Analysis of Fully Developed Laminar Mixed Convection in
Horizontal
Internally Finned Tubes

by

Sohail Mirza

A thesis
presented to the University of Manitoba
in partial fulfillment of the
requirements for the degree of
Master of Science
in
Mechanical Engineering

Winnipeg, Manitoba, 1983

ANALYSIS OF FULLY DEVELOPED LAMINAR MIXED CONVECTION IN

HORIZONTAL

INTERNALLY FINNED TUBES

by

Sohail Mirza

A thesis submitted to the Faculty of Graduate Studies of
the University of Manitoba in partial fulfillment of the requirements
of the degree of

MASTER OF SCIENCE

© 1983

ABSTRACT

Fully developed, laminar, mixed convection is analyzed in horizontal tubes with two vertically oriented internal fins. Constant heat input axially and uniform wall temperature circumferentially are assumed. A mathematical model was developed for which the solution was obtained using the finite difference method applied on a Marker and Cell type of mesh.

Results are presented for a Prandtl number of 0.7, Grashof numbers of upto 10^6 , and fin height to internal radius ratios of 0 (smooth tube), 0.25, 0.50, 0.75 and 1.0. These results include the secondary flow, axial velocity and temperature distributions and local heat flux distribution. Engineering parameters such as the friction factor and Nusselt number are then evaluated based on these distributions.

Free convection effects are found to be significant, especially for large Grashof numbers and short fins. Fins are found to suppress the free convective currents. The percentage increases in Nusselt number and friction factor over their forced convective values are found to decrease as the fin height increases. In all cases considered, the percentage increase in Nusselt number (due to free convection) is significantly higher than the percentage increase in friction factor.

ACKNOWLEDGEMENTS

NOMENCLATURE

English Symbols

A   cross sectional area of the tube [m²]

c   specific heat at constant pressure [J/kg K]

D   continuity term, defined by equation (4.7)

Fr   gravitational body force per unit volume in the radial direction [N/m³]

Fϕ gravitational body force per unit volume in the angular direction [N/m³]

f   mean friction factor, defined by equation (5.5)

Gr   Grashof number, $(8\beta r_0^3 gQ)/(\nu^2 \pi k)$

g   acceleration of gravity [m/sec²]

H   non-dimensional fin height, ℓ/r_0

h   mean convective heat transfer coefficient, defined by equation (5.9). [W/m²K]

i,j   indices in the R and ϕ directions, respectively.

k   thermal conductivity [W/m K]

ℓ fin height [m]

Nu   Nusselt number, $2hr_0/k$

P   non-dimensional pressure, defined by equation (3.8h)

Pr   Prandtl number, $\mu c/k$

p   pressure [N/m²]

Q   input heat rate per unit length [W/m]

q''   local heat flux [W/m²]

$\bar{q}''$ mean heat flux [W/m²]

R non-dimensional radial coordinate, r/r_0

Ra Rayleigh number, $Gr\, Pr$

Re Reynolds number, $2w_b r_0/\nu$

r radial coordinate [m]

r_0 internal radius of the tube [m]

T temperatute [K]

T_w wall temperature of the tube and fins [K]

T_b bulk temperature of the fluid [K]

t non-dimensional time, $\tau\nu/r_0^2$

U radial velocity (non-dimensional), defined by equation (3.14a)

U^* radial velocity (non-dimensional), defined by equation (3.8d)

u radial velocity [m/sec]

V angular velocity (nondimensional), defined by equation (3.14b)

V^* angular velocity (non-dimensional), defined by equation (3.8e)

v angular velocity [m/sec]

W axial velocity (non-dimensional), defined by equation (3.14d)

W^* axial velocity (non-dimensional), defined by equation (3.8f)

w axial velocity [m/sec]

w_b bulk velocity of the fluid [m/sec]

Z   axial coordinate(non-dimensional), defined by equation(3.8b)

z   axial coordinate [m]

Greek Symbols

β volumetric coefficient of thermal expansion [K^{-1}]

θ temperature(non-dimensional), defined by equation (3.14c)

θ^{*} temperature(non-dimensional), defined by equation(3.8g)

μ viscosity [N sec/m²]

ν kinematic viscosity [m²/sec]

ρ fluid density [kg/m³]

$\rho_{\bullet}$ fluid density at wall temperature [kg/m³]

ϕ angular coordinate

τ time [sec]

CONTENTS

LIST OF FIGURES

LIST OF TABLES

Chapter I

INTRODUCTION

The need for compact heat exchangers has invigorated an extensive research into different methods of heat transfer augmentation. This research has so far proposed several methods. Some of these methods, e.g., surface vibration, electrostatic fields and fluid additives are not suitable for most applications on account of additional costs and requirements of auxiliary power.

A more attractive technique is that of surface promoters, which is designed to reduce the thermal resistance at the surfaces of the tubes. Due to its simplicity, this technique has gained special attention. The internally finned tubes belong to this class and have become extremely popular in recent years. Feasibility of manufacturing and significantly improved heat transfer performance over smooth tubes are the main reasons for the success of these tubes. However, the enhancement in the rate of heat transfer is achieved at the cost of increased pumping power. Shape and type (straight or spiral) of internal fins, their relative height, interfin spacing and many other parameters were reported to have an influence on the tube performance of these tubes.

For internally finned tubes, both laminar and turbulent flows were studied, several tube configurations were considered

- 1 -

and data on the corresponding pressure drop and heat transfer performance were reported. Analytical and experimental techniques were used in these investigations. The mathematical models used in both laminar and turbulent flow situations assumed pure forced convection. For the case of turbulent flow, the analytical and experimental results showed close agreement. On the other hand, the analytical predictions of laminar heat transfer deviated significantly from the experimental results. This deviation is attributed to the presence of free convection inside the tube. In turbulent flow where the inertia forces are much larger than the viscous forces, free convection effects are normally insignificant. Hence, the analytical predictions are expected to match well with the experimental data. In laminar flow, free convection is known to have significant effects on the velocity and temperature distributions within the flow cross section and hence cannot be ignored in the analysis.

From a mathematical point of view, inclusion of free convection into the analysis of laminar fluid flow and heat transfer through internally finned tubes is a difficult task. In order to model mixed free and forced convection mathematically, the system of governing equations becomes highly non linear and hence extremely difficult to solve. Tube orientation is yet another factor which determines the nature of these equations. For vertically oriented tubes, the forced and free convection currents are unidirectional and hence the analysis requires solutions of two dimensional velocity and pressure fields. In horizontal tubes,

free convective currents are perpendicular to the forced convection and three dimensional velocity and pressure fields are required to be solved. In the literature, no analysis is available where, the laminar mixed convection problem in horizontal internally finned tubes is investigated.

The motivation behind the present study is to include the effects of free convection in fully developed laminar flow of air (Pr=0.7) inside internally finned tubes. Two straight longitudinal fins of variable height are incorporated in the smooth tube geometry to simplify the analytical complexities. Constant axial heat input is assumed at the wall. With this geometry and boundary condition, objectives of this work can be summarized as follows:

1. To investigate the effects of fin height and Grashof number on the following parameters:

    a. Secondary flow induced by free convection currents.

    b. Axial velocity and temperature distributions.

    c. Local heat flux distribution along the circular
       tube wall and fins.

    d. Overall values of friction factor and Nusselt number.

2. To establish an analytical background for further research in the same area where more than two internal fins are considered.

Chapter II

LITERATURE REVIEW

Analysis of laminar fluid flow and heat transfer in horizontal tubes where a veritable proposition of mixed convection is taken into consideration, poses serious difficulties. When the problem is approached analytically, complexity of the governing partial differential equations, as will be seen later, makes attainment of exact solutions a formidable task. Early analysts seeking closed form solutions, mostly made their models very exclusive by employing various simplifying assumptions. Consequently, their solutions became either very restrictive or completely unrealistic [1].

The analysis is further intricated if the flow cross section deviates from the simple circular geometry of smooth tube. Experimental results therefore, remain the main source of information when design considerations are made. Today however, the painful and time consuming task of experimental research can be substantially reduced by incorporating modern computer technology, and many variations of a given problem can be studied with relative ease.

It has been experimentally observed that introduction of internal fins substantially increases the rate of heat transfer at the cost of increased pumping power. During laminar flow, free

- 4 -

convection effects are expected to be significant. It is desirable therefore to study this problem analytically. As will be seen in this review, the case of laminar mixed convection in horizontal internally finned tubes has not yet been solved.

In the perspective of above discussion, it is imperative that experimental as well as mathematical researches involving both the smooth and internally finned horizontal tubes be reviewed. Since the present solution was developed numerically, it was also felt important that a brief literature survey of some widely employed numerical methods pertaining to incompressible fluid flow and heat transfer problems be included. This chapter is therefore divided into three sections. Selected literature is reviewed in respective context with reasonable brevity.

2.1 SMOOTH TUBES

2.1.1 Experimental

Experimental work done in the area of incompressible flow and heat transfer in horizontal tubes, where the presence of secondary flow is recognized goes back to the 1920's. However, it was not until the late 1950's that serious attention was paid to the enhancement of heat transfer and pumping friction due to the existence of secondary flow.

Essentially, two limiting boundary conditions were imposed at the tube wall. One corresponds to the isothermal tube-wall, and the other is the case of constant wall heat flux. In the case of constant wall heat flux, a constant temperature difference exists

between the fluid bulk temperature and the tube wall in the fully developed region. This difference generates density gradients causing secondary flow perpendicular to the main or primary flow. It can be said (given everything else constant) that application of higher heating loads would augment the intensity of secondary flow. Hence, free convection exists not only through the entire length of the tube but, its magnitude is proportional to heating loads. Grashof and Rayleigh numbers are commonly used as dimensionless measures of the intensity of applied heating loads.

McComas and Eckert [2] studied the mixed laminar convection in horizontal tubes with constant wall heat flux using air as working fluid. Low heating loads (Gr=1000) were applied and an attempt was made to correlate Nusselt number with Rayleigh number and a non-dimensional length ratio. Although these researchers were doubtful about the usefullness of this non-dimensional length ratio, it was however incorporated. Previous researches on vertical smooth tubes showed a strong dependence on this ratio. It is to be noted that in vertical tubes the primary and secondary flows are unidirectional , whereas, in horizontal tubes they are perpendicular to each other. Any dependence of Nusselt number on length ratios is not intuitively conceived. At low heating loads, the weak secondary flow does not substantially alter the values of heat transfer coefficient and friction factor. These researchers could only observe a slight decrease in wall temperature compared to that predicted by the forced convective analysis.

A significant work where higher heating loads were applied was carried out in the Soviet Union. Petukhov and Polyakov [3,4] experimentally investigated the local heat transfer during laminar flow of water in a horizontal stainless steel tube subjected to constant wall heat flux. The measurements were performed over a Reynolds number range of 50 to 2400 and Rayleigh number varying from $2x10^4$ to $4x10^7$. They proposed a correlation equation for the average Nusselt number as a function of Rayleigh number alone. It was reported that due to the presence of free convection, the wall temperature varied considerably over the perimeter of the tube. This fostered the notion that there exists in the upper portion of the tube, a region where fluid has a relatively high temperature and which is not encompassed by the cross circulation. For the values of Rayleigh number of the order of 10^6 , average Nusselt number was reported to have increased about threefold over the forced convective value. Another interesting feature reported is the delay of laminar-turbulent transition in terms of Reynolds number. Higher values of Reynolds number were needed to reach this transition in comparison with the case of pure forced convection.

Shannon and Depew [5] reported similar findings. Water was used in a smooth copper tube and a fully developed velocity profile was established at the onset of heating. Reynolds number ranged from 120 to 2300 and the highest value of Grashof number was $2.5x10^5$. The thermal entry region was found to be very small. Values of Nusselt number two-and-a-half times larger than

those expected from forced convection were found at this value of Grashof number.Nusselt number was correlated with Rayleigh number.

The additional factor of wall conductance was incorporated by Bergles and Simonds [6] .They used glass and copper tubes subjected to constant wall heat flux and water was used as working fluid. This study reported a qualitative and visual picture of the effects of free convection on forced convection. Reasonably high heating loads (Ra=10^8) were applied. At this high value of Rayleigh number, the heat transfer coefficient reached three to four times the value predicted by traditional forced convective solutions where secondary flow is altogether ignored. An important feature of this study was the identification of upper and lower bounds of the average Nusselt number at high heating loads. Since the presence of free convection lowers the wall temperature, conductivity of the tube material determines these bounds. For practical purposes, glass and copper tubes were assigned these lower and upper bounds, respectively. Based on these considerations, a tentative composite prediction plot was recommended, which matched well with the correlations suggested by Petukhov and Polyakov [3,4] who used a stainless steel tube.

Morcos and Bergles [7] extended this work to ethylene glycol. They employed glass and stainless steel tubes and confirmed the arguments suggested by Simonds and Bergles [6]. For fully developed laminar flow, Nusselt number primarily depended upon Rayleigh number, however, a dimensionless tube wall conductance pa-

rameter was also required to correlate the heat transfer data. In this study,effects of increasing Rayleigh number on pumping friction were also investigated. The friction factor was found to increase with Rayleigh number, however, its relative increase in comparison with Nusselt number was small.

For the case of isothermal wall, reasonable amount of work has been reported. In horizontal isothermal tubes, the effect of free convection on forced convection is present only in the thermal entry region. As the fluid travels down the tube length,the fluid bulk temperature approaches the wall temperature. At one point,the wall to bulk temperature difference becomes small, thus eliminating the cause of free convection. It is therefore obvious that,in the case of isothermal tubes, some characterstic length based on the tube dimensions be incorporated in establishing correlations.

Brown and Thomas [8] investigated combined free and forced convection heat transfer for laminar flow in horizontal isothermal tubes. Water was used as working fluid and Nusselt number was correlated with Graetz and Grashof numbers. Although the values of Grashof number were not very large, a rise in Nusselt number values was reported. These researchers suggested that mass flow rate of the fluid could be an important factor in establishing meaningful correlations. The argument was based on finite length tubes, where only forced convection was considered. It was argued that at higher flow rates, the temperature profile remains steep at the sides of the tube whereas at lower flow rates the profile

becomes more curved, and temperature gradient at the wall is therefore small. If free convection is to be superimposed on the above two cases, it could be reasonable to assume that the steeper temperature profile would give rise to a greater rate of mixing, hence it was concluded that heat transfer enhancement due to free convection would depend on flow rates as well.

Depew and August [9] confirmed the argument that mass flow rate could be an important factor. They however challenged the assumption that the length to diameter (L/D) ratio could be a significant parameter in free convection functions. Analysis of relatively short tubes helped conclude this objection. Since the temperature gradient at the wall falls with the increasing distance along the tube length, the gradient for a short tube would remain relatively steep for the entire length. It was presumed that short thin tubes would exhibit relatively higher natural convection effects than longer tubes, hence (L/D) ratio loses its significance as a universal entity. In an attempt to derive a correlation between Nusselt and Grashof numbers, viscosity was found to have profound effects. Hence, Prandtl number was incorporated as an independent parameter.

In both of the above two researches, the influence of free convection was found to be substantial as far as enhancement in the rate of heat transfer is concerned. Yousef and Tarasuk [10] conducted an interferometric study of isothermal tubes. Reynolds number ranged from 120 to 1200 and, Grashof number varied from 0.8×10^4 to 8.7×10^4. A wide variety of (L/D) ratios was inves-

tigated (L/D = 6 - 46). These investigators employed Mach-Zender interferometer to determine the three dimensional temperature field and the circumferential and average Nusselt number for air in the entry region. Significant changes in temperature profile from that of pure forced flow case were noted. Nusselt number at the bottom was reported to be as high as five times the value at the top. Intensity of free convection was found to be maximum at the tube inlet, while in the fully developed region, no secondary flow was found. In a later report [11] , the same investigators proposed correlations between Nusselt number and parameters such as Grashof number, Graetz number and Prandtl number. The significant feature of this work had been the use of a wide range of (L/D) ratios and confirming Graetz number as a significant correlation entity. It was also stated that the interferometric studies offered maximum possible experimental precision to date.

2.1.2   Analytical

Many attempts have been made to analytically investigate the problem of laminar mixed convection in horizontal tubes. For both types of limiting boundary conditions, various mathematical models were proposed. Exact methods and numerical techniques were employed in solving these models. An excellent summary of this work upto 1972 was reported by Hong and Bergles [12] .

In general, these models were restricted in one way or another. Various simplifications such as limits on the value of Prandtl number, restrictions on boundary conditions, neglecting

wall conductance and inertia terms in the governing equations have made these models limited. Most of this work considered isothermal tubes and the case of constant wall heat flux for high values of heating loads is hardly available. It is interesting to note that the span of the present analysis would possibly fill a gap in the existing literature on smooth tubes as well.

For the case of uniform wall heat flux, Hong and Bergles [13] have theoretically investigated the problem of combined forced and free convection in horizontal tubes. The flow was assumed to be fully developed with a large Prandtl number. Viscosity and density were assumed to be temperature dependent. The analysis assumed uniform heat flux axially and circumferentially. Secondary flow was assumed to be composed of two regions: a thin boundary layer near the tube wall and a core which was enclosed by the boundary layer. Governing equations were separately solved analytically for the two regions. As a result of this analysis, Nusselt number was expressed as a fourth order function of Rayleigh number. Results were compared with the experimental data of ethylene glycol and good agreement was reported. This comparison was however made at relatively small heating loads ($Ra=10^4$) . As will be seen later, and as was also reported by Petukhov and Polyakov [3,4] , significant variation in the circumferential distribution of heat transfer results occur at high heating loads. Thus, the assumption of uniform circumferential wall heat flux no longer remains valid at high values of Rayleigh number. Hence, the analysis cannot be used there for accurate prediction.

Moreover, because the analysis assumed large values of Prandtl number, it is not applicable to most common fluids such as air and water, even at low heating loads.

Patankar et al. [14] have analytically studied a situation where heating was considered to be circumferentially non-uniform. Prandtl number values of 0.7 (air) and 5 (water) were used. Density was assumed temperature dependent only in the buoyancy term where Boussinesq's approximation was invoked. Two boundary conditions were considered. In the first case, the tube was heated uniformly over a 180 degree arc encompassing the upper half of its circumference, while the lower portion of the tube was kept insulated. For the second case, the situation was reversed. In both the cases, heat addition per unit length was axially uniform. Since solutions were sought for conditions where the natural convection was a first order effect rather than a perturbation of forced convection, numerical techniques were required. At high values of Grashof number, an augmentation of heat transfer was noted for both cases. This effect was more pronounced for the case of heated upper half. Values of the friction factor coefficient exhibited similar increasing trends. However, in comparison with the increase in Nusselt number, the percentage increase in friction factor was much smaller. Heat transfer was found to be independent of Reynolds number in the fully developed region.

Analytical studies directed towards establishing solutions for the entry region in isothermal tubes are relatively more nu-

merous. Hieber et al. [15] investigated mixed convection in an isothermally heated horizontal pipe. A large Prandtl number was assumed. Analysis was limited to a Reynolds number range of 100 to 1000. The solution domain for the entry region was decomposed into four regions; namely, the near region, the intermediate region, the near intermediate region and the far region. In the near region, the velocity profile was approximated by the Blausius distribution which was used to calculate the buoyancy forces. The far region was totally free of secondary flow. The governing equations were integrated in these regions with various approximations. Results thus obtained expressed Nusselt number as a function of Reynolds number, Grashof number and the (L/D) ratio. After incorporating numerous corrections, the theory was claimed to agree well with the experimental results.

Ou et al. [16] in contrast to Hieber et al. [15] solved the governing equations for the entrance region of an isothermal tube. Their analysis also used a large Prandtl number assumption (Pr > 10) and provided numerical results. The large Prandtl assumption renders the inertia terms in the vorticity transport equation negligible, thus simplifies the solution procedure. Results are however limited to viscous fluids. These analysts solved the governing equations using the finite difference method and could only use Grashof number values upto 10^6. Beyond this value, the method of solution showed instability. Results were found to be in close agreement with the existing data on ethyl-alcohol and glycerol-water mixture.

Hishida et al. [17] solved the thermal entry region problem for isothermal tubes. Though the highest value of Grashof number corresponded to moderate heating loads (Gr=10⁴), no restriction on Prandtl was imposed. Dimensionless momentum and energy equations were solved using the "MAC" approach which will be discussed later. Pressure was obtained from a Poisson form of the pressure equation and stability of the finite difference scheme was restored based on similar methods as will be used in the present analysis. The present author however, views the convergence criterion used by these analysts with some skepticism.

In both types of boundary conditions, the author is unaware of a model where no serious assumption to simplify the equations have been used while sufficiently high heating loads are applied. The present analysis assumes constant heat application per unit length with no restriction on Prandtl number or heating load.

2.2   HORIZONTAL INTERNALLY FINNED TUBES

2.2.1   Experimental

Relatively few studies are available for the internally-finned-tubes performance. An excellent summary of this work upto 1968 was reported by Bergles [18] and updated upto 1970 by Bergles and Webb [19].

Watkinson et al. [20] obtained data of pressure drop and heat transfer of horizontal internally finned tubes in laminar oil flow. Tubes with variable number of straight and spiral fins were used. A steam jacket surrounded the test section to ensure

an isothermal boundary condition. Various kinds of oil (Pr = 180 - 250) were used and Reynolds number ranged from 50 to 3000. At Reynolds number of 500, heat transfer was enhanced over smooth tube values by 8 to 224 percent depending on the tube geometry. For the same value of Reynolds number and pumping power, the increase in heat transfer ranged from 1 to 187 percent. It was reported that, given all other conditions unchanged, fewer but longer fins gave larger heat transfer coefficients. This study proposed correlations for Nusselt number as a function of number of fins, Reynolds number, Grashof number and (L/D) ratio. For straight fins, the reciprocal of the number of fins was employed in these correlations while inter-fin spacing to pitch ratio was used for spiral fins.

Marner and Bergles [21] studied the heat transfer characterstics of an internally finned tube with ten longitudinal fins. Uniform heat flux was applied on the tube wall and very limited data was reported. Dependence of Nusselt number on Prandtl number was shown, but no correlation was reported.

For the uniform wall heat flux case, no comprehensive experimental work has been reported to date for horizontal internally finned tubes. A work of this nature is in progress at Heat Transfer Laboratories of the the department of Mechanical Engineering, University of Manitoba. It is anticipated that very comprehensive data will be reported in the near future.

2.2.2   Analytical

The author is unaware of any analytical work where horizontal internally finned tubes were treated for the situation of mixed laminar convection. This problem was however solved under forced convective flow conditions where secondary flow was neglected.

Hu and Chang [22] investigated the heat transfer of fully developed laminar flow in straight finned tubes. Fins were considered very thin.   It was assumed that a constant heat flux existed over the cylindrical tube surface and along each fin. This assumption is unrealistic and could lead to very misleading results. These analysts tentatively suggested an optimum point in terms of number of fins and their height as parameters. For no viscous dissipation and no internal heat generation, a tube with 22 internal fins and of fin height to tube radius ratio of 0.795 gave the highest Nusselt number value.

As a pre-requisite to study the forced convective heat transfer characterstics of internally finned tubes, Nandakumar and Masliyah [23] obtained a finite element solution of the momentum equation describing laminar fluid flow in straight finned tubes. It was concluded that Reynolds number, inter-fin spacing and fin height determined the value of friction factor.

An improvement was later made by Soliman and Feingold [24] who developed an infinite series solution for the velocity distribution and friction factor. A fin shape which resembled closely the real fin configuration was used in this analysis. Flow was

assumed to be fully developed and laminar. For tubes with long fins, secondary loops were found to exist within the inter-fin region. This work was extended by same analysts [25] to include the heat transfer case. For various combinations of fin height and thicknesses, it was found that the Nusselt number increased with the number of fins " M " upto a critical value of M. Beyond this value, a reversal of trend occured. Soliman [26] included the effect of fin conductance. Under uniform heat flux axially and constant outside wall temperature circumferentially, the heat transfer characterstics were influenced by the product of the fin half angle and the ratio of thermal conductivity of fin material to that of fluid.

Soliman et al. [27] investigated the isothermal wall boundary condition in internally finned tubes. Fin conductance was taken into account and a finite difference solution was obtained for variable number of fins and fin heights. A very interesting feature of this analysis is the fact that fin surface proved to be a more effective heat transfer surface than the tube wall. This was observed for about the whole range of number of fins used. From the results, it was concluded that the heat transfer coefficient along the side of the fins was not uniform. In previous analyses e.g. [20] , this finding is contradicted when fin efficiency was calculated. It would be very interesting to note the results of present analysis pertaining to this area.

An important analysis where the effects of buoyancy forces on the overall heat transfer enhancement were considered, was

carried out by Acharya and Patankar [28] . Laminar mixed convection was analysed in a shrouded fin array. Results were reported for three values of tip clearance and two boundary conditions. For hot fin and base, which is most relevent to the present analysis, it was found that the Nusselt number increased with Grashof number and tip clearance. Maximum value of Nusselt number was obtained when the tip clearence was equal to the fin height. For the same value of fin height, maximum amount of heat was transfered from the fin surface. Coefficient of friction showed similar increasing trends with a maximum value again corresponding to the case where. the tip clearance was equal to the fin height. Though this geometry cannot provide an estimate for internally finned tubes, it greatly motivates an analysis where both the effects of internal fins and the presence of free convection are simultaneously analysed. The present study is directed towards this same goal.

Prakash and Patankar [29] solved the combined free and forced convection problem in vertical tubes with radial internal fins. Although this configuration is different from the horizontal tubes and unidirectional primary and secondary flows make the solution procedure considerably simpler, however, the analysis provides important information about the effects of buoyancy on forced convection. Flow was considered fully developed laminar and constant axial heat flux was assumed. Rayleigh number varied from 10 to 10^5 and several tube geometries in terms of number of fins and their relative heights were considered. Finite differ-

ence forms of governing partial differential equations which were obviously not a function of angle, were numerically solved. The buoyancy force was found to increase significantly both friction and heat transfer in the finned tubes; augmentation factors in the range of 5 to 10 were encountered for the heat transfer process. Although friction coefficient showed an increase as well, corresponding augmentation factors were much less than the heat transfer. The effect of buoyancy was particularly strong when less fins of shorter length were analyzed.

2.3 NUMERICAL METHODS IN INCOMPRESSIBLE FLOW PROBLEMS

A complete survey of all the numerical techniques pertaining to incompressible fluid flow and heat transfer problems is beyond the scope of this thesis. An excellent survey with brief discussion on nearly all numerical methods in fluid dynamics is presented by Roache [30].

The finite difference method remains the most widely employed numerical technique to solve the governing differential equations. Miyakoda [31] has discussed various possibilities to implement this method for incompressible fluid flow problems. His work reviews and explains some basic forms of partial differential equations appearing in the area of incompressible fluid flow. Solution procedures and stability criteria are also discussed.

Two standard procedures are usually employed to establish solutions for the incompressible fluid flow problems. The first

approach is to solve the primitive equations without any altera-
tions or functional transformations. Primitive variables are cal-
culated directly using any applicable standard method. The second
approach is to transform the primitive equations into vorticity
transport and stream function equations. Pressure is eliminated
from the system by cross differentiation of momentum equations
and solutions are expressed in terms of vorticity and stream
functions. If required, primitive variables can be determined by
integrating the obtained values of vorticity and stream func-
tions.

The primitive approach is recommended [30] for problems with
free surfaces or fluid interfaces. In most of the cases however,
the vorticity-stream function approach provides easier formula-
tions and shorter computational time.

For the present analysis, the primitive variable approach
was chosen. It provides a first hand description of the secon-
dary flow and pressure distribution which can be found without
further manipulations.

Both of the above approaches could be incorporated for
steady incompressible flow and the same solution procedures can
be applied. These solution procedures can be divided into two
classes in general. The first class treats steady state equa-
tions as they are and either direct non-iterative or iterative
methods are applied to establish a solution. In this class, the
Spalding-Patankar method [32], has found extensive use. This ful-
ly implicit finite difference scheme is essentially designed for

duct flow or boundary layer problems where stream wise second derivatives of unknown variables can be neglected. This enables solutions to be obtained by starting with any known values in the axial direction and marching downstream in the flow direction.

The second class of methods for steady state problems is the method of pseudo or "false" transient. The basic idea behind this technique is to consider a steady state problem temporarily unsteady. Transient solutions are successively obtained or a "marching in time" process is carried out to a point where, no change in the values of variables with time is observed. Since at this point, the time derivatives vanish, the results can be considered of a steady state. Roache [30] has proved that the false transient approach is equivalent to the steady state methods of the first class discussed earlier. He argued that, since the transient approach does not presume a steady state solution, it is preferable. In some instances, although a steady state is assumed to exist, in reality it may never exist at all. This approach is also prefered because the Von Neuman stability criteria are well established, whereas in the steady state schemes, rationally derived criteria are hardly available. Various schemes to solve false transient or transient equations are available and are schematically summarized by Roache [30].

In the incompressible fluid flow equations, the finite difference form of non-linear convection terms produce some instability. This is caused by accumulated truncation errors. In early investigations, when the phenomenon was not properly understood,

shorter time steps were used as a remedy. In other words, vari-
ables were under-relaxed to very small values. A delayed diver-
gence or meaningless results were obtained. Harlow and Welch [33]
proposed a method where, in addition to the recognition of this
problem,a solution technique was recommended. This method has
been used in the present analysis and is discussed at length in
chapter IV.

Chapter III

STATEMENT OF THE PROBLEM

3.1   PHYSICAL MODEL

The geometry under consideration is that of a horizontal tube with two longitudinal internal fins shown in figure 3.1 .The tube has an inside radius r_0 and the fins are straight longitudinally.   For this geometry, the cylindrical coordinate system (r,ϕ,z) is the obvious choice.

The present analysis considers only hydrodynamically and thermally fully developed laminar flow with uniform axial heat input.   Consequently, the values of velocity, axial pressure gradient and axial temperature gradient are invariant along the z axis.

The fluid is considered incompressible with constant physical properties.   The density is temperature dependent only where buoyancy effects are considered.   The fins and the tube wall are assumed to be of negligible thickness and negligible thermal resistance.   As a result, the temperature can be considered uniform circumferentially throughout the tube-wall and fins. This assumption closely approximates real life situation where tubes with internal fins are made of highly conductive material such as copper.
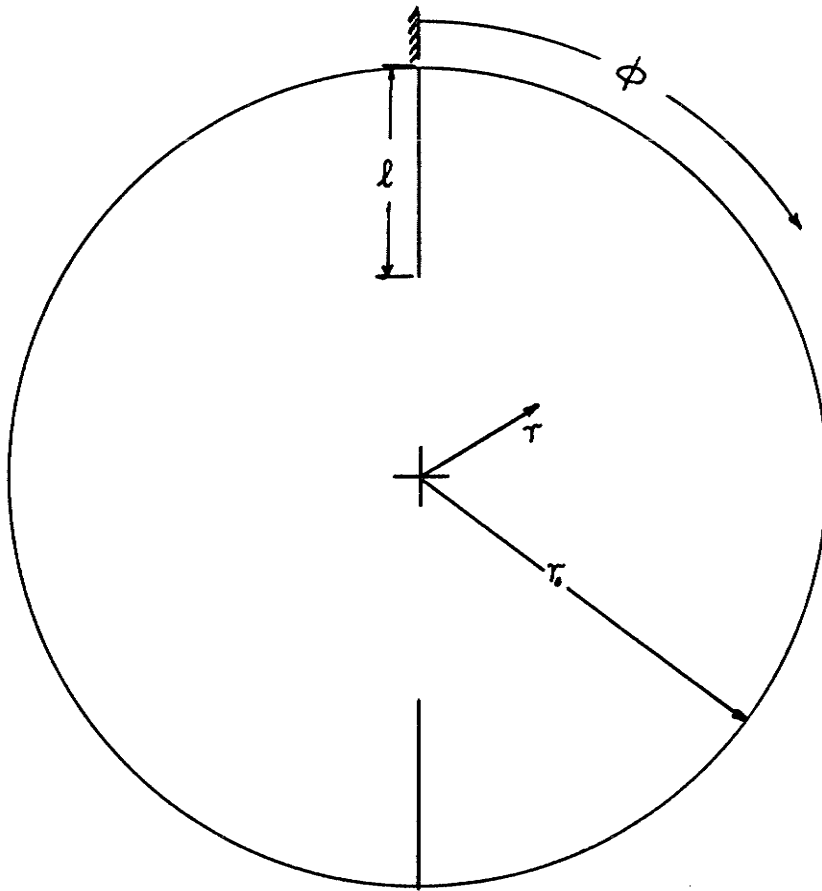
Fig. 3.1 Tube geometry and coordinate system

There is no restriction on the type of fluid and therefore any realistic value of Prandtl number could be incorporated in the analysis. There is also no restriction on the magnitude of the applied heating load and hence the analysis can incorporate any value of Grashof number for which a numerical solution is possible.

Application of heat at the wall would create a temperature difference between the fluid close to the wall and the fluid away from it. This in turn would create density gradients throughout the cross section which cause free convection or secondary flow perpendicular to the axial or primary flow. The hot and hence light fluid moves upwards while the heavier fluid comes down to take its place. This phenomenon is responsible for secondary loops whose motion can be described in terms of the radial and angular components of the velocity vectors. Unlike pure forced convection where heat is convected only axially, secondary flow improves the temperature mixing process, thereby enhancing the heat transfer. This secondary motion however acts as an obstruction to the primary flow and therefore increases the frictional drag.

Increase in the inside surface area due to the presence of internal fins is expected to enhance the rate of heat transfer. However, the intensity of secondary flow is likely to decrease as well, which may decrease the rate of heat transfer. This adverse effect hence poses the problem of determining the most efficient geometry in terms of maximum rate of heat transfer at minimum

possible pumping power.   Tube with two longitudinal internal fins
is analyzed with the same basic idea under consideration.

3.2   MATHEMATICAL MODEL

The problem can be completely described by the Navier-Stokes
equations,   continuity equation and energy equation.   These equa-
tions after simplifications based on the assumptions mentioned in
the previous section can be written as:

1.   Radial Momentum Equation:

$$u \frac{\partial u}{\partial r} + \frac{v}{r} \frac{\partial u}{\partial \phi} - \frac{v^2}{r} = - \frac{1}{\rho} \frac{\partial p}{\partial r} + Fr + \frac{\mu}{\rho} \{\nabla^2 u - \frac{2}{r^2} \frac{\partial v}{\partial \phi} - \frac{u}{r^2}\} \qquad (3.1)$$

2.   Angular Momentum Equation:

$$u \frac{\partial v}{\partial r} + \frac{v}{r} \frac{\partial v}{\partial \phi} + \frac{u\,v}{r} = - \frac{1}{\rho r} \frac{\partial p}{\partial \phi} + F\phi + \frac{\mu}{\rho} \{\nabla^2 v + \frac{2}{r^2} \frac{\partial u}{\partial \phi} - \frac{v}{r^2}\} \qquad (3.2)$$

3.   Axial Momentum equation:

$$u \frac{\partial w}{\partial r} + \frac{v}{r} \frac{\partial w}{\partial \phi} = - \frac{1}{\rho} \frac{dp}{dz} + \frac{\mu}{\rho} \{\nabla^2 w\} \qquad (3.3)$$

4.   Continuity Equation:

$$\frac{1}{r} \frac{\partial}{\partial r} (ur) + \frac{1}{r} \frac{\partial v}{\partial \phi} = 0 \qquad (3.4)$$

5. Energy Equation:

$$\rho c \left\{ u \frac{\partial T}{\partial r} + \frac{v}{r} \frac{\partial T}{\partial \phi} + w \frac{dT}{dz} \right\} = k \nabla^2 T \tag{3.5}$$

where ∇^2 is the well known Laplacian operator. Equations (3.1) to (3.5) are five nonlinear partial differential equations in five unknowns; u,v,w,p and T. The unknowns in these equations are inseparable, and hence equations (3.1) to (3.5) must be solved simultaneously. The axial pressure gradient dp/dz will be treated as a constant since the flow is fully developed. Also, since heat is added uniformly in the axial direction the axial temperature gradient dT/dz becomes a constant.

The terms Fr and Fϕ in equations (3.1) and (3.2), respectively, represent the radial and circumferential components of the buoyancy force. Without this force, u, v, $\partial p/\partial r$ and $\partial p/\partial \phi$ reduce to zero and the model reduces to the case of pure forced convection. Mathematically, the terms Fr and Fϕ can be expressed as:

$$Fr = -\frac{\rho}{\rho_0} g \cos \phi \tag{3.6a}$$
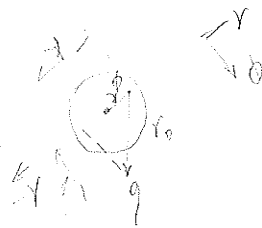
$$F_\phi = \frac{\rho}{\rho_0} g \sin \phi \tag{3.6b}$$

where ρ is the local density, while ρ_0 is the density correspond-
ing to the wall temperature. Invoking the Boussinesq's approxima-
tion which assumes basically that the density varies linearly
with temperature, we get:

$$Fr = -\{1-\beta(T-T_w)\} \ g \ \cos \phi \qquad (3.7a)$$

$$F_\phi = \{1-\beta(T-T_w)\} \ g \ \sin \phi \qquad (3.7b)$$

It is recognized that, a non-dimensional form for the gov-
erning equations is not only convenient for analytical solution
but, in addition the results can also be expressed in a general-
ized form. The following transformations were used to accomplish
this task.

$$R = \frac{r}{r_0} \qquad (3.8a)$$

$$Z = \frac{z \ W_b}{\nu} \qquad (3.8b)$$

$$H = \frac{\ell}{r_0} \qquad (3.8c)$$

$$U^* = \frac{u \, r_o}{\nu} \qquad\qquad (3.8d)$$

$$V^* = \frac{v \, r_o}{\nu} \qquad\qquad (3.8e)$$

$$W^* = \frac{w}{w_b} \qquad\qquad (3.8f)$$

$$\theta^* = (T-T_w) \, \pi k \, / \, Q \qquad\qquad (3.8g)$$

It is assumed that, axial pressure gradient is uniform along the tube cross section. The independence of dp/dz over r and ϕ enables the use of following transformation to simplify the equations in terms of non-dimensional quantities:

$$P = \frac{r_o \, p}{\rho \nu} + \frac{r_o^2}{\nu^2} r \, g \, \cos \phi \qquad\qquad (3.8h)$$

In the manipulation of governing equations (3.1) to (3.5) in accordance with the transformations introduced in equation (3.8), the invariance of axial temperature gradient dT/dz is taken into account and the following equation, derived from energy balance over a given control volume is used:

$$\frac{dT}{dz} = \frac{Q}{\pi r_o^2 w_b \rho c} \qquad\qquad (3.8i)$$

With these transformations, a non-dimensional set of equations corresponding to equations (3.1) to (3.5) can be written as:

1. Radial Momentum Equation:

$$U^* \frac{\partial U^*}{\partial R} + \frac{V^*}{R} \frac{\partial U^*}{\partial \phi} - \frac{V^{*^2}}{R} = - \frac{\partial P}{\partial R} + \frac{Gr}{8} \theta^* \cos\phi + \{\nabla^2 U^* - \frac{2}{R^2} \frac{\partial V^*}{\partial \phi} - \frac{U^*}{R^2}\} \quad (3.9)$$

2. Angular Momentum Equation:

$$U^* \frac{\partial V^*}{\partial R} + \frac{V^*}{R} \frac{\partial V^*}{\partial \phi} + \frac{U^* V^*}{R} =$$
$$- \frac{1}{R} \frac{\partial P}{\partial \phi} - \frac{Gr}{8} \theta^* \sin\phi + \{\nabla^2 V^* + \frac{2}{R^2} \frac{\partial U^*}{\partial \phi} - \frac{V^*}{R^2}\} \quad (3.10)$$

3. Axial Momentum Equation:

$$U^* \frac{\partial W^*}{\partial R} + \frac{V^*}{R} \frac{\partial W^*}{\partial \phi} = - \frac{dP}{dZ} + \nabla^2 W^* \quad (3.11)$$

4. Continuity Equation:

$$\frac{1}{R} \frac{\partial}{\partial R} (U^* R) + \frac{1}{R} \frac{\partial V^*}{\partial \phi} = 0 \quad (3.12)$$

5. Energy Equation:

$$U^* \frac{\partial \theta^*}{\partial R} + \frac{V^*}{R} \frac{\partial \theta^*}{\partial \phi} + \frac{W^*}{Pr} = \frac{1}{Pr} \nabla^2 \theta^* \quad (3.13)$$

where Gr and Pr are Grashof and Prandtl numbers defined as:

$$Gr = \frac{8\beta r_o^3 g \ Q}{\nu^2 \pi k}$$

$$Pr = \frac{\mu c}{k}$$

It is obvious from the above equations that the dimension-less flow parameters (U^*, V^*, W^*, P and θ^*) at any point (R, ϕ) are dependent on the values of Gr and Pr. As expected, Reynolds number is not a factor since the flow is fully developed.

The boundary conditions necessary for solving the above system of equations are easy to formulate. Due to the symmetry around the vertical plane passing through the fins, solution need to be sought for only half of the flow domain. The origin now becomes a part of the boundary, and is a point where the boundary conditions (especially for U^* and V^*) are not well defined. Consequently, these transformations were adopted:

$$U = R \ U^* \tag{3.14a}$$

$$V = R \ V^* \tag{3.14b}$$

$$\theta = R \ \theta^* \tag{3.14c}$$

$$W = \frac{W^* R}{-(dP/dZ)} \tag{3.14d}$$

As a result of these transformations, the well defined boundary conditions $U = V = W = \theta = 0$ exist at $R=0$. With these transformations, the governing equations take the following final form:

1. Radial Momentum Equation:

$$\frac{U}{R}\frac{\partial U}{\partial R} + \frac{V}{R^2}\frac{\partial U}{\partial \phi} - \frac{U^2 + V^2}{R^2} + R\frac{\partial P}{\partial R} - \frac{\partial^2 U}{\partial R^2} + \frac{1}{R}\frac{\partial U}{\partial R} - \frac{1}{R^2}\frac{\partial^2 U}{\partial^2 \phi} + \frac{2}{R^2}\frac{\partial V}{\partial \phi}$$

$$- \frac{Gr}{8}\theta\cos\phi = 0 \tag{3.15}$$

2. Angular Momentum Equation:

$$\frac{U}{R}\frac{\partial V}{\partial R} + \frac{V}{R^2}\frac{\partial V}{\partial \phi} + \frac{\partial P}{\partial \phi} - \frac{\partial^2 V}{\partial R^2} + \frac{1}{R}\frac{\partial V}{\partial R} - \frac{1}{R^2}\frac{\partial^2 V}{\partial \phi^2} - \frac{2}{R^2}\frac{\partial U}{\partial \phi}$$

$$+ \frac{Gr}{8}\theta\sin\phi = 0 \tag{3.16}$$

3. Axial Momentum Equation:

$$\frac{U}{R}\frac{\partial W}{\partial R} + \frac{V}{R^2}\frac{\partial W}{\partial \phi} - \frac{U\,W}{R^2} - R - \frac{\partial^2 W}{\partial R^2} + \frac{1}{R}\frac{\partial W}{\partial R} - \frac{1}{R^2}\frac{\partial^2 W}{\partial \phi^2} - \frac{W}{R^2} = 0 \tag{3.17}$$

4. Continuity Equation:

$$\frac{\partial U}{\partial R} + \frac{1}{R}\frac{\partial V}{\partial \phi} = 0 \tag{3.18}$$

5. Energy Equation:

$$\frac{U}{R}\frac{\partial \theta}{\partial R} - \frac{U\theta}{R^2} + \frac{V}{R^2}\frac{\partial \theta}{\partial \phi} - \frac{(dP/dZ)W}{Pr}$$

$$- \frac{1}{Pr}\frac{\partial^2 \theta}{\partial R^2} + \frac{1}{Pr\ R}\frac{\partial \theta}{\partial R} - \frac{1}{Pr\ R^2}\frac{\partial^2 \theta}{\partial \phi^2} - \frac{\theta}{Pr\ R^2} = 0$$

(3.19)

In the above equations, axial pressure gradient dP/dZ has been used as a scaling factor for the value of W. This is in accordance with the assumption that its value remains a constant. Since dP/dZ appears in the non-dimensional form of the energy equation, it has to be evaluated so that any change in the axial velocity be corrected and hence properly represented in the energy equation. The value of dP/dZ can be calculated as follows:

By definition, $w_b = \frac{2}{\pi r_0^2} \int_0^\pi \int_0^{r_0} w\ r\ dr\ d\phi$.

In dimensionless form, the above equation can be written as,

$$\frac{2}{\pi} \int_0^\pi \int_0^1 W^* R dR d\phi = 1$$

dividing both sides by $-(dP/dZ)$, we get

$$\frac{-dP}{dZ} = \frac{1}{\frac{2}{\pi} \int_0^\pi \int_0^1 \frac{W^* R\ dR\ d\phi}{-(dP/dZ)}}$$

and finally

$$\frac{dP}{dZ} = \frac{-1}{\frac{2}{\pi} \int_0^\pi \int_0^1 W dR d\phi}$$

(3.20)

Hence, the axial velocity distribution obtained from equation (3.17) can be substituted in equation (3.20) and the resulting value of dP/dZ can be used in the energy equation (3.19).

The following boundary conditions were applied to the governing equations [(3.15) to (3.19)], written in reference to figure 3.2:

(a) R=0:

$$U = V = W = P = \theta = 0.$$

(3.21a)

(b) $0 < R < (1-H)$, $\phi = 0°$ and $180°$:

$$\frac{\partial P}{\partial \phi} = \frac{\partial U}{\partial \phi} = \frac{\partial W}{\partial \phi} = \frac{\partial \theta}{\partial \phi} = V = 0$$

(3.21b)

(c) $(1-H) < R < 1$, $\phi = 0°$ and $180°$:

$$U = V = W = \theta = \frac{\partial P}{\partial \phi} = 0$$

(3.21c)

(d) R=1 , $0 \leq \phi \leq 180°$:

$$U = V = W = \theta = 0$$

$$\frac{\partial P}{\partial R} = \frac{\partial^2 U}{\partial R^2} - \frac{\partial U}{\partial R}$$

$\text{from } (3.15)$

(3.21d)
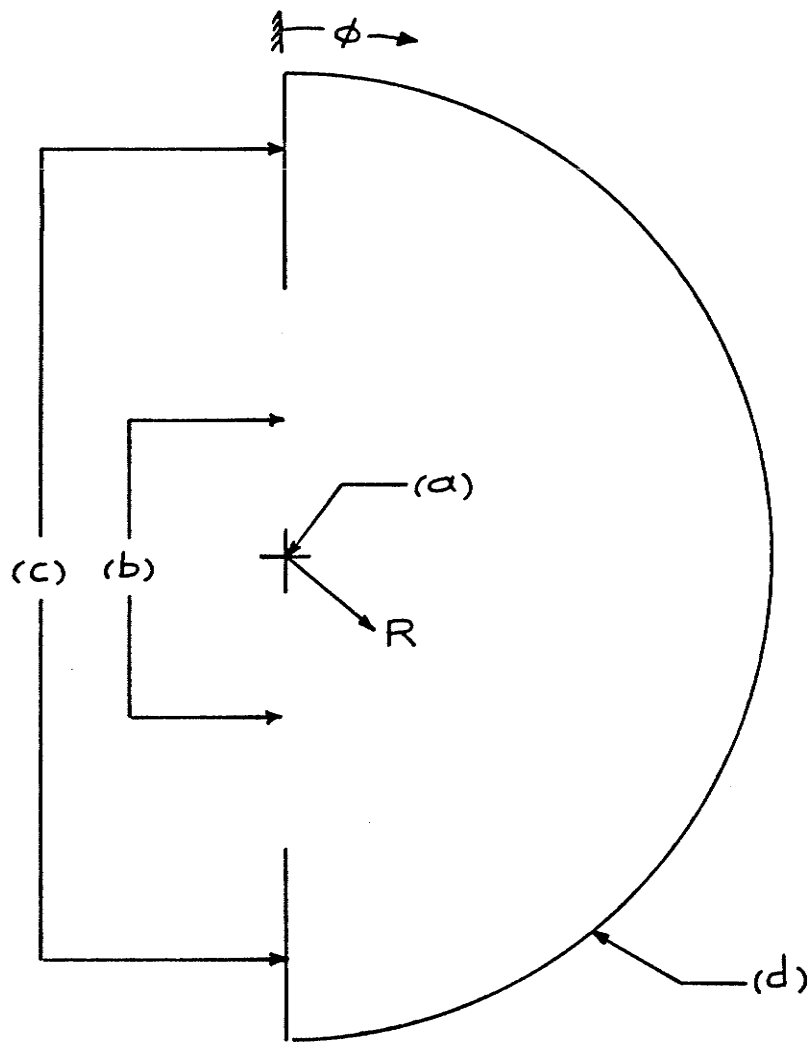
Fig. 3.2   Flow domain and different locations for
           the boundary conditions

The choice of P=0 at R=0 is quite arbitrary and does not influence the values of U, V, W or θ. According to equations (3.15) and (3.16), the pressure gradients and not the absolute values of pressure are relevent. Since a value of pressure must be specified in the domain for numerical stability, the above choice was made. Formulation of the mathematical model is now complete.

Chapter IV

METHOD OF SOLUTION

Due to the complexity of the governing partial differential equations (3.15) to (3.19), no attempt was made to establish a closed form analytical solution. The finite difference method was considered to be the best choice.

The technique of false transients in conjunction with the Marker and Cell type of mesh was used with certain modifications. This technique and its merits are discussed in the next two sections. However, it is emphasized that, for a complete understanding of the approach, this whole chapter should be reviewed.

4.1   TRANSIENT EQUATIONS

The set of equations (3.15) to (3.19) with boundary conditions (3.21) are sufficient to obtain a steady state solution of the present problem. In the early stages of this work, equations similar to (3.15) to (3.19) were programmed using direct iterative methods but instability was repeatedly encountered whenever a finite non-zero value of Grashof number was used. Accumulated truncation error was among one of the less obvious reasons. The governing equations were not being satisfied exactly at each iteration and no handy remedy was available.

After an extensive literature survey, the Marker and Cell method originally developed by workers at the Los Alamos Laboratories was selected on account of its inherent conservative nature to overcome this problem. This method requires satisfying the Continuity equation (3.18) at every time step. If the time dependent momentum equations are modified at each new time step by forcing the continuity term to zero, convergence and stability is expected. Since a steady state solution is sought, progress in time could be carried out to a point where time derivatives of all variables would vanish.

In this analysis, transient solutions are not the goal, but a tool for establishing the steady state solution. The modifications required in order to incorporate the method of false transients is straightforward. Time derivative terms in the momentum and energy equations, which were previously set to zero, are now retained. With nondimensional time, equations (3.15) to (3.19) would take following form:

i. Radial Momentum Equation:

$$
\frac{\partial U}{\partial t} = -\frac{U}{R}\frac{\partial U}{\partial R} - \frac{V}{R^2}\frac{\partial U}{\partial \phi} + \frac{U^2 + V^2}{R^2} - R\frac{\partial P}{\partial R} + \frac{\partial^2 U}{\partial R^2}
$$
$$
- \frac{1}{R}\frac{\partial U}{\partial R} + \frac{1}{R^2}\frac{\partial^2 U}{\partial \phi^2} - \frac{2}{R^2}\frac{\partial V}{\partial \phi} + \frac{Gr}{8}\,\theta\cos\phi
$$

(4.1)

ii. Angular Momentum Equation:

$$
\frac{\partial V}{\partial t} = -\frac{U}{R}\frac{\partial V}{\partial R} - \frac{V}{R^2}\frac{\partial V}{\partial \phi} - \frac{\partial P}{\partial \phi} + \frac{\partial^2 V}{\partial R^2} - \frac{1}{R}\frac{\partial V}{\partial R}
$$
$$
+ \frac{1}{R^2}\frac{\partial^2 V}{\partial R^2} + \frac{2}{R^2}\frac{\partial U}{\partial \phi} - \frac{Gr}{8}\,\theta\sin\phi
$$

(4.2)

iii. Axial Momentum Equation:

$$\frac{\partial W}{\partial t} = -\frac{U}{R}\frac{\partial W}{\partial R} - \frac{V}{R^2}\frac{\partial W}{\partial \phi} + \frac{U\,W}{R^2} + R$$
$$+ \frac{\partial^2 W}{\partial R^2} - \frac{1}{R}\frac{\partial W}{\partial R} + \frac{1}{R^2}\frac{\partial^2 W}{\partial \phi^2} + \frac{W}{R^2}$$

(4.3)

iv. Continuity Equation:

$$\frac{\partial U}{\partial R} + \frac{1}{R}\frac{\partial V}{\partial \phi} = 0$$

(4.4)

v. Energy Equation:

$$\frac{\partial \theta}{\partial t} = -\frac{U}{R}\frac{\partial \theta}{\partial R} + \frac{U\,\theta}{R^2} - \frac{V}{R^2}\frac{\partial \theta}{\partial \phi} + \frac{(dP/dZ)\,W}{Pr}$$
$$+ \frac{1}{Pr}\{ \frac{\partial^2 \theta}{\partial R^2} - \frac{1}{R}\frac{\partial \theta}{\partial R} + \frac{1}{R^2}\frac{\partial^2 \theta}{\partial \phi^2} + \frac{\theta}{R^2} \}$$

(4.5)

where 't' is the nondimensional time defined as:

$$t = \tau \nu \,/\, r_o^2$$

Boundary conditions (3.21) remain unchanged and are applicable at any time 't'. The initial conditions for this system represent an initial guess for the values of U, V, W, θ, and P. A separate section will be included later to explain their choice.

Although the set of equations (4.1) to (4.5) is sufficient to solve for all the five unknowns, the Marker and Cell or "MAC" method suggests that the pressure should be obtained from a Poisson form of the pressure equation. As will be seen, this equation permits the chronological modification to momentum equations. Moreover, Roache [30] insists that pressure values thus obtained are more accurate. This equation can be easily derived from equations (4.1), (4.2) and (4.4) and after considerable manipulations would take the form:

$$
\begin{aligned}
\nabla^2 P = -\Big[\frac{1}{R} \Big\{ \frac{\partial D}{\partial t} + \frac{1}{R} \Big(U \frac{\partial D}{\partial R} + \frac{V}{R} \frac{\partial D}{\partial \phi} - \frac{U\,D}{R} \Big) \\
- \nabla^2 D + \frac{2}{R} \frac{\partial D}{\partial R} - \frac{D}{R^2} \Big\} \\
+ \frac{Gr}{8} \Big\{ \frac{1}{R^2} \theta \cos\phi - \frac{\cos\phi}{R} \frac{\partial \theta}{\partial R} + \frac{1}{R^2} \sin\phi \frac{\partial \theta}{\partial \phi} \Big\} \\
+ \frac{1}{R^2} \Big\{ \Big(\frac{\partial U}{\partial R} \Big)^2 + \Big(\frac{1}{R} \frac{\partial V}{\partial \phi} \Big)^2 + \frac{(U^2 + V^2)}{R^2} \\
+ \frac{2}{R} \Big(\frac{U}{R} \frac{\partial V}{\partial \phi} - \frac{V}{R} \frac{\partial U}{\partial \phi} \Big) \\
- \frac{\partial}{\partial R} \Big(\frac{U^2 + V^2}{R} \Big) + \frac{2}{R} \frac{\partial U}{\partial \phi} \frac{\partial V}{\partial R} \Big\} \Big]
\end{aligned}
\tag{4.6}
$$

where the term D known as "dilation" is given by:

$$
D = \frac{\partial U}{\partial R} + \frac{1}{R} \frac{\partial V}{\partial \phi}
\tag{4.7}
$$

This term represents the continuity term and could be set equal to zero. In the finite difference form, however, because of the truncation error, this term is never identically zero. If no remedial method is incorporated, this error would accumulate and a drifting and consequently unstable behaviour would be encountered. The Marker and Cell method suggests that at every time step this term should be forced to zero to avoid error accumulation. This is done when the $\partial D/\partial t$ term is expressed in the finite forward difference form as:

$$\frac{\partial D}{\partial t} = \frac{D^{t+\Delta t} - D^t}{\Delta t} \qquad (4.8a)$$

By setting $D^{t+\Delta t}$ equal to zero, then

$$\frac{\partial D}{\partial t} = \frac{-D^t}{\Delta t} \qquad (4.8b)$$

In preparing the finite difference form of equation (4.6), the $\partial D/\partial t$ term was replaced by the form (4.8b).

Two approaches were suggested in the literature for solving Poisson's equation; these are direct methods and the method of false transients. Direct methods are preferable when possible because they require much less computation time. Unfortunately,

these methods cannot be applied here because cylindrical coordinates are being used. Consequently, equation (4.6) was placed in a transient form as follows:

$$\frac{\partial P}{\partial t} = \nabla^2 P - 0 \tag{4.9}$$

where the function "0" is the whole right hand side of equation (4.6).

4.2 THE "MAC" MESH

The cylindrical coordinate equivalent of the "MAC" mesh (proposed originally for cartesian coordinates) is shown in figure 4.1
As can be seen, different variables in a certain cell are defined at different locations. Pressure, axial velocity and temperature (represented by a solid square) are defined at the center of the cell element, while radial and angular velocities (represented by a solid circle and a hexagon, respectively) are defined at the respective radial and angular extremes.

The finite difference spatial derivatives are evaluated by central differences, while forward differences are used for time derivatives. Whenever possible, these derivatives are evaluated over a single mesh spacing. The following examples with reference to figure 4.1 illustrate this procedure.

$$\frac{\partial U(i+\frac{1}{2},j)}{\partial t} \simeq \frac{U(i+\frac{1}{2},j)^{t+\Delta t} - U(i+\frac{1}{2},j)^{t}}{\Delta t} \tag{4.10a}$$
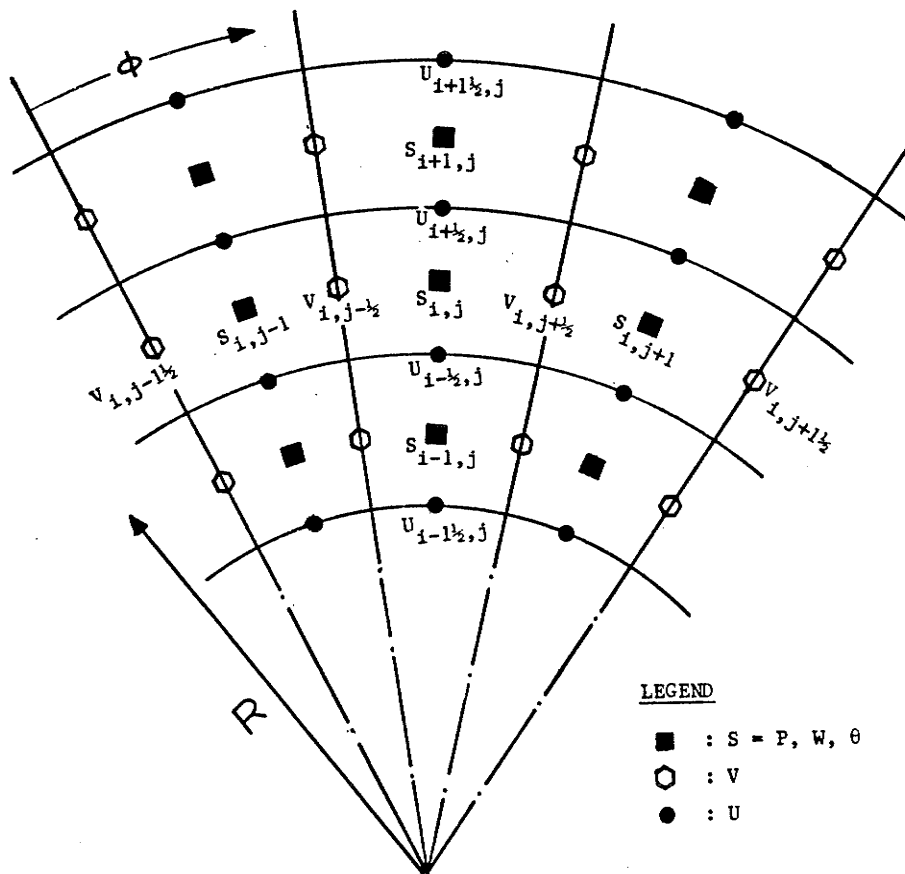
Fig. 4.1 The "MAC" mesh in cylindrical coordinates

$$\frac{\partial P(i,j)^t}{\partial R} \simeq \frac{P(i+1,j)^t - P(i,j)^t}{\Delta R} \tag{4.10b}$$

$$\frac{\partial^2 U(i+\frac{1}{2},j)^t}{\partial R^2} \simeq \frac{U(i+1\frac{1}{2},j)^t + U(i-1\frac{1}{2},j)^t - 2 U(i+\frac{1}{2},j)^t}{(\Delta R)^2} \tag{4.10c}$$

$$\frac{\partial U^2}{\partial R}(i+\frac{1}{2},j)^t \simeq \frac{U^2(i+1\frac{1}{2},j)^t - U^2(1-1\frac{1}{2},j)^t}{2\Delta R} \tag{4.10d}$$

where superscript "t" represents time, and (Δt) represents the time step. Whenever needed, the values of $U(i,j)$ and $V(i,j)$ are defined as:

$$U(i,j)^t \simeq \frac{U(i-\frac{1}{2},j)^t + U(i+\frac{1}{2},j)^t}{2} \tag{4.10e}$$

$$V(i,j)^t \simeq \frac{V(i,j-\frac{1}{2})^t + V(i,j+\frac{1}{2})^t}{2} \tag{4.10f}$$

Product terms like $UV(i,j)$ are evaluated as the product of the averages and not the average of the product, e.g.:

$$U\ V\ (i,j) \simeq \frac{\{U(i+\frac{1}{2},j)+U(i-\frac{1}{2},j)\}\{V(i,j+\frac{1}{2})+V(i,j-\frac{1}{2})\}}{4} \qquad (4.10g)$$

The complete mesh used in the present analysis is given in figure 4.2. Points outside the solution domain were used to facilitate the evaluation of derivatives on the boundary. Boundary conditions (3.21) were imposed such that, whenever a variable does not lie on the boundary, the average of the inner and outer values would satisfy the boundary condition. For example, in figure 4.1 if $U(i+1/2,j)$ is at the circumferential wall (and therefore is of magnitude zero), $W(i+1,j)$ is set to be the negative of $W(i,j)$ so that the radial average of the two is zero at the wall $[W(i+1/2,j)=0]$. The same procedure was employed in the angular direction. For points just below the fin surface e.g., $(k,2)$ in figure 4.2 were treated slightly differently. Since the influence of hot fin surface is believed to be significant in this region, first the radial averages of two neighbouring points $(k-1,2)$ and $k+1,2)$ were calculated and then the symmetry relationship was used:

$$S(k,2) = [S(k+1,2)+S(k-1,2)]/2 \ldots \text{(average)}$$

$$S(k,1) = S(k,2) \ldots\ldots\ldots\ldots\ldots \text{(symmetry)}$$

Central differences in the R and ϕ direction (illustrated in the previous examples) were possible everywhere in the core re-
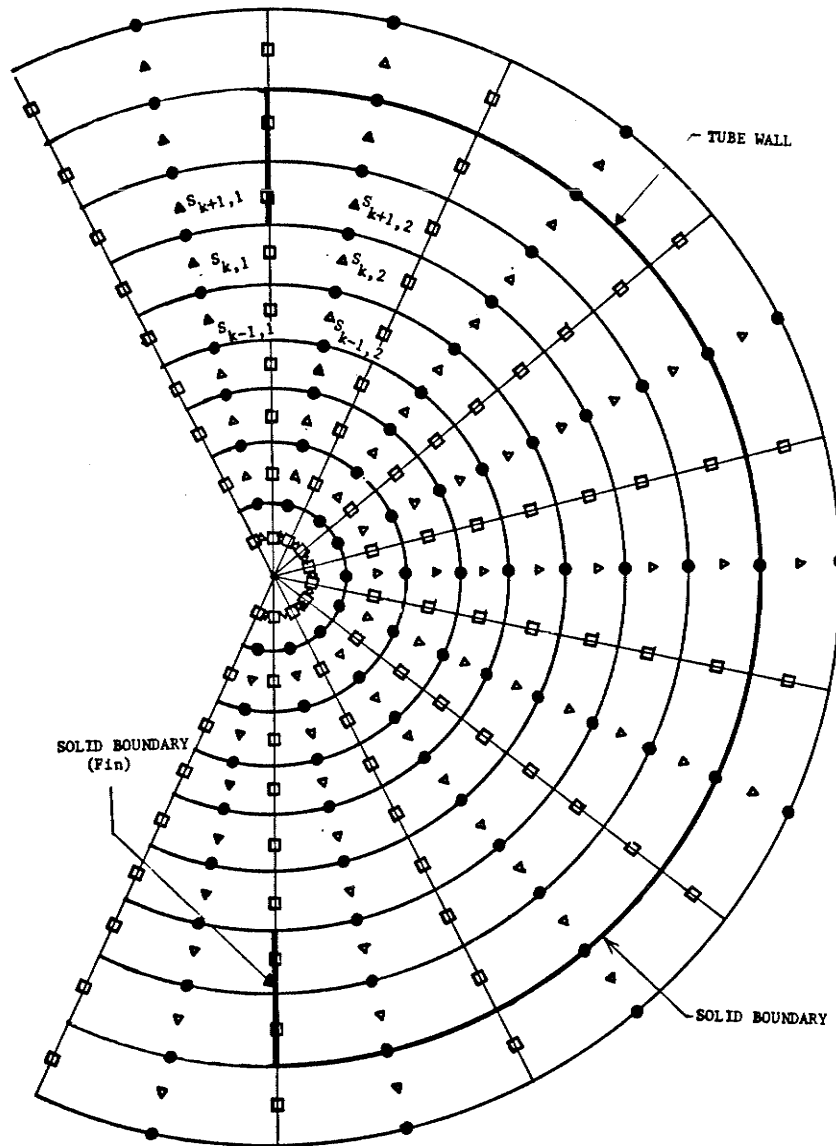
Fig. 4.2 The complete mesh used in the present analysis

gion.   However, along the first radial line (i=1/2), the central difference formulation was modified in the R direction. Radial derivatives of V, W, θ and P were evaluated so that the effect of their zero magnitude at the origin could be incorporated. Figure 4.3 illustrates this situation.

Using the Taylor series expansion, the first and the second radial derivatives can be formulated as:

$$\frac{\partial S(\frac{1}{2},j)^t}{\partial R} = \frac{1/2\ S(\frac{1}{2},j)^t + 2/3\ S(1\frac{1}{2},j)^t - 1/10\ S(2\frac{1}{2},j)^t}{\Delta R} \qquad (4.11)$$

$$\frac{\partial^2 S(\frac{1}{2},j)^t}{\partial R^2} = \frac{-5\ S(\frac{1}{2},j)^t + 2\ S(1\frac{1}{2},j)^t - 2/10\ S(2\frac{1}{2},j)^t}{(\Delta R)^2} \qquad (4.12)$$

where S stands for V, W, P or θ.

Any other significant feature or special treatment required will be mentioned in future sections where the evaluation of these variables is discussed.

$$S \equiv V, W, P \text{ or } \theta$$
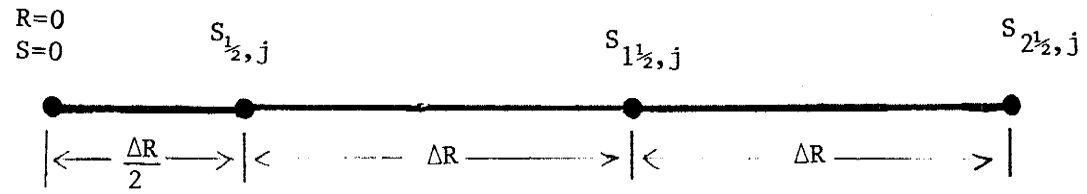
Fig. 4.3 Radial derivatives along i=½

4.3   SOLUTION PROCEDURE

Figure 4.4 outlines the solution alogorithm used to solve the present problem. An initial guess (t=0) for the unknown variables was provided to the program. Solution process started with the evaluation of pressure at t+Δt from the Poisson equation. The pressure values thus obtained were used in the evaluation of radial and angular velocities. With known values of U and V, the axial momentum equation was solved for unknown values of W and energy equation for the unknown values of θ at t=Δt. Progress in time was maintained by repeating the above steps until the steady state solution was established. Various features of the solution procedure are discussed in the subsequent sections.

4.3.1   Initial Guess

To start the computations, initial values of U,V,W,P and θ at t=0 must be specified. Since the transient solutions are not the objective of this analysis, the choice of initial values is arbitrary. The only factors considered were ensuring numerical stability and conserving computation time by choosing initial conditions as close as possible to the final steady state solution.

For smooth tubes and Gr=0 and 100, the velocity and temperature profiles obtained from the forced convection theory served as initial values. For the finned tubes, the solution of reference [25] with a few modifications was used for Gr=0 and 100. For any geometry, after establishing the solution for Gr=100, solutions
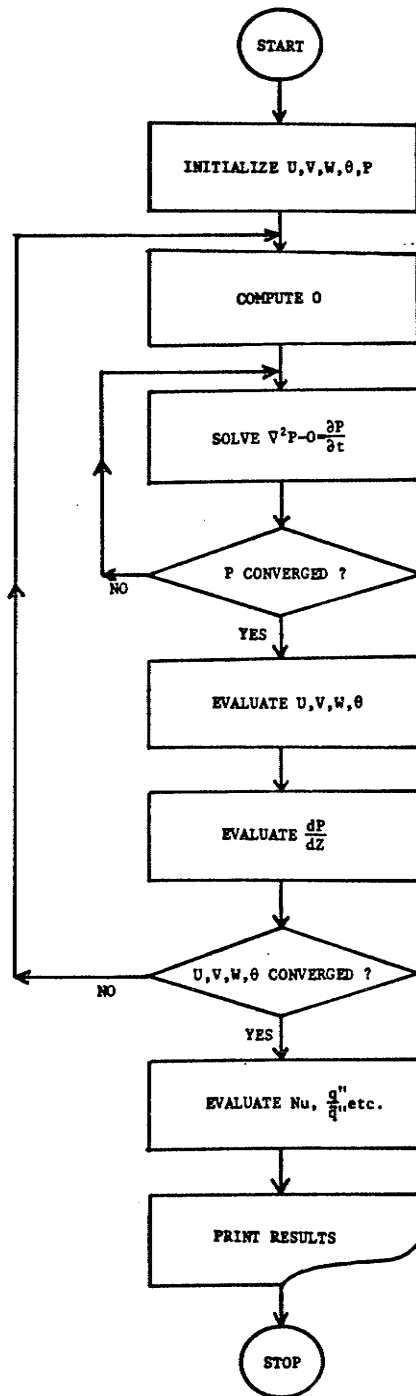
Fig. 4.4 Flow chart of the computational scheme

were then obtained for Gr=10^3,10^4,10^5 and 10^6. The final solution for any of these values of Gr was taken as the initial values of the next higher value of Gr. This procedure proved to be very stable as well as efficient in terms of computer time.

4.3.2 Solution of Poisson's equation

Equation (4.9) in finite difference form is given by:

$$\frac{P(i,j)^{t+\Delta t} - P(i,j)^t}{\Delta t} = \{\nabla^2 P(i,j) - O(i,j)\}^t \qquad (4.13a)$$

or:

$$P(i,j)^{t+\Delta t} = P(i,j)^t + \Delta t\{\nabla^2 P(i,j) - O(i,j)\}^t \qquad (4.13b)$$

The term $[\nabla^2 P-O]$ on the right hand side of equation (4.13b) represents the residuals which must be reduced to zero at all mesh points when steady state is reached. This was used as one of the convergence criterion for pressure and is discussed in a later section.

The term O representing the right hand side of equation (4.6) was decomposed into three parts:

$$O = DD + SS + TT$$

where:

DD = all terms involving "D"

SS = all terms not involving "D" or "θ"

TT = all terms involving "θ"

With available values of O and P at time t, new values of pressure were calculated for time $t + \Delta t$. Progress in time was continued till convergence of pressure was achieved and the final values of pressure were used in the calculations of new radial and angular velocities.

At the circumferential boundary (tube wall), the radial momentum equation can be used to obtain the pressure values. The radial pressure gradient based on momentum equation (4.1) can be written as:

$$\frac{\partial P}{\partial R} = \frac{1}{R} \frac{\partial^2 U}{\partial R^2} - \frac{1}{R^2} \frac{\partial U}{\partial R} \tag{4.14}$$

Equation (4.14) can be used to calculate the pressure at the outside circumferential nodes. However Roache [30] reported that this plausible method does not converge. Miyakoda [31] explained that this approach would cause the solution to drift endlessly. He suggested that instead of applying equation (4.14) directly, this equation should be incorporated into the difference scheme (4.13) · at interior points adjacent to the boundary. Following

this approach, equation (4.13) for these points takes the follow-
ing form:

$$P(i,j)^{t+\Delta t} = P(i,j)^t + \Delta t\{\nabla^2 P^*(i,j) - O(i,j)\} \qquad (4.15)$$

where, in the $\nabla^2 P^*$ term, all radial derivatives for pressure
were calculated from equation (4.14). This caused terms like
$P(i,j)^{t+\Delta t}$ to appear on the right hand side of equation (4.15).
This equation was therefore solved algebraically for $P(i,j)^{t+\Delta t}$
After convergence was achieved, the pressure values at nodes out-
side the flow domain were obtained from equation (4.14). This
completed the evaluation of pressure at any time step.

4.3.3 Solution to U,V,W and θ

Starting with values of U, V, W, P and θ at time t, method
to evaluate the values of P at time t +Δt was shown in the pre-
vious section. Using the new values of P, equations (4.1), (4.2),
(4.4) and (4.5) were used to calculate the corresponding values
of U, V, W and θ, respectively, at time t +Δt. The finite dif-
ference form of these equations [similar to (4.13)] were swept
once. All spatial derivatives were calculated in terms of vari-
able values at the previous time step (for the first time step,
the initial guess was used).

All fields thus obtained were tested for convergence by comparing the fields at time t +Δt to those at time t. If convergence was not observed, computations were advanced to a new time step. This process was continued until all fields were converged. Convergence criteria will be discussed in a later section. The final converged fields were used to calculate the overall fluid flow and heat transfer parameters.

4.4 CONVERGENCE CRITERIA

For any of the variables U, V, W, P or θ (in general S), the usual criteria for convergence is:

$$\left| \frac{S(i,j)^{t+\Delta t} - S(i,j)^{t}}{S(i,j)^{t}} \right| \leqslant d \qquad (4.16)$$

The value of "d" can be made arbitrarily small and in literature, its value varied from 10^{-3} to 10^{-8}, from which, it may be concluded that the whole idea is not rational [30].

The values of d in equation (4.16) can be made arbitrarily small and still possibly stop the computations prematurely. This then can possibly be avoided by taking first derivatives:

$$\left| \frac{\dfrac{\partial s^{t+\Delta t}}{\partial L} - \dfrac{\partial s^{t}}{\partial L}}{\dfrac{\partial s^{t}}{\partial L}} \right| \leqslant d$$

where $L \equiv R$ or ϕ or both.   A number of time steps can also be carried out before testing for convergence, i.e. :

$$\left| \frac{s^{t+n\Delta t} - s^{t}}{s^{t}} \right| \leqslant d$$

where n is arbitrary. Usual values in the literature are within the range 10 - 1000.

Unfortunately, none of these criteria offer a satisfactory answer to the problem and one is restricted in proceeding with more time steps on account of limited computational time.   The approach adopted for convergence in this analysis is also subjective. Pressure, being the most sensitive and crucial parameter was tested against some apparent pitfalls. It was found that rapid progress in time could be made by relaxing the convergence criterion for pressure at the initial stages.   Criterion (4.16) with d being 10^{-4} was used in this process.   Poisson's equation was obviously not strictly satisfied but convergence criterion (4.16) with $d = 10^{-6}$ was applied for U, V, W and θ. Once this solution was established, equation (4.13) was used further until all the residuals ($\nabla^2 P - 0$) were within $\pm 10^{-2}$. It was found that at

this small values of residuals, convergence criterion (4.16) when applied to ∂P/∂r and ∂P/∂∅ would give values of d almost equal to zero. This then provided refined values of pressure; the rest of the variables (U,V,W, and θ) were computed to satisfy criterion (4.16) with d = 10^{-5}. In some cases, the value of d was decreased to 10^{-6} but no significant difference was noted.

4.5   SELECTION OF THE TIME STEP AND MESH SIZE

It is imperative that a value of Δt be selected in such a way that convergence is assured. A close examination of equations (4.1) to (4.6) revealed that if a criterion is established on the basis of Poisson's equation, it would also satisfy equations (4.1) to (4.5).

The most crucial location was the first radial line (R=1/2 ΔR) where values of ∂P/∂R and ∂²P/∂R² were defined using equations (4.11) and (4.12), respectively. At this value of radius, equation (4.13) is written as:

$$\frac{\partial P}{\partial t} = \{ \frac{\partial^2 P}{\partial R^2} + \frac{1}{R}\frac{\partial P}{\partial R} + \frac{1}{R^2}\frac{\partial^2 P}{\partial \phi^2} - 0 \}_{R=\Delta R/2} \qquad (4.17)$$

In finite difference form, using equations (4.11) and (4.12) for ∂P/∂R and ∂²P/∂R²respectively, and collecting terms involving P(i,j)^t at the right hand side, we get

$$P(i,j)^{t+\Delta t} = P(i,j)^t \{ 1 + \Delta t \, (\frac{1}{\Delta R^2} - \frac{5}{\Delta R^2} - \frac{8}{\Delta R^2 \Delta \phi^2})\} + \text{other terms.}$$

For convergence, the coefficient of $P(i,j)^t$ should be positive, i.e.,

$$1 - \frac{4\Delta t}{(\Delta R)^2} - \frac{8\Delta t}{(\Delta R)^2 (\Delta\phi)^2} \geqslant 0$$

or;

$$(\Delta t)_{max} \leqslant \frac{(\Delta R)^2}{4(1 + \frac{2}{(\Delta\phi)^2})} \qquad (4.18)$$

This condition imposes a severe restriction on the size of mesh which can be used. As can be clearly seen, the use of a very fine mesh requires extremely small values of Δt and hence very large computational time.

For the present analysis, a mesh with $\Delta R = 0.125$ and $\Delta\phi = \pi/7$ was used. According to equation (4.18), the maximum possible value of Δt for this mesh is 0.000357. To insure convergence, the more conservative value of $\Delta t = 0.000125$ was used. With this value of Δt, a stable numerical behaviour was observed for all geometries and all Grashof numbers considered in this investigation. The total computational time necessary to establish the steady state solution for any combination of geometry and Grashof

number would naturally depend on the initial values. With the scheme followed for establishing the initial values, it was observed that the necessary computational time was in the order of 1/2 minute at Gr=0, but increased to about 1/2 hour as Grashof number increased to 10^6.

As will be shown later, the accuracy of the present results is not as high as was hoped at the beginning of this investigation. This is due to the coarse mesh used here. Had we used a finer mesh with $\Delta R=0.0625$ and $\Delta \phi = \pi/14$ (i.e., four times as many mesh points), the maximum value of Δt predicted by equation (4.18) would have been about 0.0000239. This value is about 1/15 of the corresponding value for the used mesh. Hence, computational times for the finer mesh would have to increase by a factor of 60 over those for the coarse mesh. It was judged that this increase is beyond the availibility of computer time.

Chapter V

RESULTS AND DISCUSSION

In the present analysis, velocity, temperature and pressure distributions were obtained for five tube geometries. They correspond to H=0 (smooth tube), H=0.25, H=0.50, H=0.75 and H=1.0. Variable heating loads (Gr = 0 - 10⁶) were applied and a Prandtl number of 0.7 corresponding to air was consistently used. The mesh shown in figure 4.3 was used to obtain all the results. It is conceded that, the use of this course mesh increased the truncation errors, however, a close examination of equation (4.18) reveals that even a slightly finer mesh would require considerably more computer time, which is obviously scarce and expensive.

Based on velocity and temperature distributions, important engineering parameters were calculated. In order to provide a better illustration, values of U,V,W and θ were retransformed into the U^*, V^*, W^* and $θ^*$ system discussed in chapter III. Values of U^* and V^* which will be reported in this chapter are defined at the center of the mesh elements (where W^*, P and $θ^*$ were already defined) by using the averaging procedure described in chapter IV.

This chapter explains the nature of fluid flow i.e., the velocity distributions and the nature of heat transfer i.e., the temperature distribution. Whenever possible, these explanations

are carried out in perspective of two significant factors viz, the influence of heating loads (expressed in terms of Grashof number :Gr) and the non-dimensional fin height (H). Overall engineering parameters and their variations are then explained on the basis of said distributions.

5.1   VELOCITY FIELDS

The three components of the velocity vector are the radial, angular and axial velocities. In pure forced convection, the only non-zero component of the velocity vector is the axial velocity which exists due to the axial pressure gradient.   On account of density gradients across the tube cross section,   secondary or buoyancy induced flow is generated, which is the basis of free convection. The secondary flow is perpendicular to the main flow, and non-zero values of the radial and angular velocities describe its pattern.

5.1.1   Secondary velocities

Four graphs are presented to describe the picture of secondary flow for each geometry. Variation of radial velocity in the vicinity of vertical symmetry plane is shown in the first two graphs, while the angular variation of U^* along R=0.5625 is illustrated in the third graph. The fourth graph shows the variation of the angular velocity along the horizontal plane $\phi=90°$. These four graphs are therefore used to determine a picture of the secondary flow.   For the cases of H=0 and H=0.5,   secondary

velocity vectors (U^*+V^*) are plotted at Gr=10⁶ to see the secondary flow exactly.

For smooth tubes (H=0), figures 5.1 to 5.4 are the afore mentioned four graphs. In figure 5.1, radial variation of U^* along the ϕ=12.85° line has been plotted. The location R=1 corresponds to the tube wall where all the velocities are zero. The negative U^* values indicate that the fluid is moving downwards towards the center. For Gr=1000, which correspond to a small heating load, the values of U^* are almost negligible. This implies that upto this value, free convection effects are almost non-existent. As the heat input is increased (higher values of Gr), fluid is seen to be moving faster towards the center. The maximum value of U^* is seen to exist near the center for all values of Gr. In figure 5.2, the radial variation of U^* along ϕ=167.15° line is plotted. This figure is a continuation of the previous figure. Fluid is seen to be moving past the center of the tube towards the bottom wall (R=1). For Gr=10³ to 10⁵, maximum value of U^* exists very close to the center however, for Gr=10⁶ this maximum occurs in the bottom part of the tube. As the wall is approached, flow retards and the magnitude of U^* ultimately goes to zero at the wall. Figure 5.3 shows the angular variation of U^* around the R=0.5625 radial line. Along this line, the flow is moving inwards in the upper half of the tube, while it is coming out in the bottom half. Because of this feature, the mass balance is seen to be satisfied around the R=0.5625 radial line. It is observed that the maximum positive value of radial
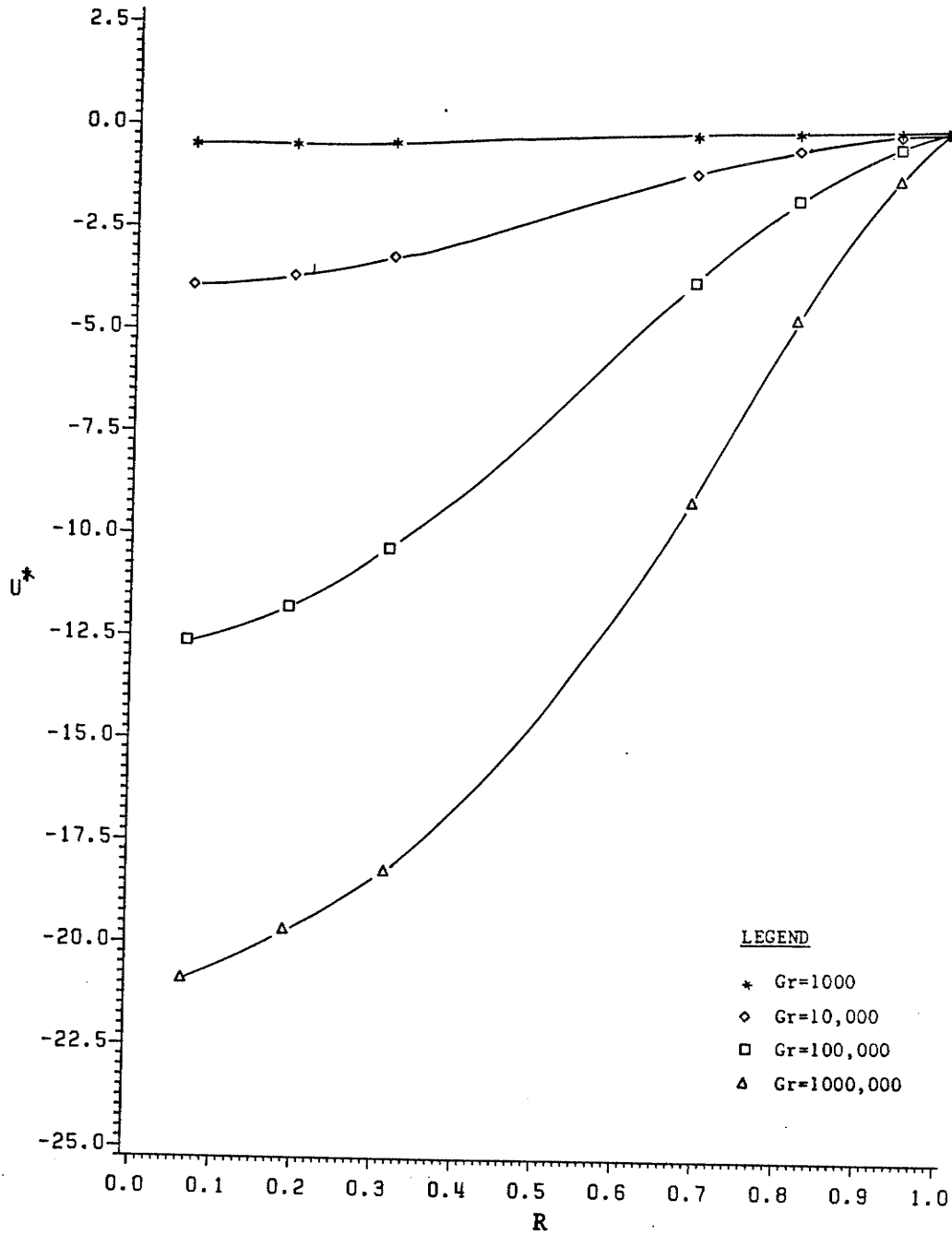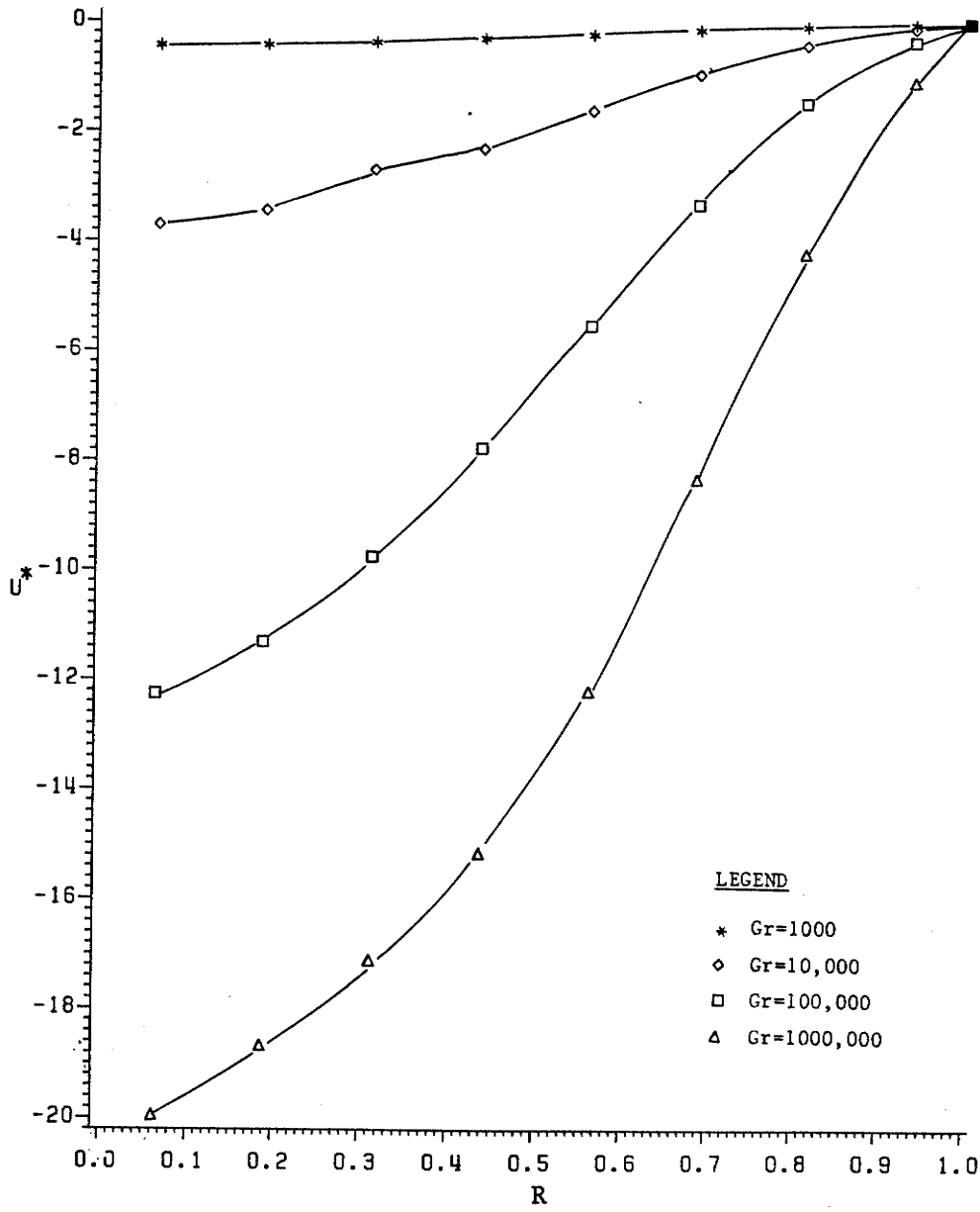
Fig. 5.1 Radial Variation of Radial Velocity (ϕ=12.85°, H=0.0)
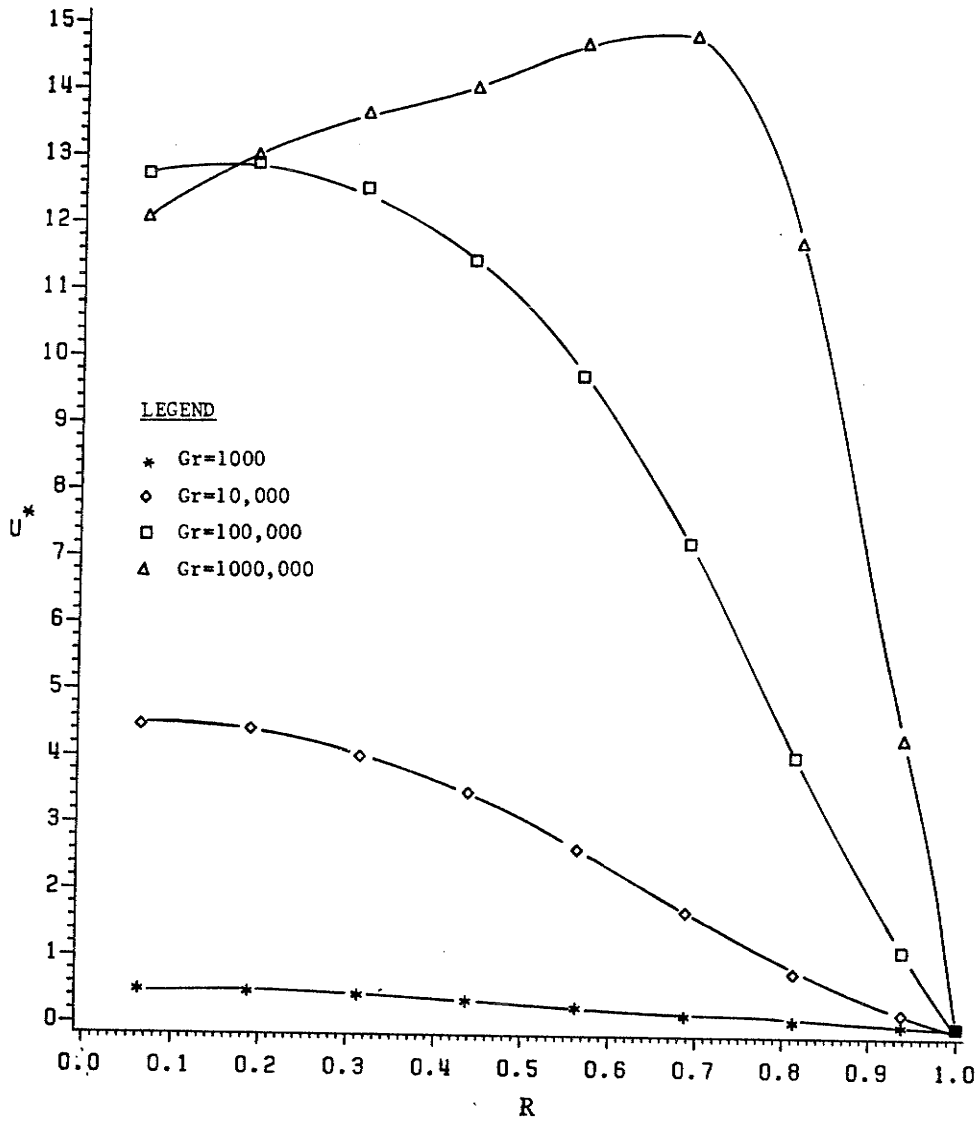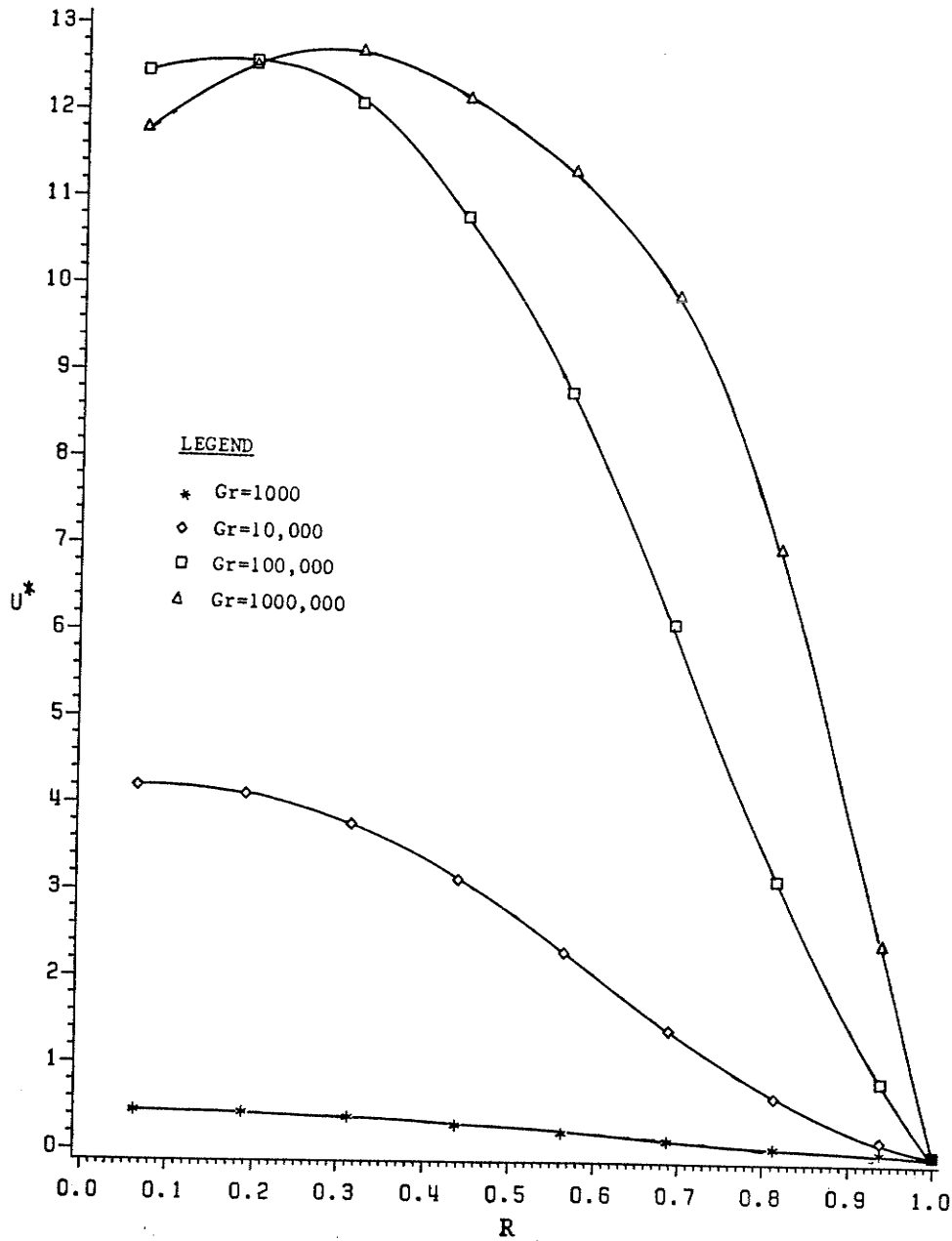
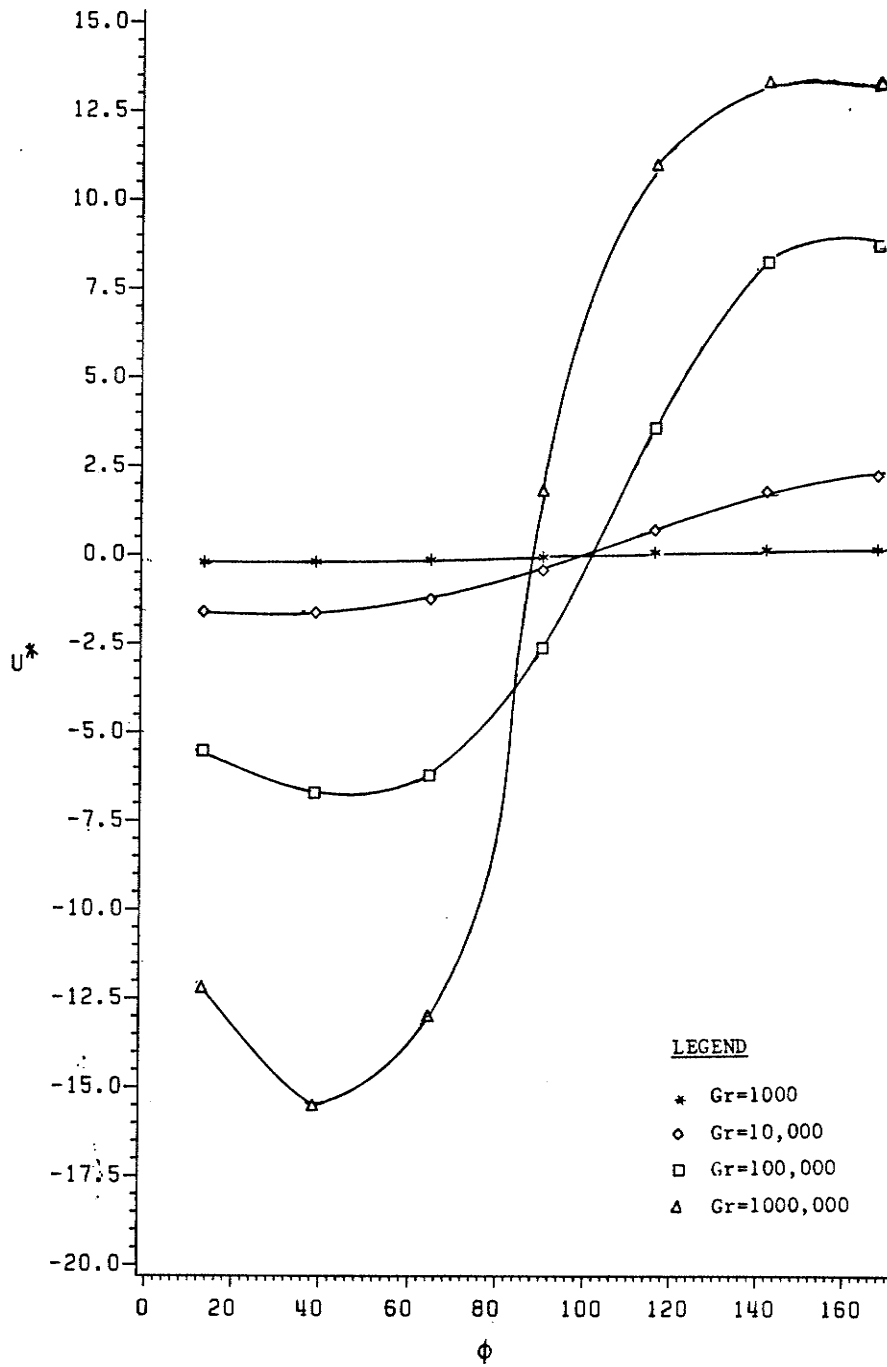Fig. 5.2 Radial Variation of Radial Velocity ($\phi=167.15^\circ$, H=0.0)
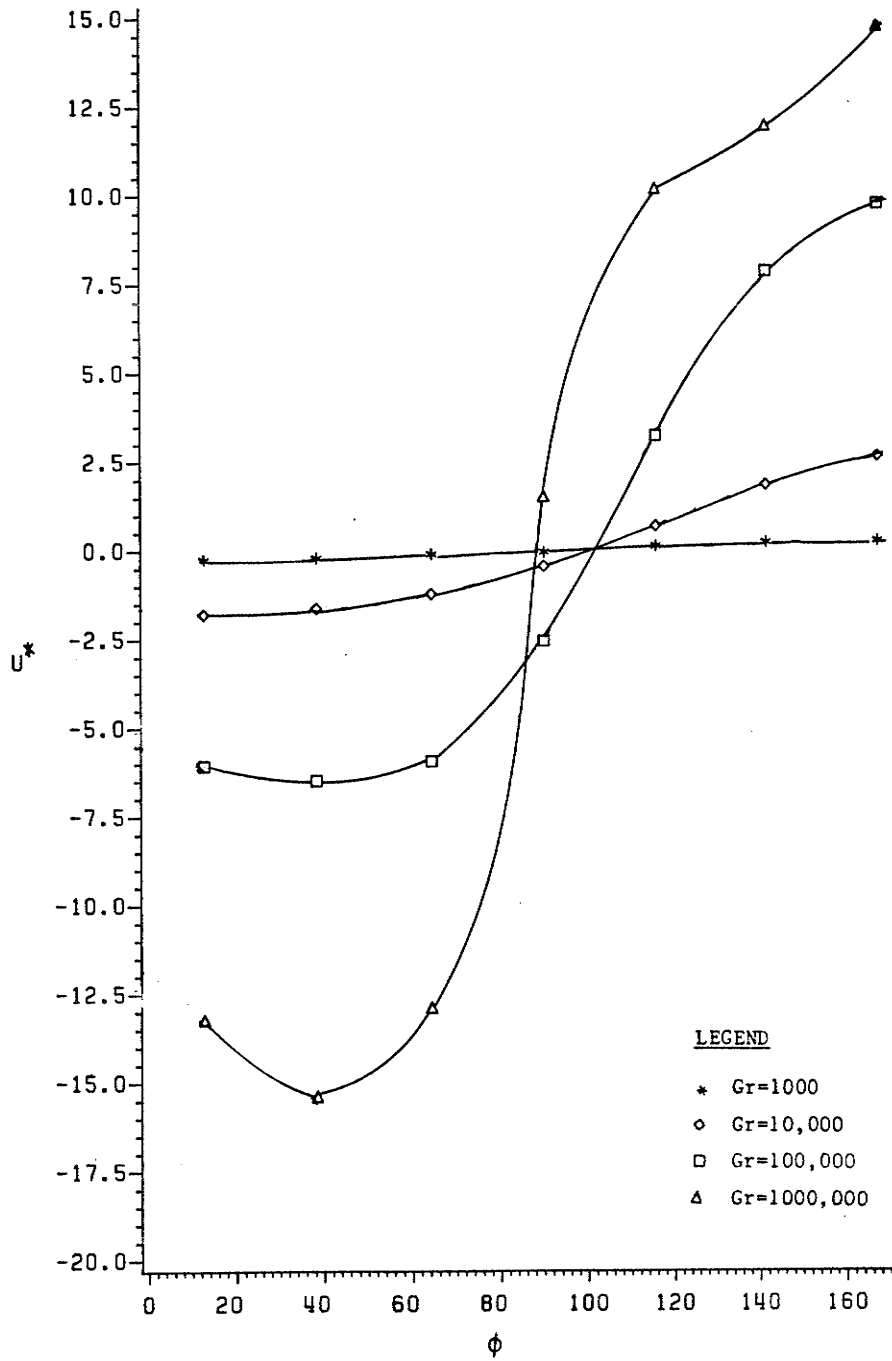
Fig. 5.3 Angular Variation of Radial Velocity (R=0.5625, H=0.0)
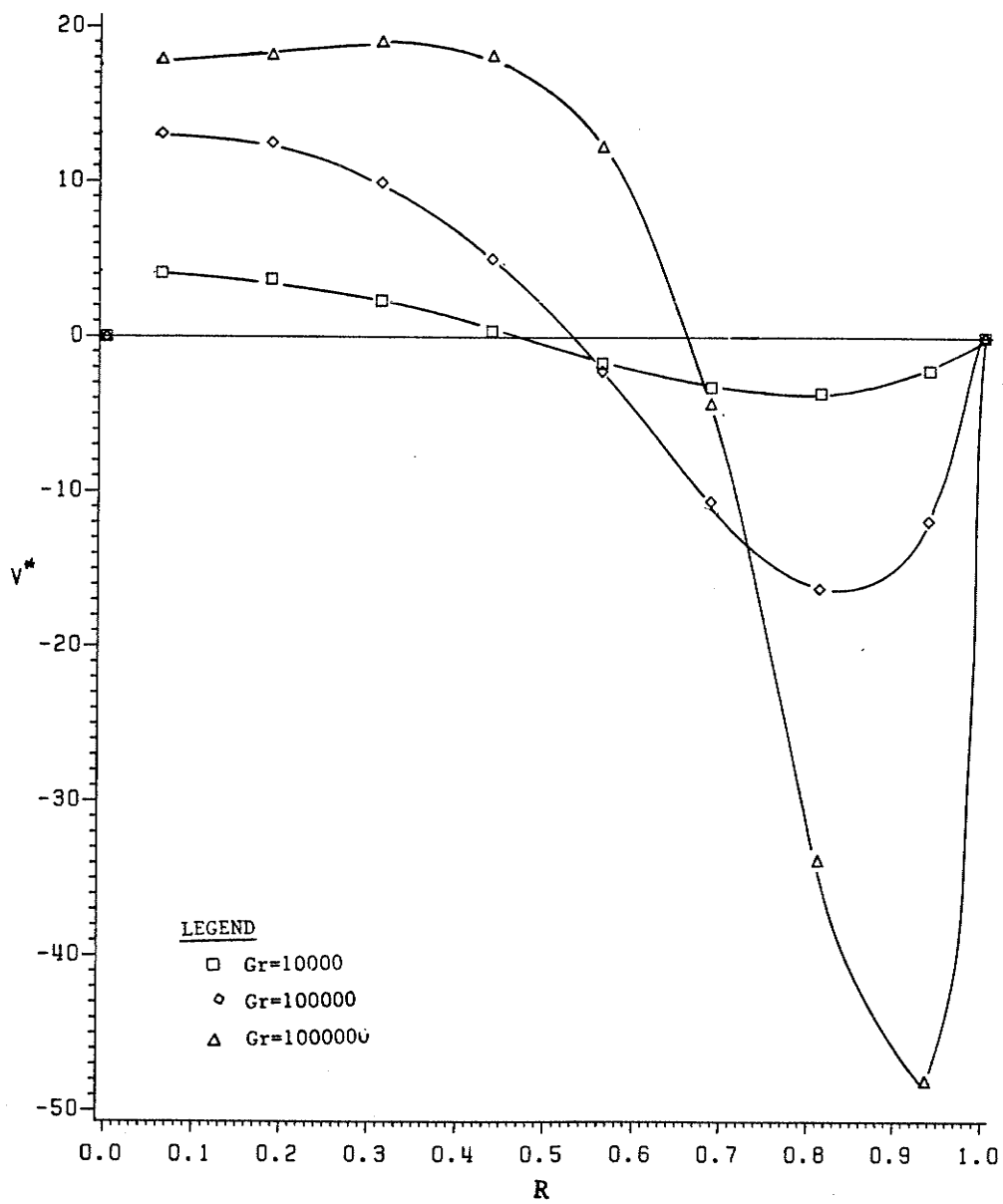
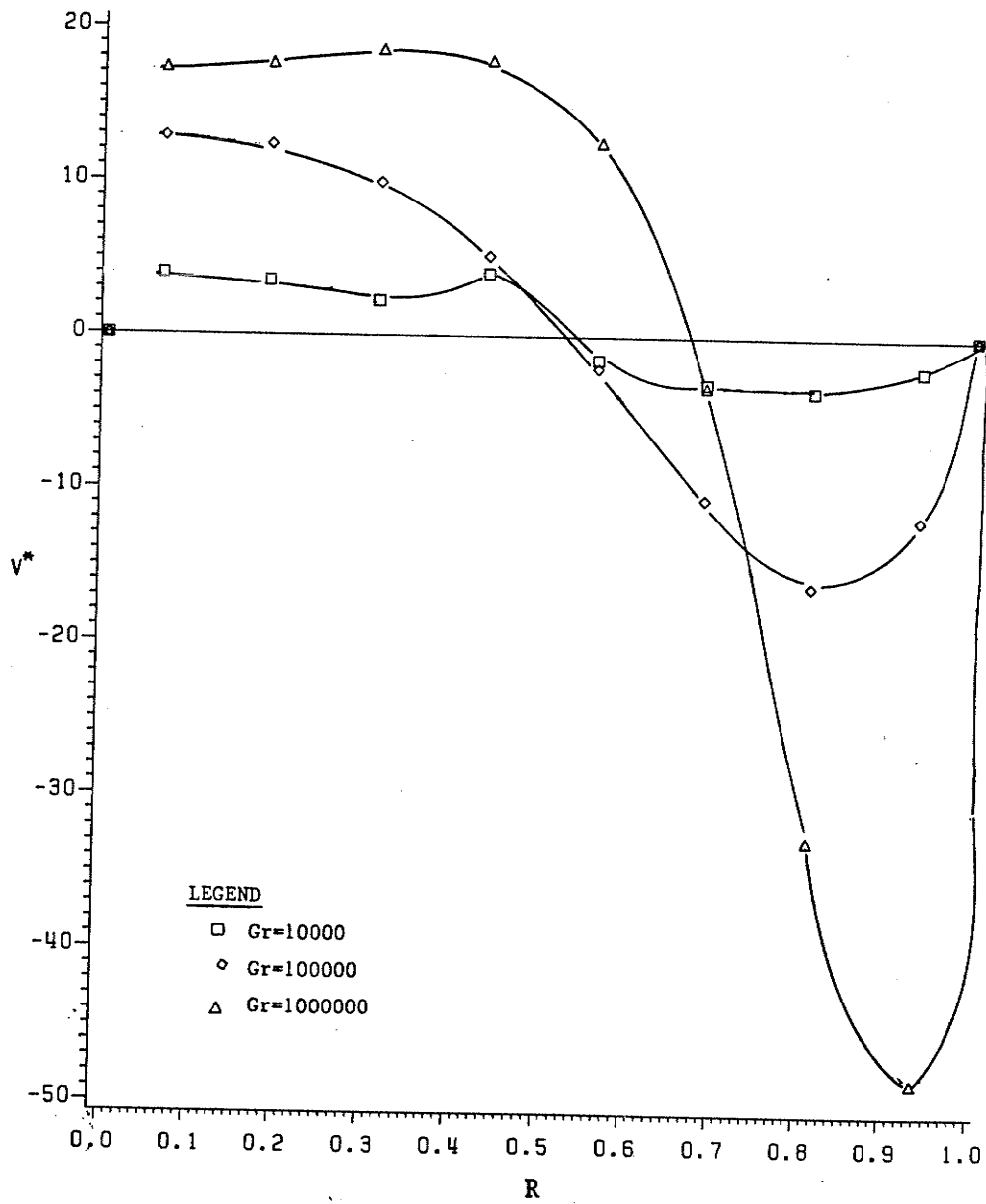Fig. 5.4 Radial Variation of Angular Velocity ($\phi=90^\circ$, H=0.0)
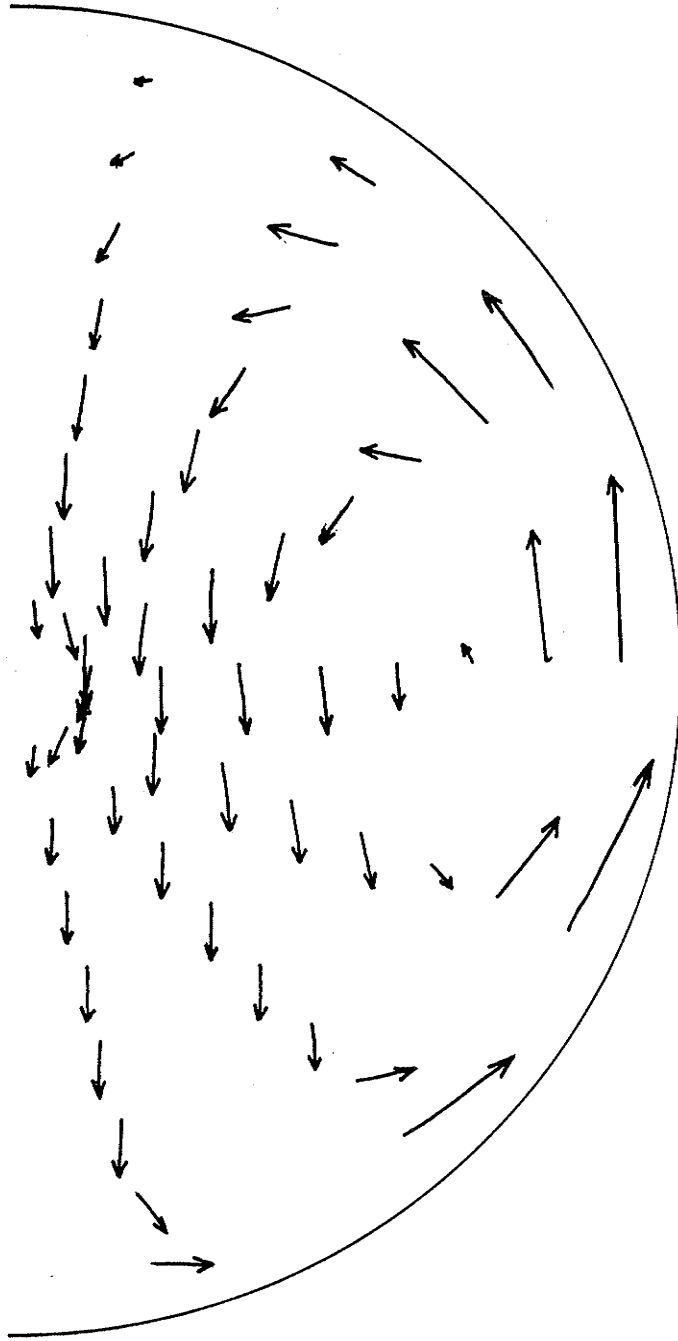
Fig. 5.5 Secondary velocity Vectors $(H=0, Gr=10^6)$

velocity exists along the bottom part of the vertical center plane. Positive values of U^* in the bottom part indicate a downward flow. Thus it can be concluded that colder and hence heavier fluid exists along the $\phi=180°$ line. In figure 5.4, variation of angular velocity is plotted along the horizontal center plane of the tube. Upto R=0.45 - 0.65 a downward flow is observed. Near the tube's circular wall, large negative values of V^* imply an upward motion.

With these graphs, a general picture of secondary flow in smooth tubes can be formed. Since the only hot surface encountered by the fluid is the circular wall, fluid adjacent to the wall is hot and lighter and hence moves upward. It replaces the cold and hence heavier fluid in the upper half of the tube, which in turn comes down in the region away from the circular wall. This picture thus suggests a single loop pattern (known as primary loop) of the secondary flow. Secondary velocity vectors confirming these arguments are plotted in figure 5.5.

Figures 5.6 to 5.9 are the four graphs for the case of H=0.25. At a first glance, these curves look similar to their smooth tube counterparts. In fact, the pattern of secondary flow is almost similar in the two cases. However, now the order of magnitude of secondary velocities is slightly smaller. Two reasons are conceivable for this decrease. First is the fact that the introduction of additional solid surface in the flow domain is causing additional surface friction. More important however is the reason that the vertical center plane is now not a complete
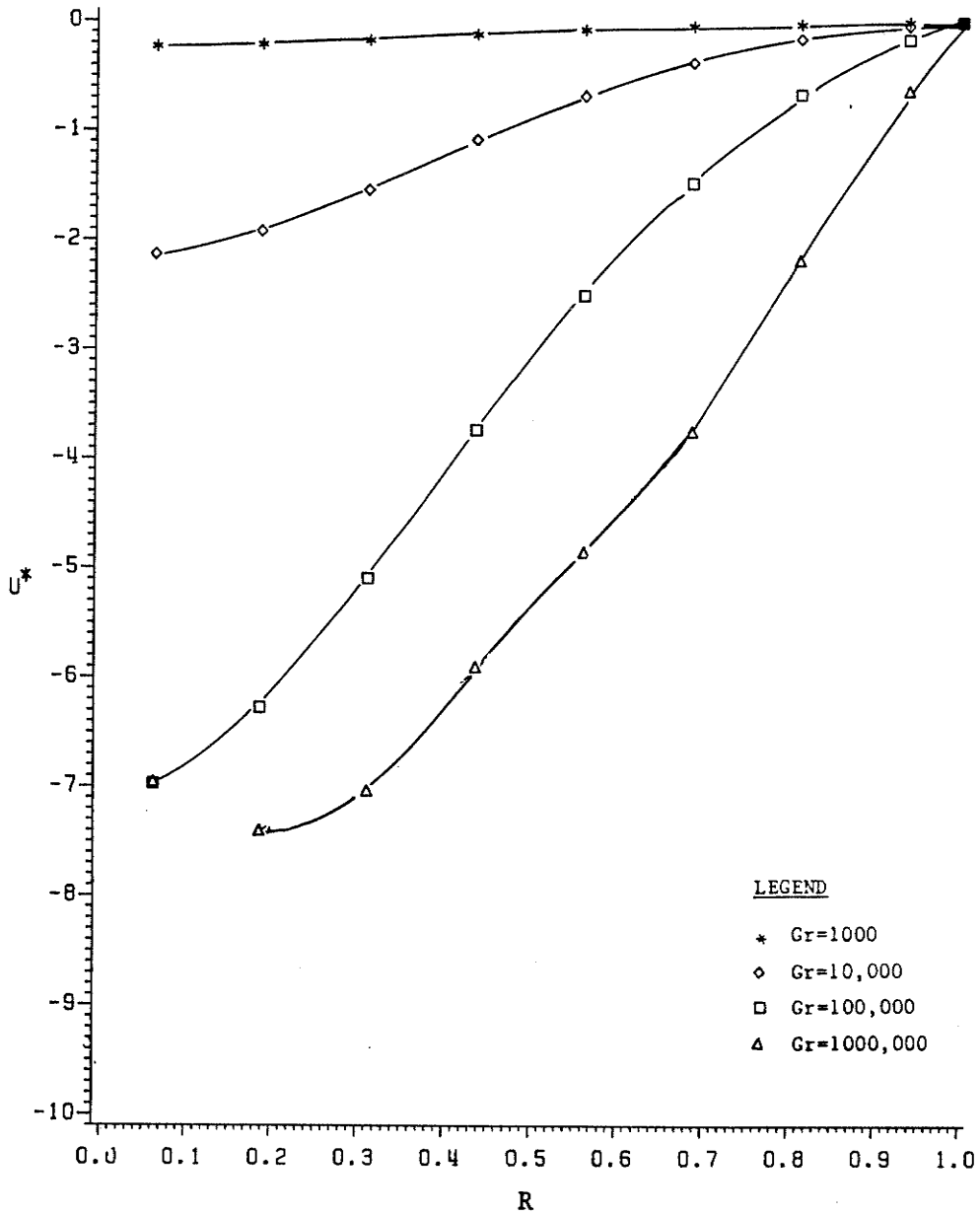
Fig. 5.6 Radial Variation of Radial Velocity ($\phi=12.85°$, H=0.25)

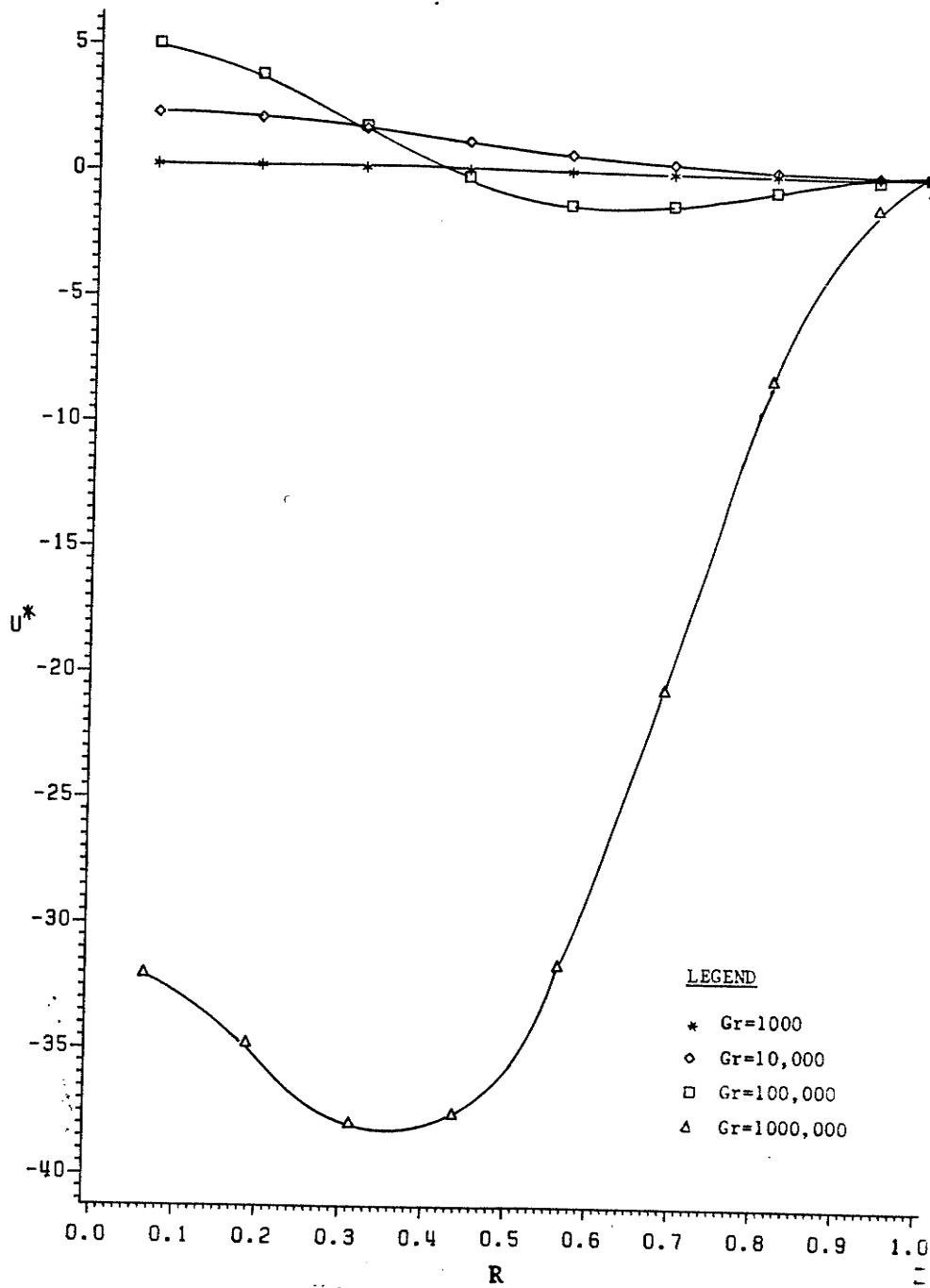Fig 5.7 Radial Variation of Radial Velocity ($\phi=167.15°$, H=0.25)

Fig. 5.8 Angular Variation of Radial Velocity (R=0.5625, H=0.25)

Fig. 5.9 Radial Variation of Angular Velocity ($\phi=90^{\circ}$, H=0.25)

free surface. Longitudinal short fins have the effect of heating
the fluid in their vicinity. Hence in that region, a tendency of
upward motion is established. Fins are however short, and this
tendency is not strong enough to reverse the flow pattern. The
main heat transfer surface is still the circular wall as far as
secondary flow is concerned. Fluid is seen to be moving up near
the wall in figure 5.9 and moving down in the region away from
the wall. In figure 5.7 an interesting difference from that of
figure 5.2 is observed. It is the effect of bottom fin at Gr=10^6:
unlike the smooth tube case, maximum positive values of U* has
shifted close to the center. It can be explained on the basis
that fluid close to the fin has retarded on account of buoyancy
effects, and hence is slow. Unlike figure 5.3 all curves in fig-
ure 5.8 are flatter near ϕ=180°. This implies that the maximum
positive values of U* (which is an indicator of downward motion
of the cold fluid) is distributed over a region close to the bot-
tom half of the vertical center line, and is not strictly limited
to it. This then suggests that, although the coldest fluid exists
in the bottom half of the tube, it is no longer present at the
vertical center line but is to be found slightly away from it.

The case of H=0.5 is shown in figures 5.10 to 5.13. In the
vicinity of the upper half of the vertical center plane, as shown
in figure 5.10, fluid is seen to be moving downwards from the
tube wall to the center. The magnitudes of the radial velocities
are greatly reduced from the previous two cases. This implies
that the presence of a longer hot fin is increasing the tendency

Fig.5.10 Radial Variation of Radial Velocity ($\phi=12.85^{\circ}$, H=0.50)

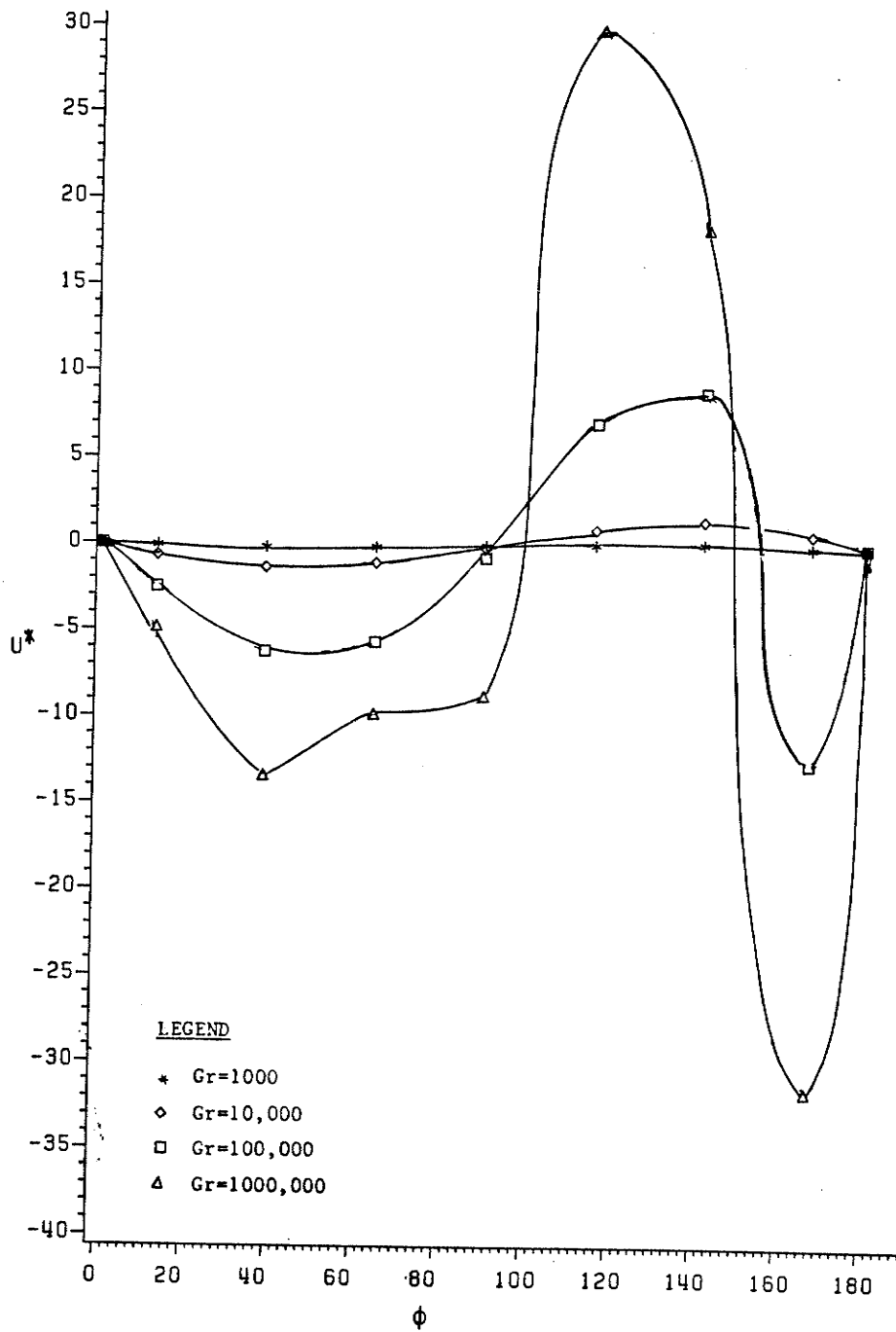Fig. 5.11 Radial Variation of Radial Velocity ($\phi=167.15^\circ$, H=0.50)

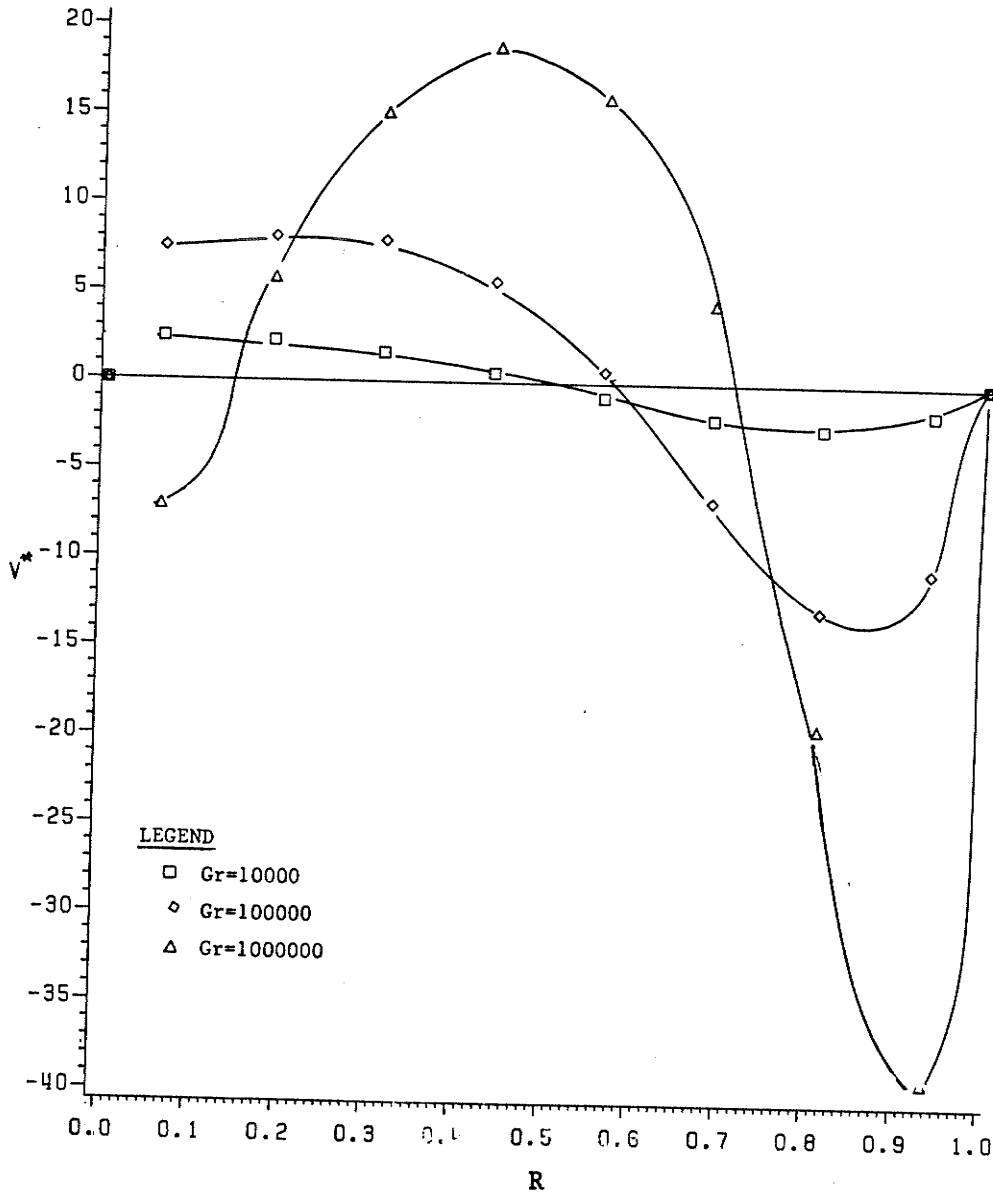Fig. 5.12 Angular Variation of Radial Velocity (R=0.5625, H=0.50)

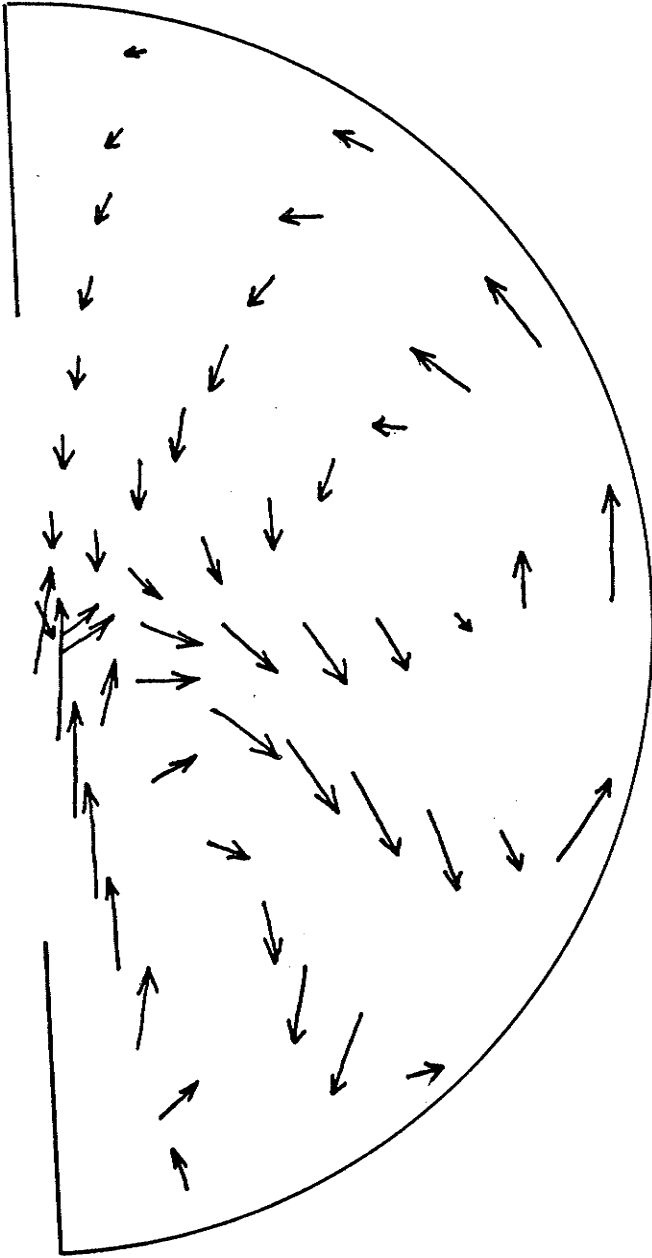Fig. 5.13 Radial Variation of Angular Velocity ($\phi=90^{\circ}$, H=0.50)

Fig. 5.14 Secondary Velocity Vectors (H=0.5 Gr=10⁶)

of upward motion even more. Magnitudes of U^* for the cases of Gr=10^5 and 10^6 are not extremely different, which was not the case for shorter fins. Near the bottom fin surface illustrated in figure 5.11, the downward motion of fluid is limited upto Gr=10^4 only. At Gr=10^5 however, fluid exhibits a different pattern. Near the center, it is moving down with a small radial velocity, and in the vicinity of the fin, its motion is upwards. This is due to longer, heated surface of the fin. At Gr=10^6 where maximum heating load is encountered, fluid is seen to be moving upwards along the entire lower half of the vertical center line. For this case, the maximum negative value of U^* exists at R=0.35. In figure 5.12 where angular variation of U^* is plotted around R=0.5625, values of U^* for Gr=10^3 and 10^4 are almost negligible. For higher heating loads however, fluid is seen to be moving into R=0.5625 radial line in the upper half of the tube. This implies a downward motion. From ϕ=90° to about 150° fluid is coming out radially downwards. For values of ϕ greater than 150°, fluid has an upward motion. This figure in conjunction with figure 5.13 suggest the secondary flow to be in the form of more than one loop (other loops are known as secondary loops), which is a deviation from the previous cases. In order to verify the conclusions drawn from the above four figures, figure 5.14 is plotted which shows the secondary velocity vectors at Gr=10^6.

The case of H=0.75 presents a completely different picture. Figure 5.15 to 5.18 illustrate the nature of secondary flow for this relatively long fin. Now, 75% of the vertical center plane
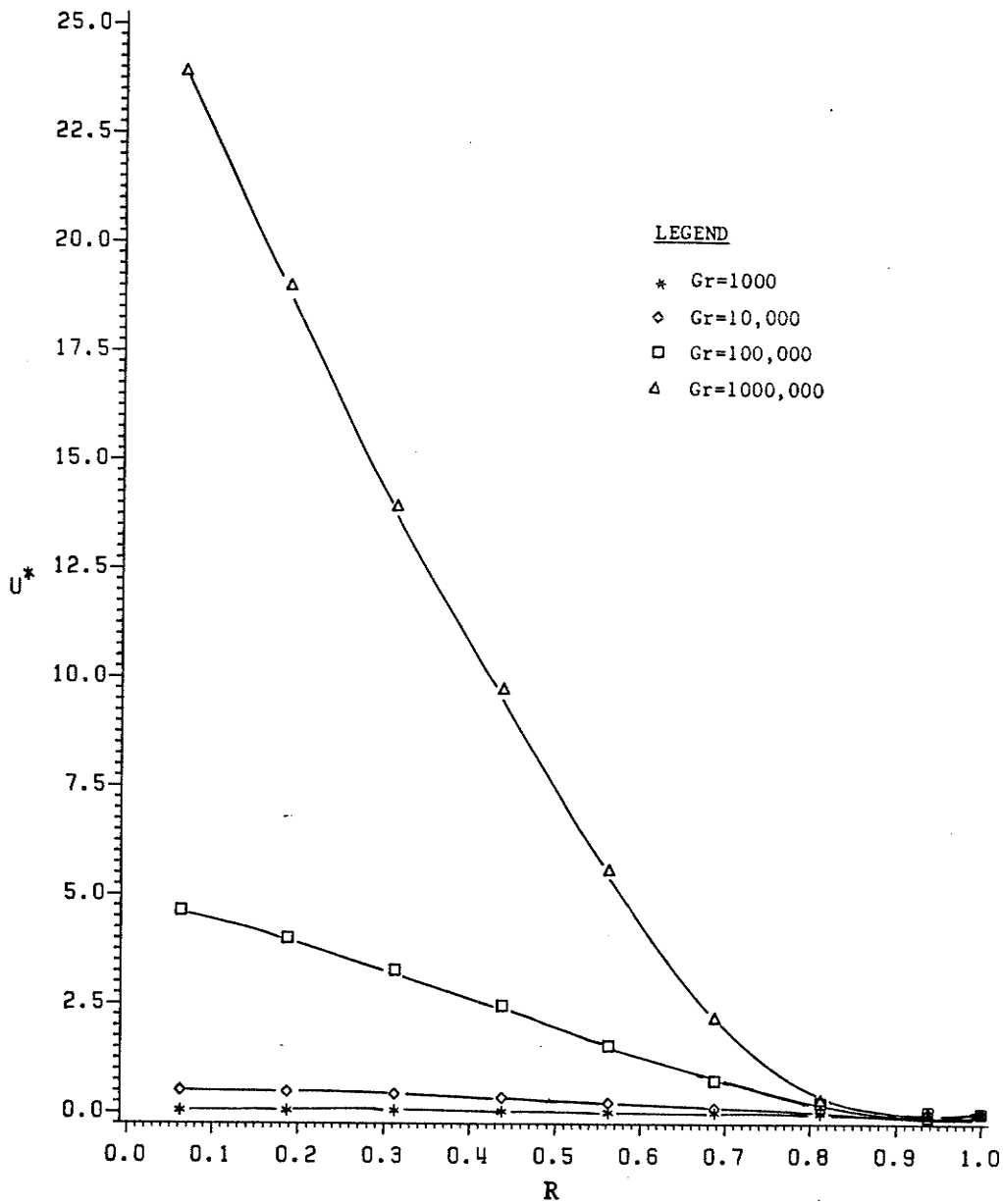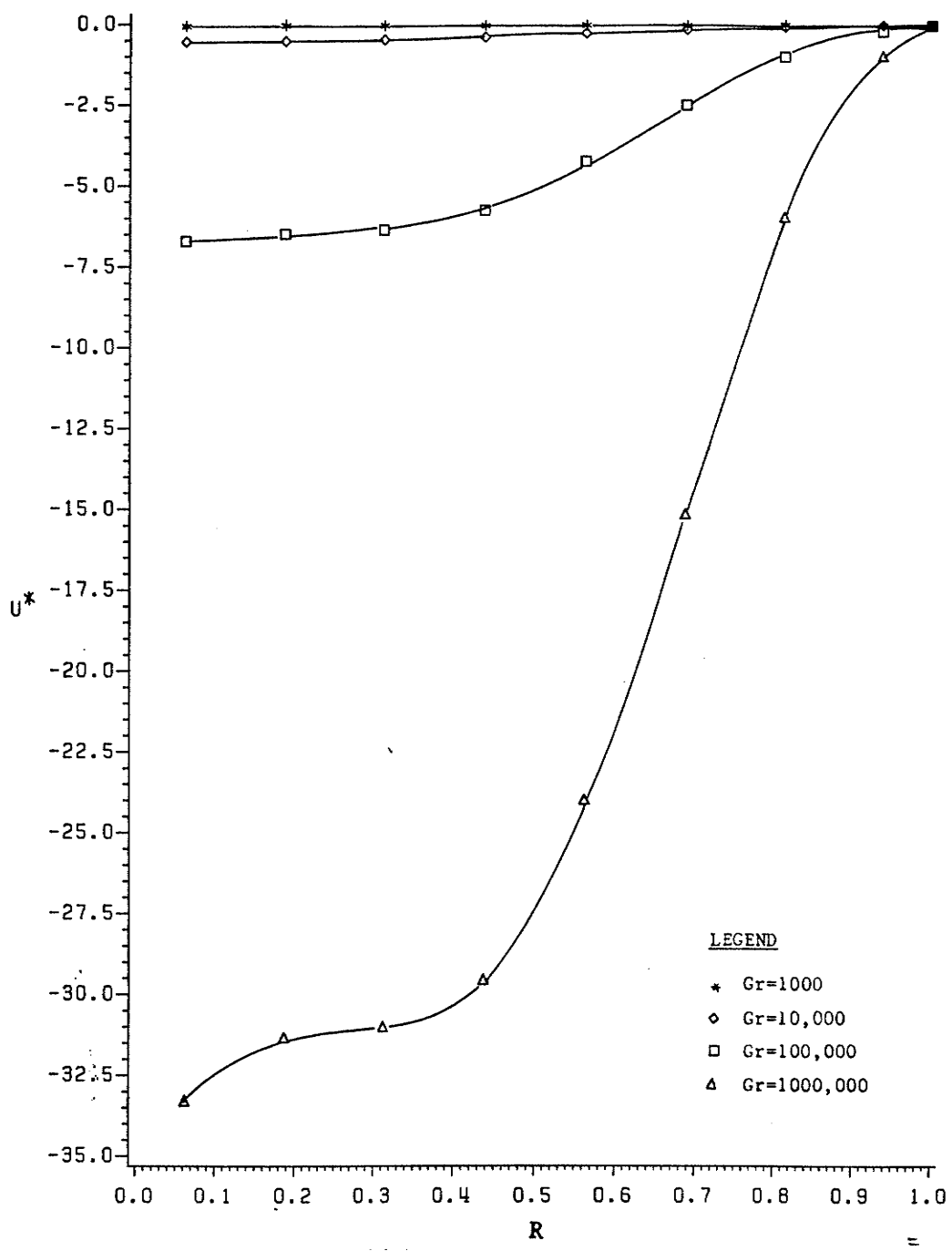
Fig. 5.15 Radial Variation of Radial Velocity (ϕ=12.85$^\bullet$, H=0.75)

Fig. 5.16 Radial Variation of Radial Velocity (ϕ=167.15$^{\bullet}$, H=0.75)

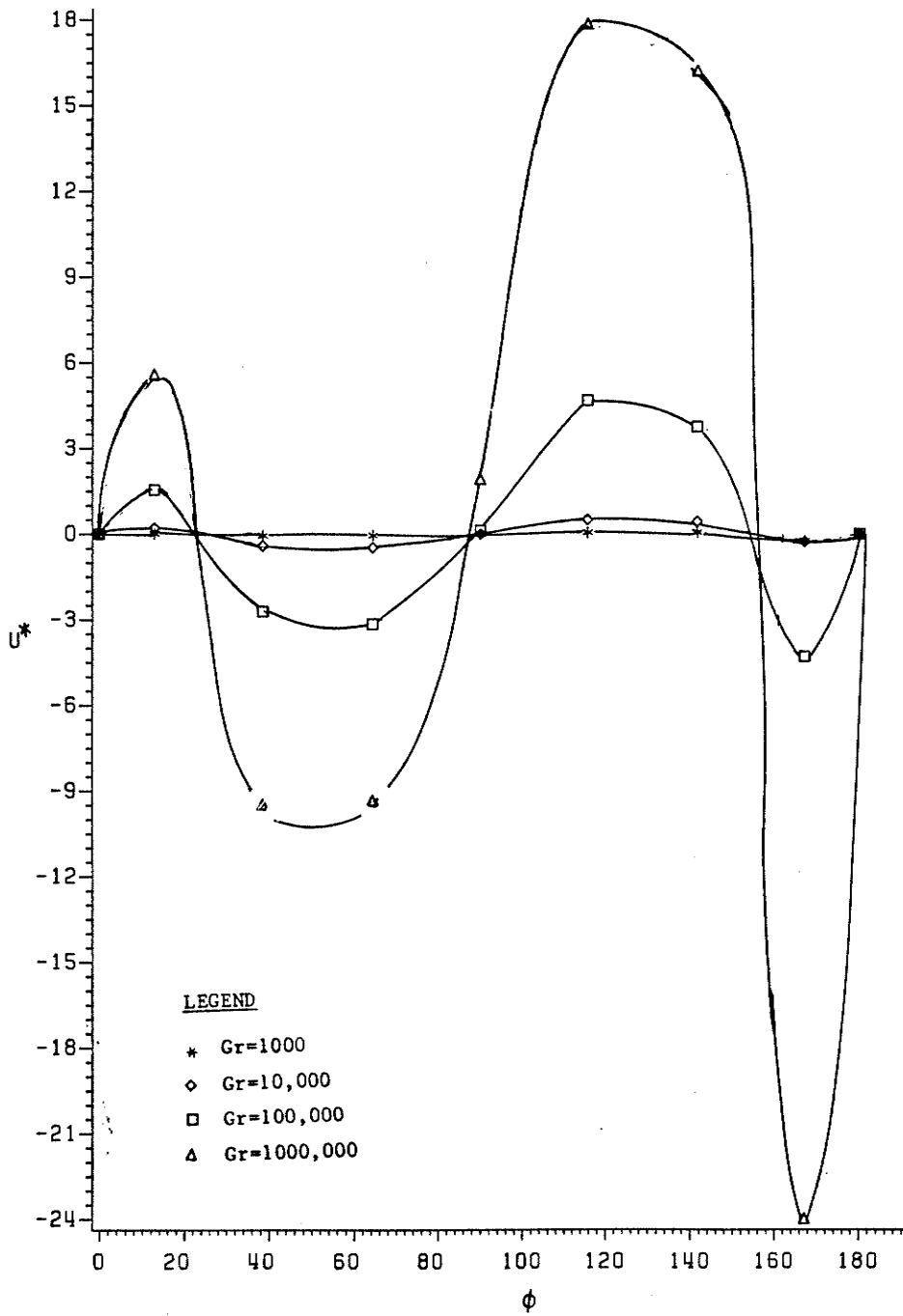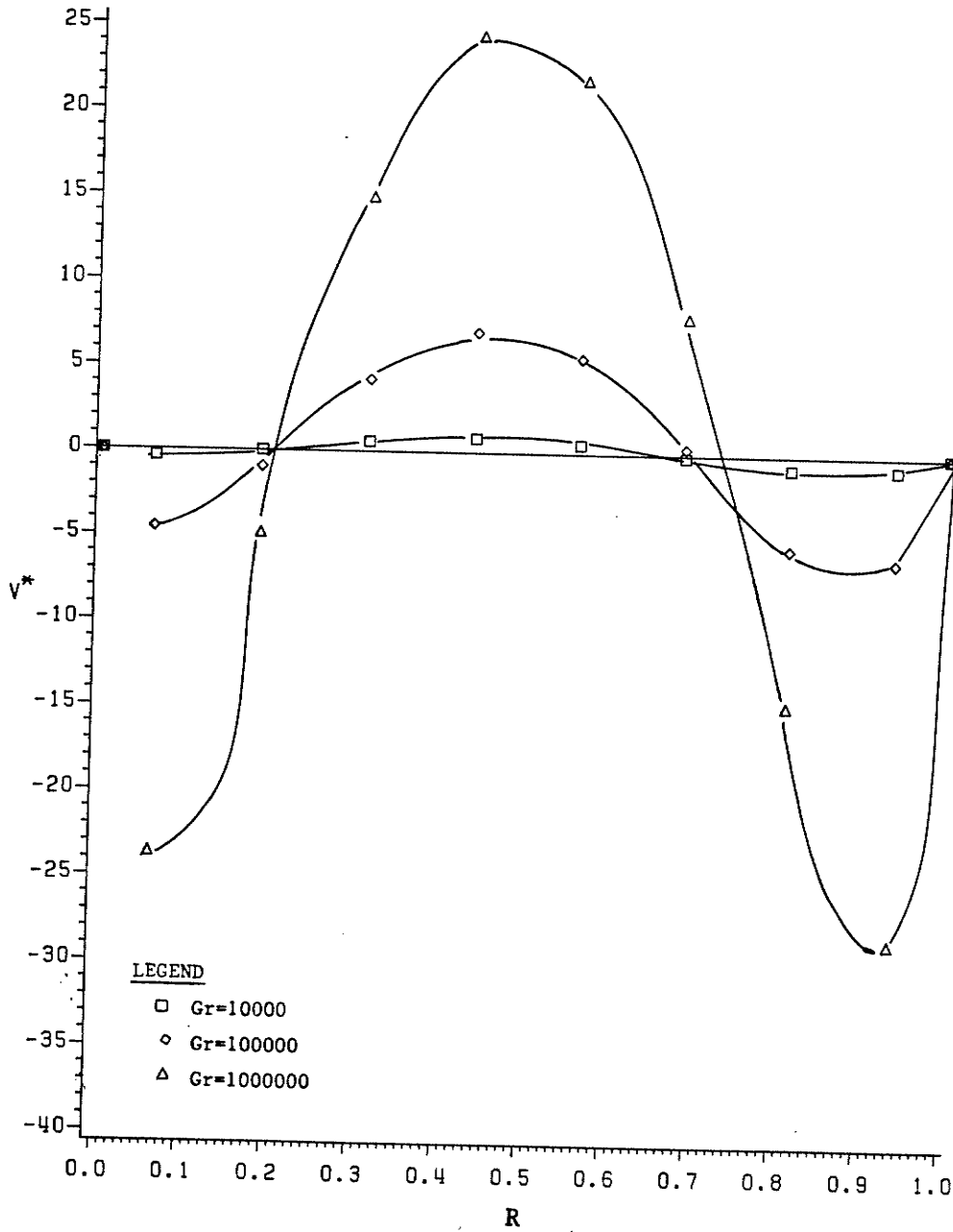Fig. 5.17 Angular Variation of Radial Velocity (R=0.5625, H=0.75)

Fig. 5.18 Radial Variation of Angular Velocity ($\phi=90°$, H=0.75)

of the tube is a heated surface.   In figure 5.15 which shows the

variation of U^* along the $\phi=12.85°$ line, fluid motion is upwards

for all values of Gr.   Values of U^* for upto Gr=10^4 are very

small. Between Gr=10^5 and 10^6, a sharp difference in the magni-

tudes of U^* is noticeable, which implies that, when fins are very

long, significant free convection effects start at very high

heating loads. This fact is also observed in figure 5.16. In both

the figures 5.15 and 5.16, an upward motion near the vertical

center plane is observed. A close examination of figures 5.17 and

5.18 suggests the formation of at least two distinct loops. Fluid

is moving up in the immediate vicinity of the vertical center

plane and the circular wall.   It is coming down in between these

two extremes. Since this behaviour is true for all values of Gr,

it can be said that the pattern of secondary flow is determined

by the tube's geometry. From figure 5.17,   location of coldest

fluid region can be predicted. In the bottom part of the tube, it

is bounded by $\phi=110°$ and $130°$ lines. An interesting observation

which may elucidate the effectiveness of the bottom fin as a heat

transfer surface, is made in figure 5.18. At Gr=10^6 and along the

horizontal center line of the tube, the magnitude of upward flow

near the center of the tube is almost equal to that at the tube's

circular wall. This suggests that   fin surface has appreciable

contribution to the rate of heat transfer. Another important ob-

servation from figures 5.15 and 5.18 can be made. Magnitudes of

secondary velocities are relatively smaller than the H=0.5 case.
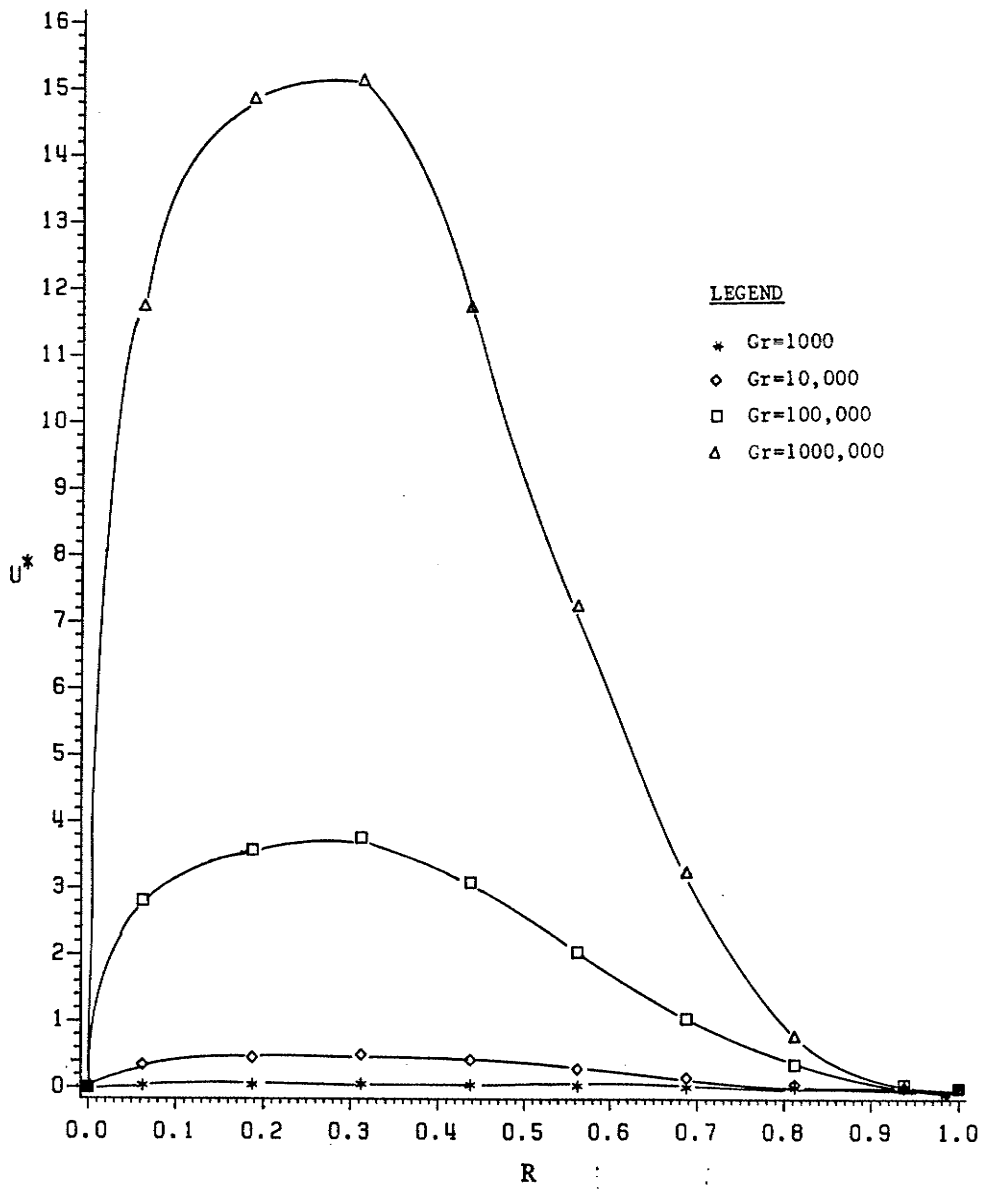
Effect of long fins is to suppress the secondary flow.

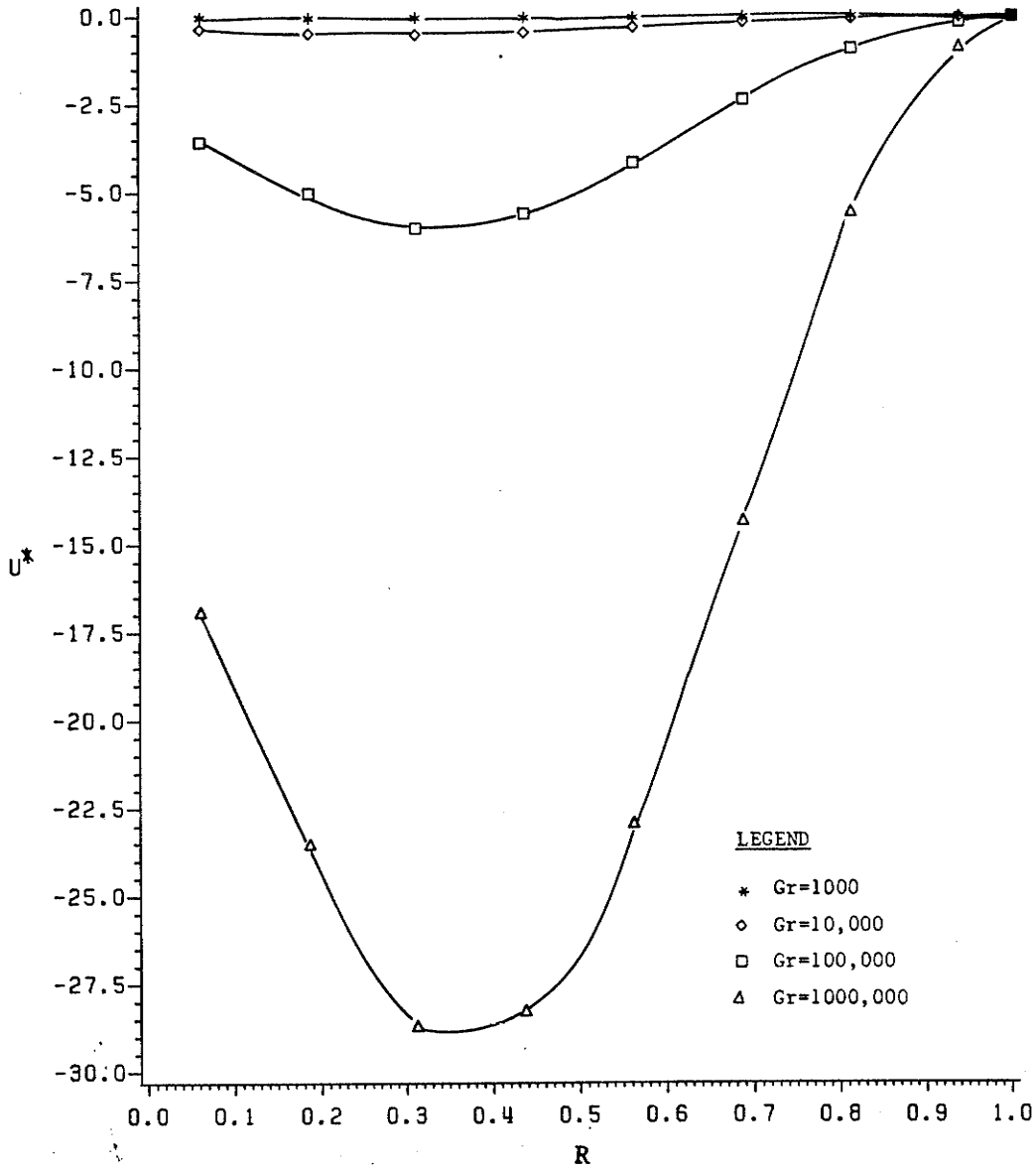Fig. 5.19 Radial Variation of Radial Velocity ($\phi=12.85^{\circ}$, H=1.00)

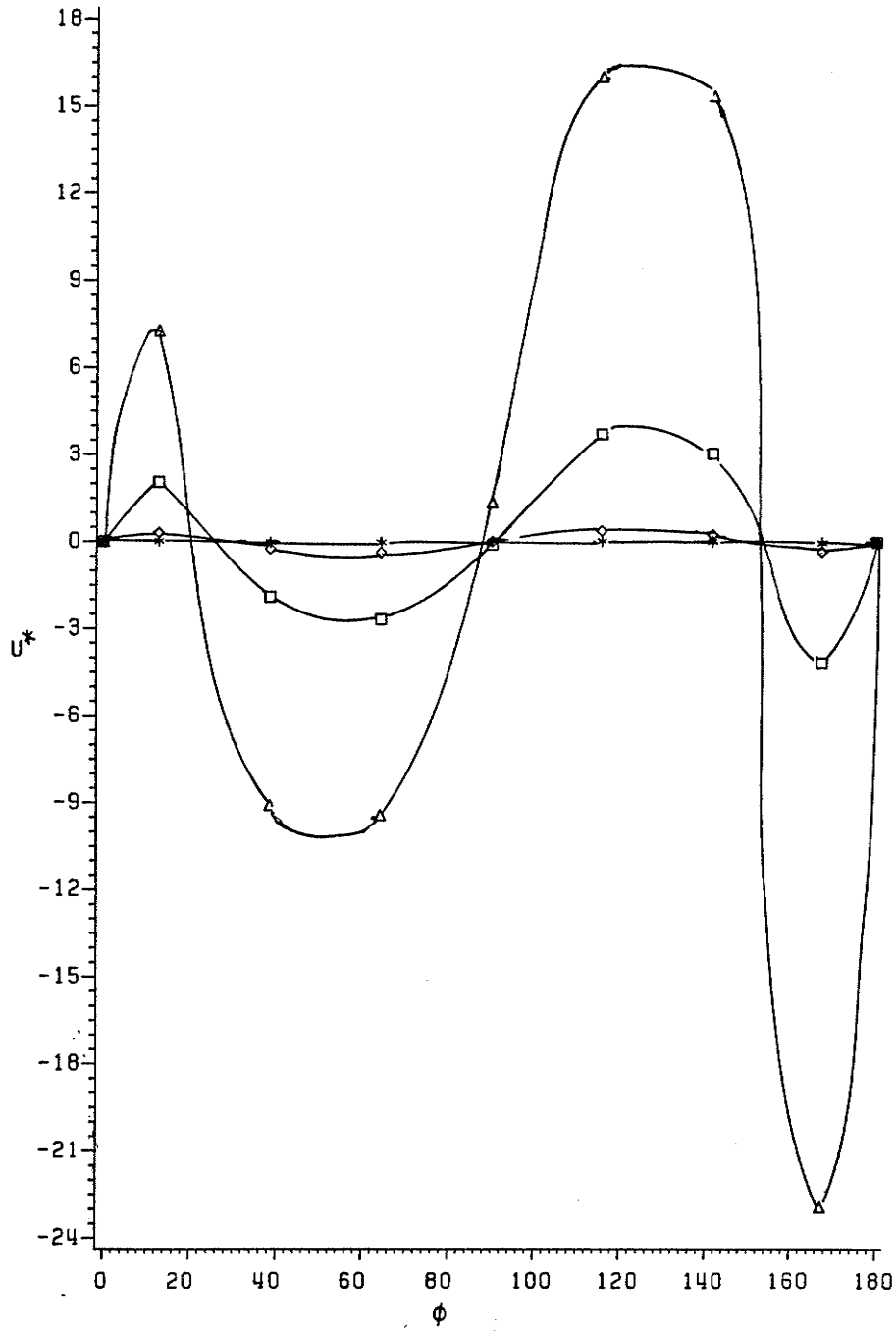Fig. 5.20 Radial Variation of Radial Velocity (ϕ=167.15$^{\theta}$, H=1.00)

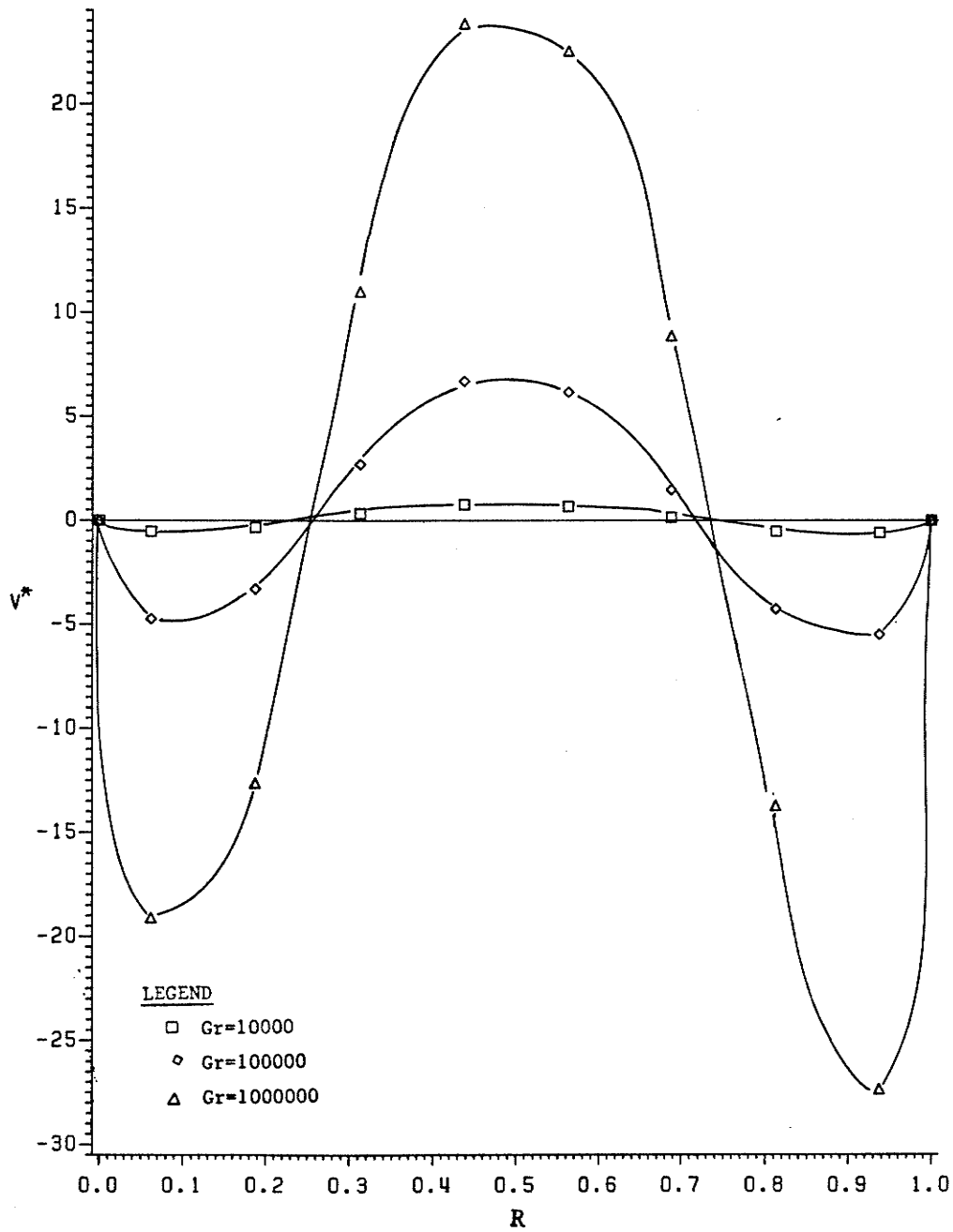Fig. 5.21 Angular Variation of Radial Velocity (R=0.5625, H=1.00)

Fig. 5.22 Radial Variation of Angular Velocity ($\phi=90^{\circ}$, H=1.00)

The case of fully finned tube (H=1.0) which is in fact a semicircular tube geometry is presented in figures 5.19 to 5.22. Now, since the whole vertical centerline of the tube is a solid heated surface, values of velocities are zero there. Looking at the radial variation of U^* along ϕ=12.85° line in figure 5.19, the values are seen to increase from zero at the center towards the increasing radius. For all values of Gr, U^* achieve a positive maximum in the interval of R=0.2 to 0.3, and then slow down to zero at R=1. Flow is upwards for all values of Gr however, a significant difference in the magnitudes of U^* at Gr=10⁶ and the rest demonstrates that, for longer fins, free convection effects are felt at very high heating loads. In figure 5.21, where angular variation of U^* is plotted around the R=0.5625 radial line, a flow pattern similar to the case of H=0.75 is observed. Maximum positive values of U^* are seen to be in the bottom part of the tube and are bounded by ϕ=90° and ϕ=150° lines. The area under the curve where maximum positive values of U^* are observed, is smaller than the corresponding area for the H=0.75 case. This is an indication that the region where the coldest fluid exists is smaller and localized. Such a situation is expected. The flow domain is now totally bounded by a hot surface, and a double loop pattern discussed earlier has to be more prominent. Hence colder fluid confines to a smaller region. Figure 5.22 presents the radial variation of V^* along the horizontal center plane of the tube. V^* has a value of zero at the center. Fluid is moving up near the center and the circular wall, and, is coming down in the

middle region. In comparison with figure 5.18 (The case of H=0.75), figure 5.22 indicates a decrease in the values of V^* near the center. In general, magnitudes of secondary velocities are lower than the H=0.75 case.

5.1.2 Axial Velocity

Two graphs for each tube geometry are plotted to describe the picture of primary flow. In the first graph, radial variation of axial velocity along the horizontal center plane of the tube has been plotted, while the other graph shows the angular variation of axial velocity around the R=0.5625 line. In order to illustrate the effects of free convection on forced convection, all graphs include the case of pure forced convection (Gr=0) as well.

Figures 5.23 and 5.24 correspond to smooth tubes. In figure 5.23, variation of W^* along the horizontal center plane of the tube is shown. For the case of pure forced convection, a parabolic velocity profile is observed. A similar profile is observed at Gr=10⁴. Values of axial velocity are found to be maximum at the center which is in accordance with the pure forced convection theory. It can be said that upto a Grashof number of 10⁴, effects of free convection are small. At Gr=10⁵ and 10⁶, two changes are noticeable. First, the magnitude of axial velocity has decreased along the horizontal center plane, and second its maximum value is no more at the center of the tube. Recalling figures 5.1 to 5.4, it was infered that for smooth tubes, the region where coldest fluid would exist is along the lower half of the vertical
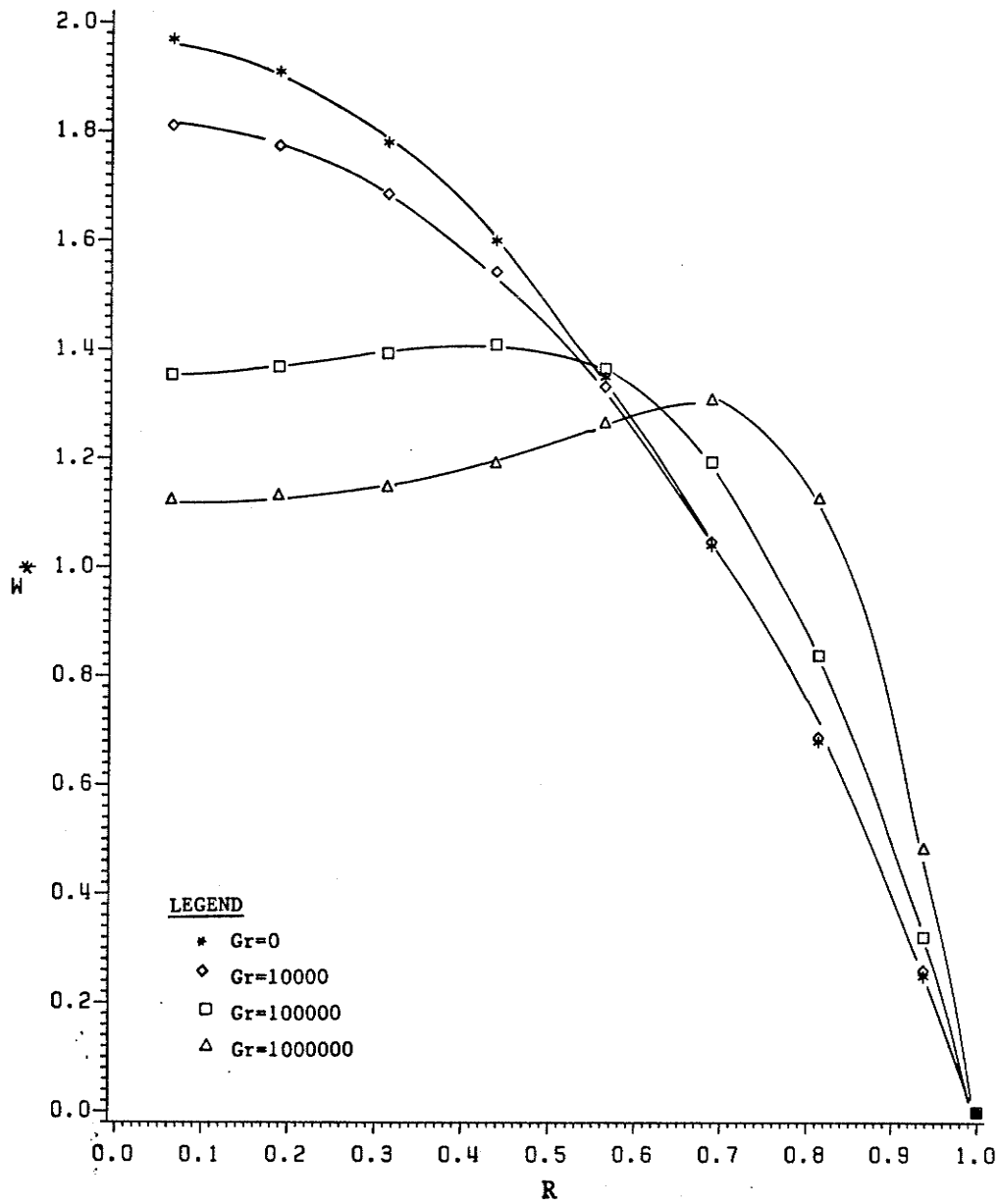
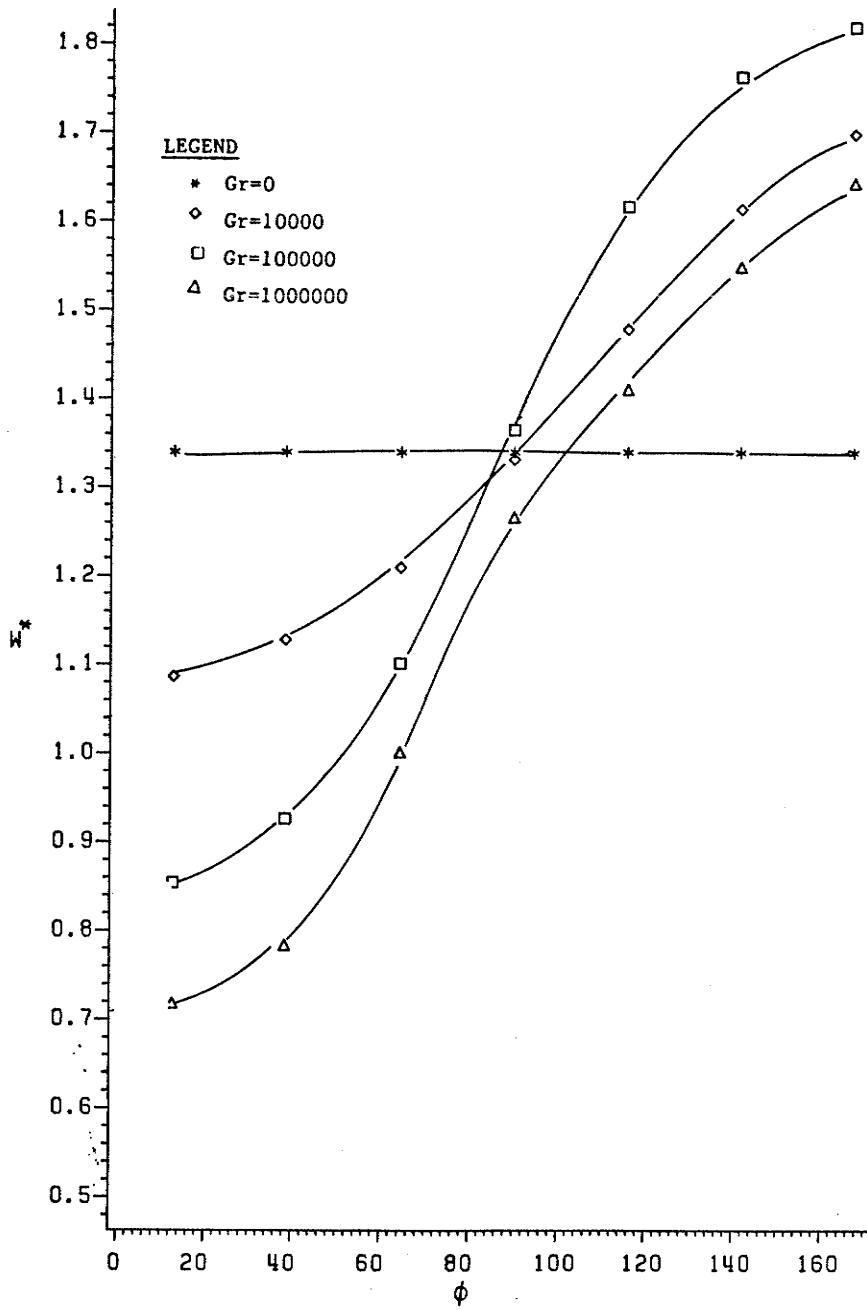Fig. 5.23 Radial Variation of Axial Velocity ($\phi=90^\circ$, H=0.00)

Fig. 5.24 Angular Variation of Axial Velocity (R=0.5625, H=0.00)

center plane. A change of profile in figure 5.23 and a close examination of figure 5.24 verify this fact. In figure 5.24, for any non-zero value of Gr, maximum values of W^* are along the lower half of the vertical center plane. Moreover, its minimum value occurs at the upper half. A downward shift in maxima can only be explained on the basis of a downward shift in the coldest fluid region. Looking at the axial velocity gradients at the wall in figure 5.23, increased heating loads have an effect to increase the wall velocity gradients. It can therefore be said that, free convection effects increase the surface friction experienced by the fluid.

Case of short fins (H=0.25) is shown in figures 5.25 and 5.26. Figure 5.25 shows almost similar velocity profiles as in figure 5.23. Axial velocity gradients at the wall are now slightly steeper, indicating that introduction of two short fins has increased the surface friction. Figure 5.26 where angular variations of W^* are plotted around the R=0.5625 line is more revealing. At Gr=0, W^* is dependent on ϕ, which was not the case for smooth tubes. Another feature is the shift of maximum values of W^* slightly away from the lower half of the vertical center plane. They now occur at angles which are less than 180°. This behaviour has already been predicted during the secondary flow analysis, and can be explained in terms of the location of the cold fluid. Cold fluid is accumulated in the bottom part of the tube but due to the presence of fins, it is slightly away from the vertical center plane. Being heavier, this fluid has larger local axial velocities.
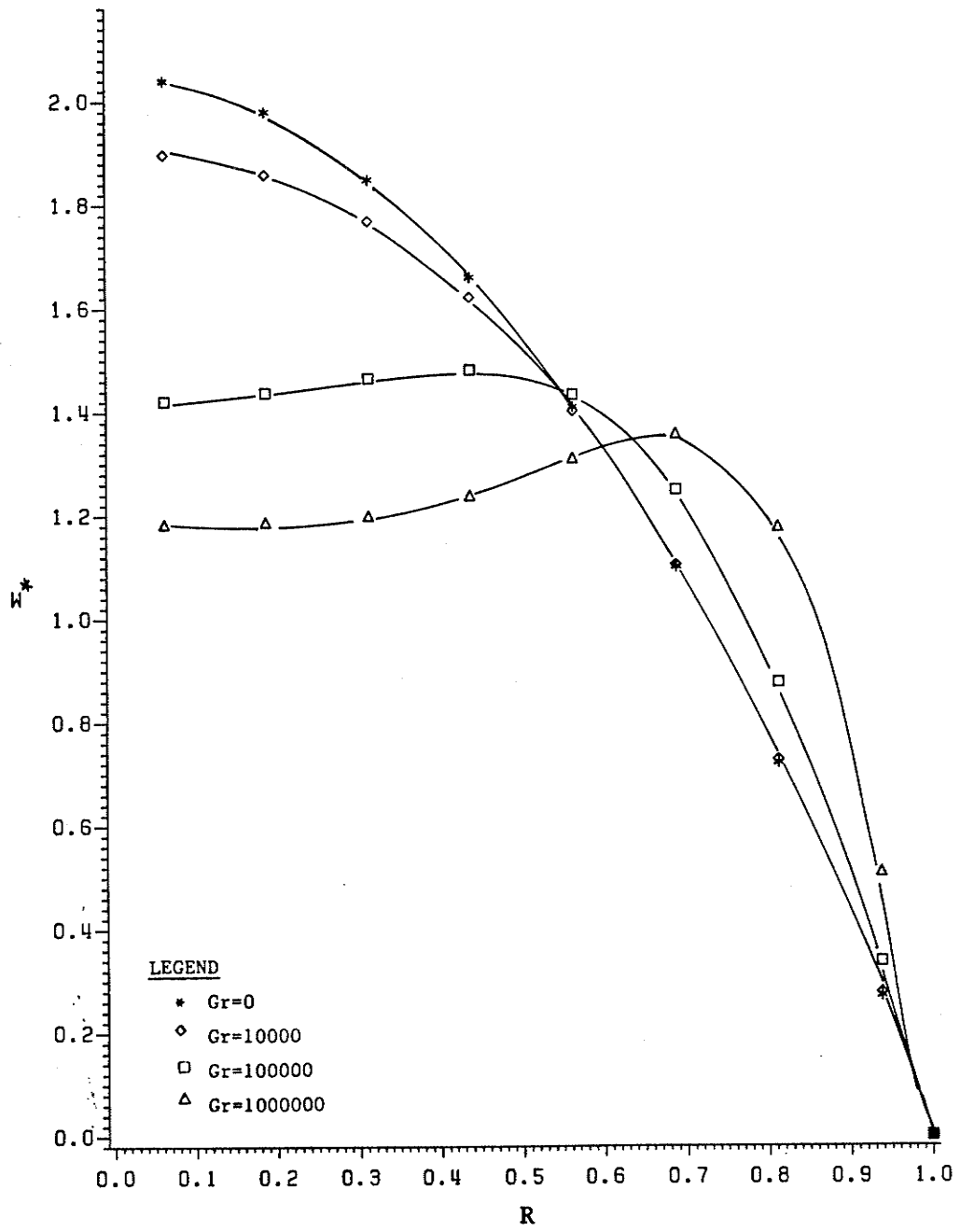
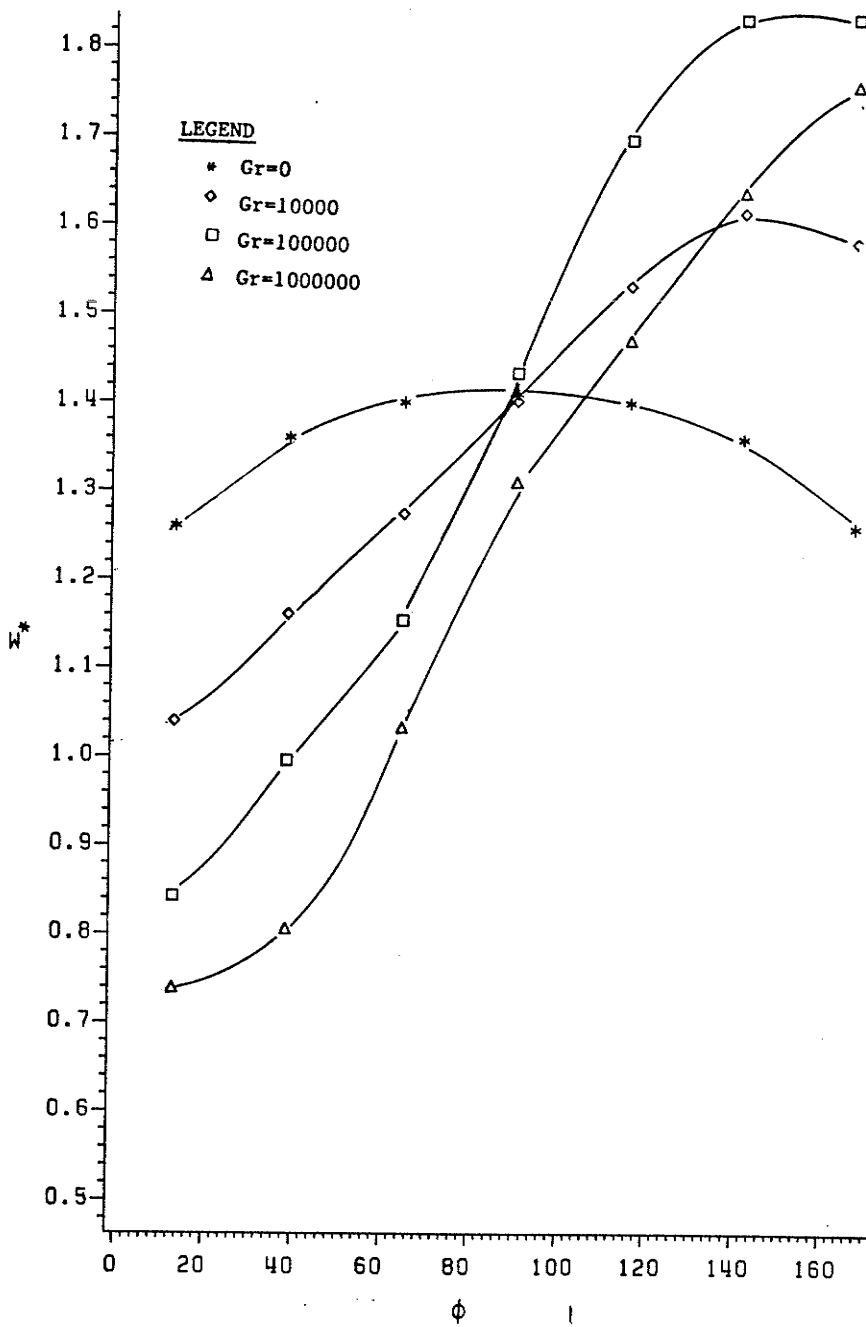Fig. 5.25 Radial Variation of Axial Velocity ($\phi=90^\bullet$, $H=0.25$)
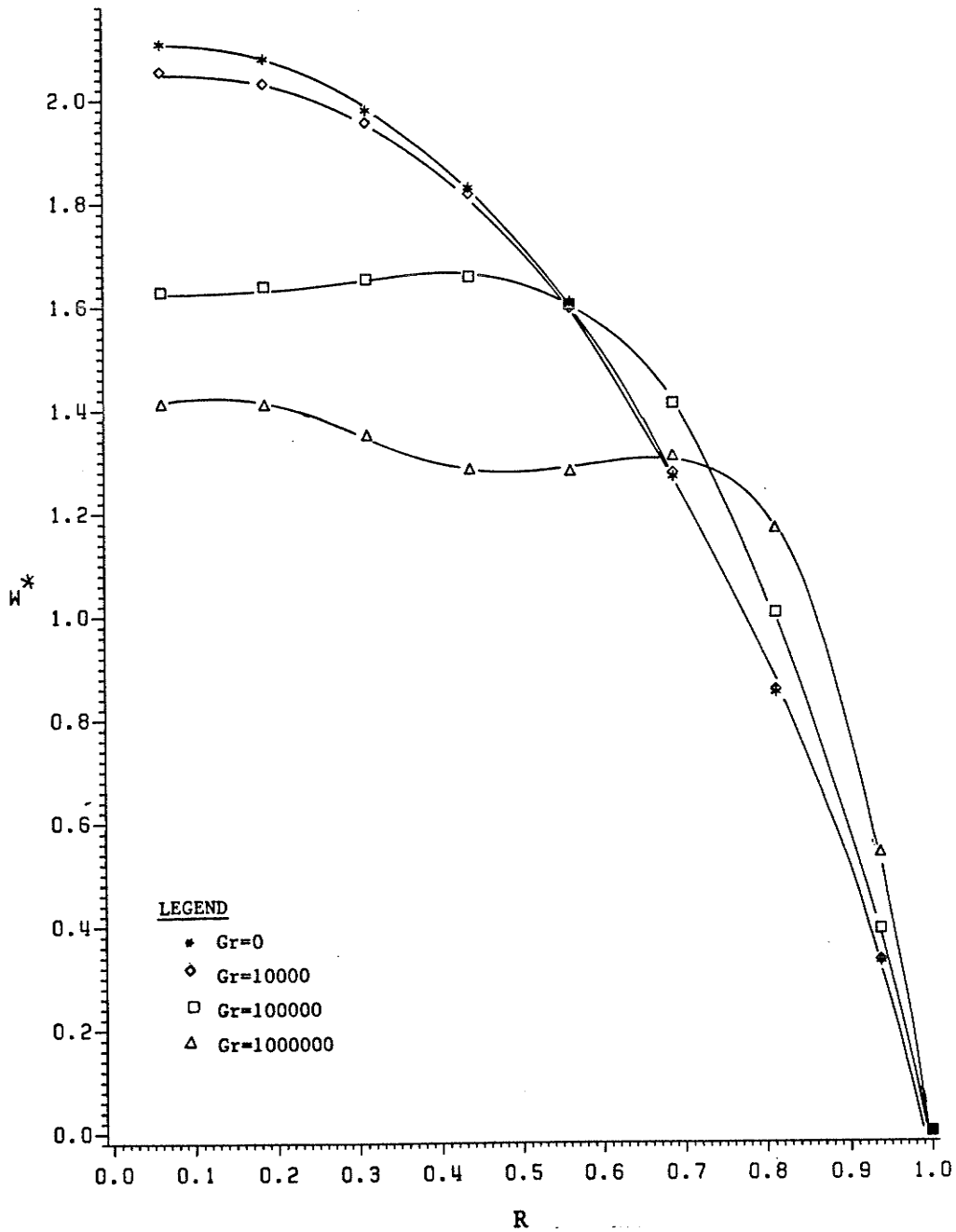
Fig. 5.26 Angular Variation of Axial Velocity (R=0.5625, H=0.25)

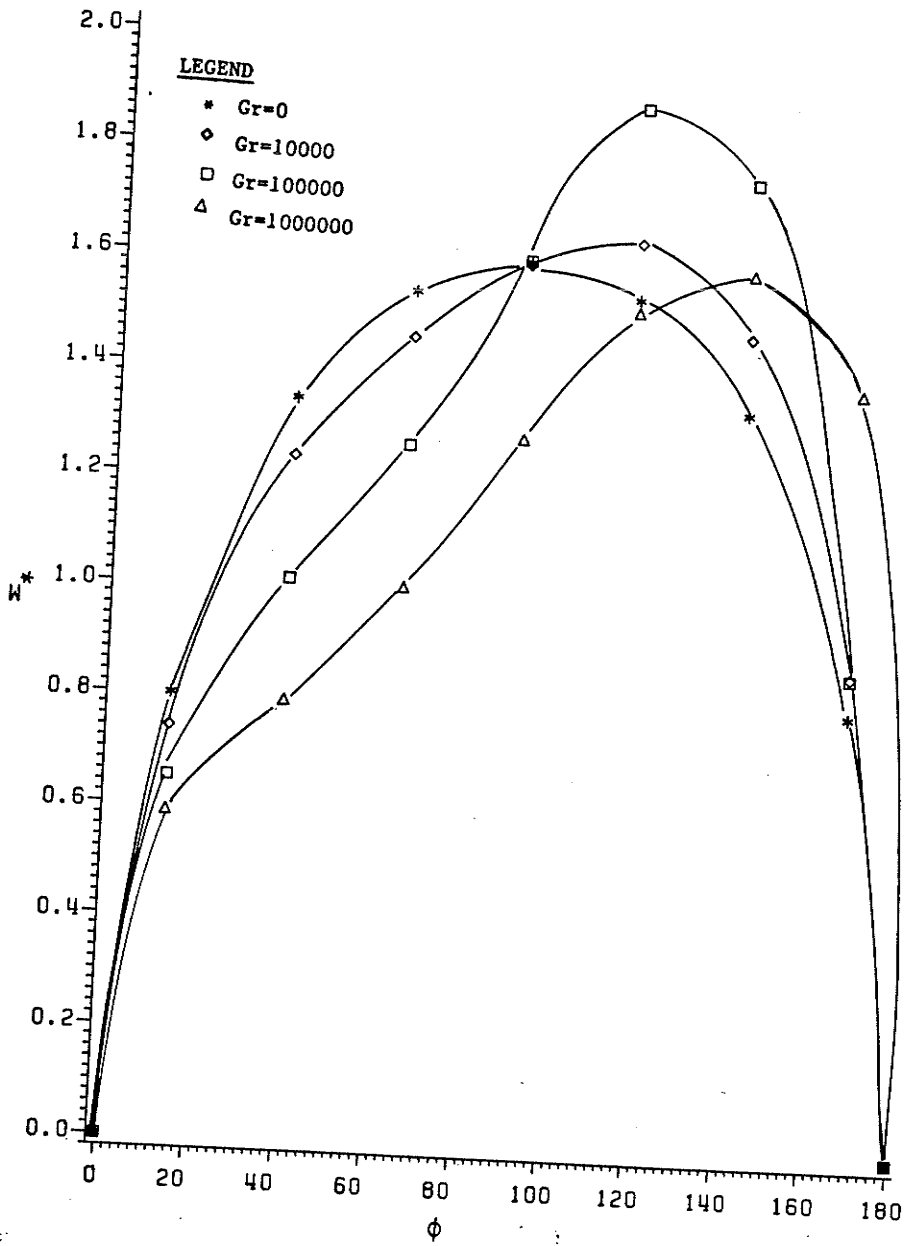Fig. 5.27 Radial Variation of Axial Velocity ($\phi=90°$, H=0.50)

Fig. 5.28 Angular Variation of Axial Velocity (R=0.5625, H=0.50)

Figures 5.27 and 5.28 are plotted for H=0.5. In general, figure 5.27 shows higher axial velocity gradients at the wall than the previous two cases. A rightward shift in the maximum values of W^* is observed as the value of Gr is increased, which can be attributed to the secondary flow pattern observed in the previous section. For this value of H, the difference between the W^* profiles for Gr=0 and Gr=10⁴ is small. It indicates that as fins are getting longer, free convection effects are felt at higher heating loads. An explanation of this phenomenon can be given in terms of the nature of secondary flow. As was observed, the effect of long fins was to decrease the secondary velocities until very high heating loads were applied. The single loop pattern of the secondary flow was seen to be distorted, and formation of two or more loops was concluded. That picture is also reflected here. Figure 5.28 illustrate two major changes when compared with figures 5.24 and 5.26. First, for all non-zero values of Gr, the location of maximum value of axial velocity shifts from the horizontal plane. This is explained on the basis of colder fluid. More important observation however is the magnitude of axial velocity gradients at the top and the bottom fins. At the top fin (ϕ=0°), steepest gradient is observed for the pure forced convection case. As the value of Gr is increased, gradients become less and less steep. At the bottom fin (ϕ=180°) a reversed trend is observed. From this observation, it can be said that as the free convection effects become prominent, the top fin offers less resistance to the axial flow, whereas, the bottom fin has an inverse effect.
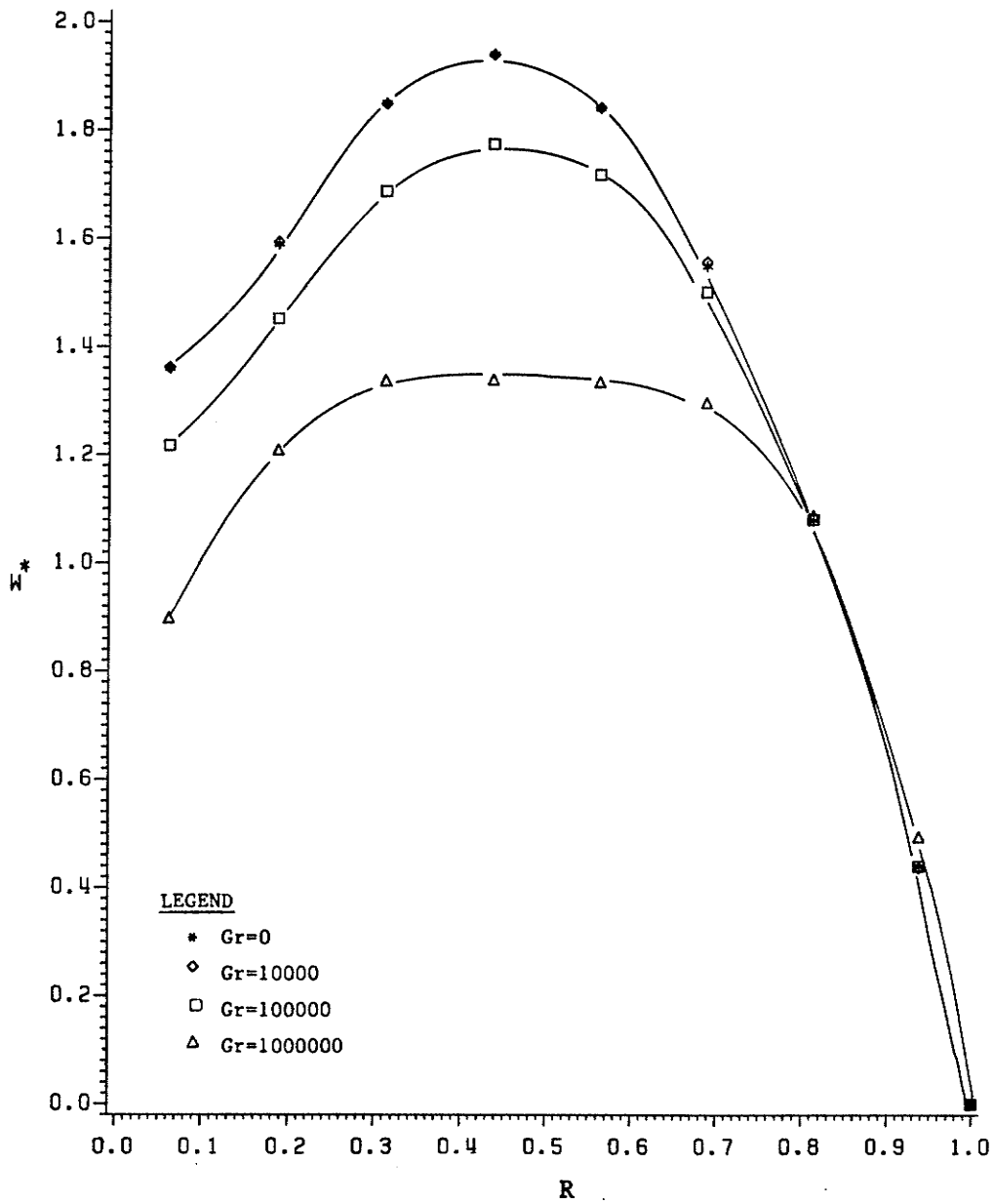
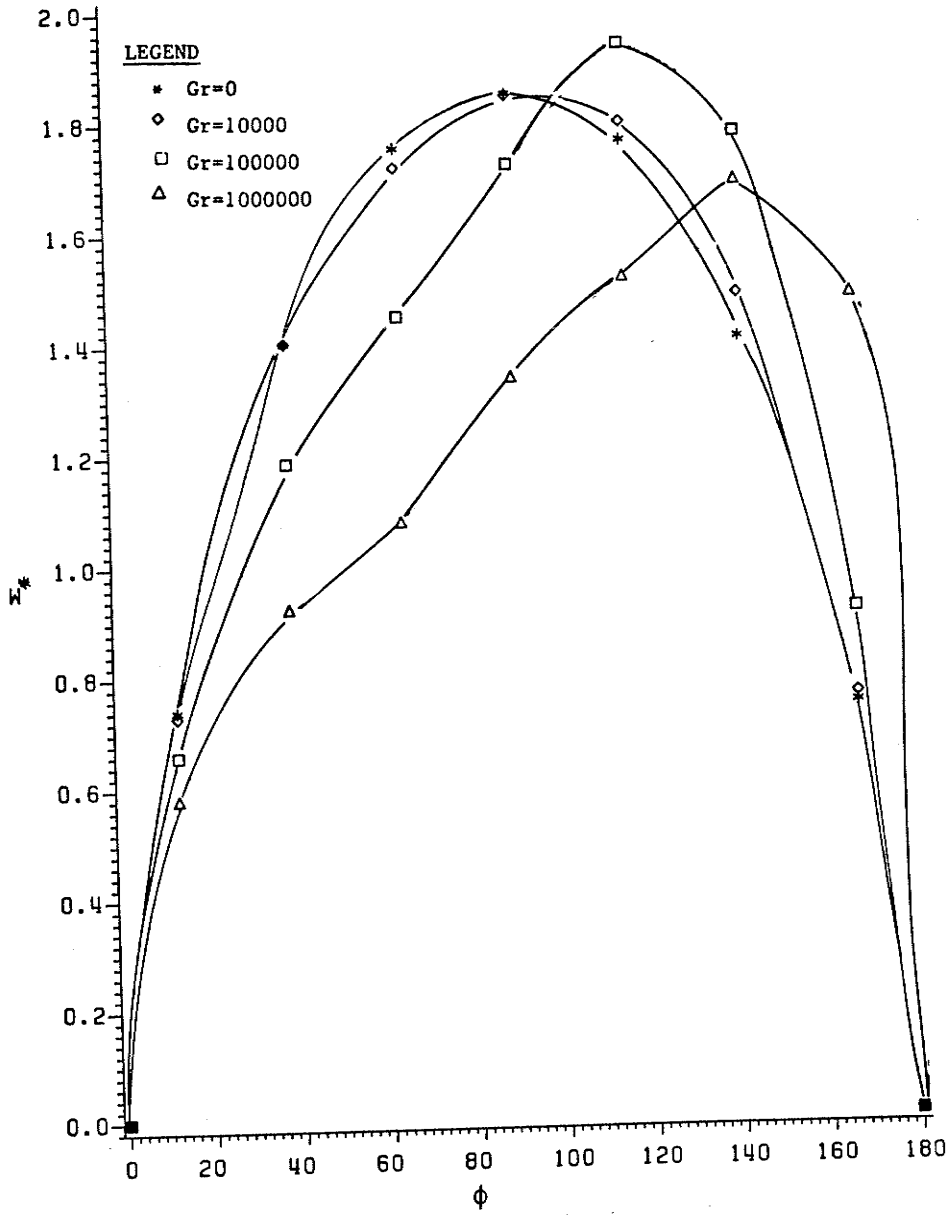Fig. 5.29 Radial Variation of Axial Velocity ($\phi=90^{\circ}$, H=0.75)

Fig. 5.30 Angular Variation of Axial Velocity (R=0.5625, H=0.75)

Axial velocity variations for the H=0.75 tube geometry are plotted in figures 5.29 and 5.30. In figure 5.29, two important features pertaining to Gr=0 and Gr=10⁴ are observed. First, the two lines almost overlap each other, confirming the notion that for upto Gr=10⁴, effects of free convection are almost negligible. This was also observed when secondary velocities were analyzed. Second, it can be seen that maximum values of W^* have shifted from R=0 (in previous cases) to an R of about 0.45. The second observation can be explained by the presence of very long fins. Now 75% of the vertical center plane is a solid, heated surface. High values of W^* for the case of Gr=10⁶ are distributed over a large region, ranging from R=0.3 to R=0.6. As observed previously, secondary flow was downwards with considerable velocities in this region, hence, it is obvious that colder fluid exists underneath this radial interval, and is reflected by the axial velocity profile. For upto Gr=10⁵, axial velocity gradients at the wall are almost identical. This implies that the influence of secondary flow on forced convection is significant only at very high heating loads. Figure 5.30 where variation of W^* is plotted around R=0.5625, supports this conclusion. From axial velocity gradients, much larger surface friction is observed at the bottom fin for Gr=10⁶. Maximum values of W^* exist at ϕ=90° when Gr=0. At higher heating loads however, there is a gradual downward shift.

The case of full fin (H=1.0) is shown in figures 5.31 and 5.32. Tube's vertical center plane is now a solid surface. Fig-
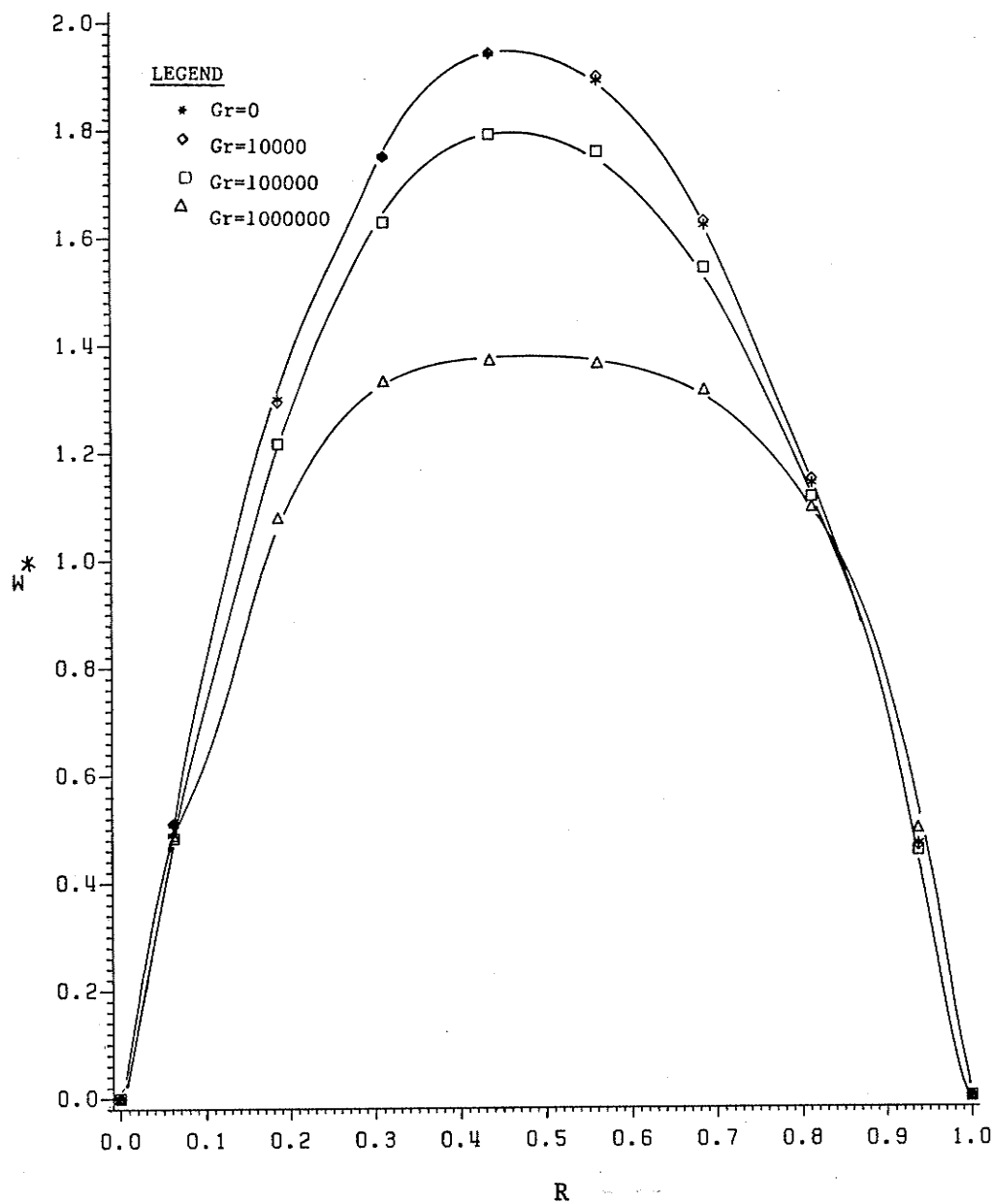
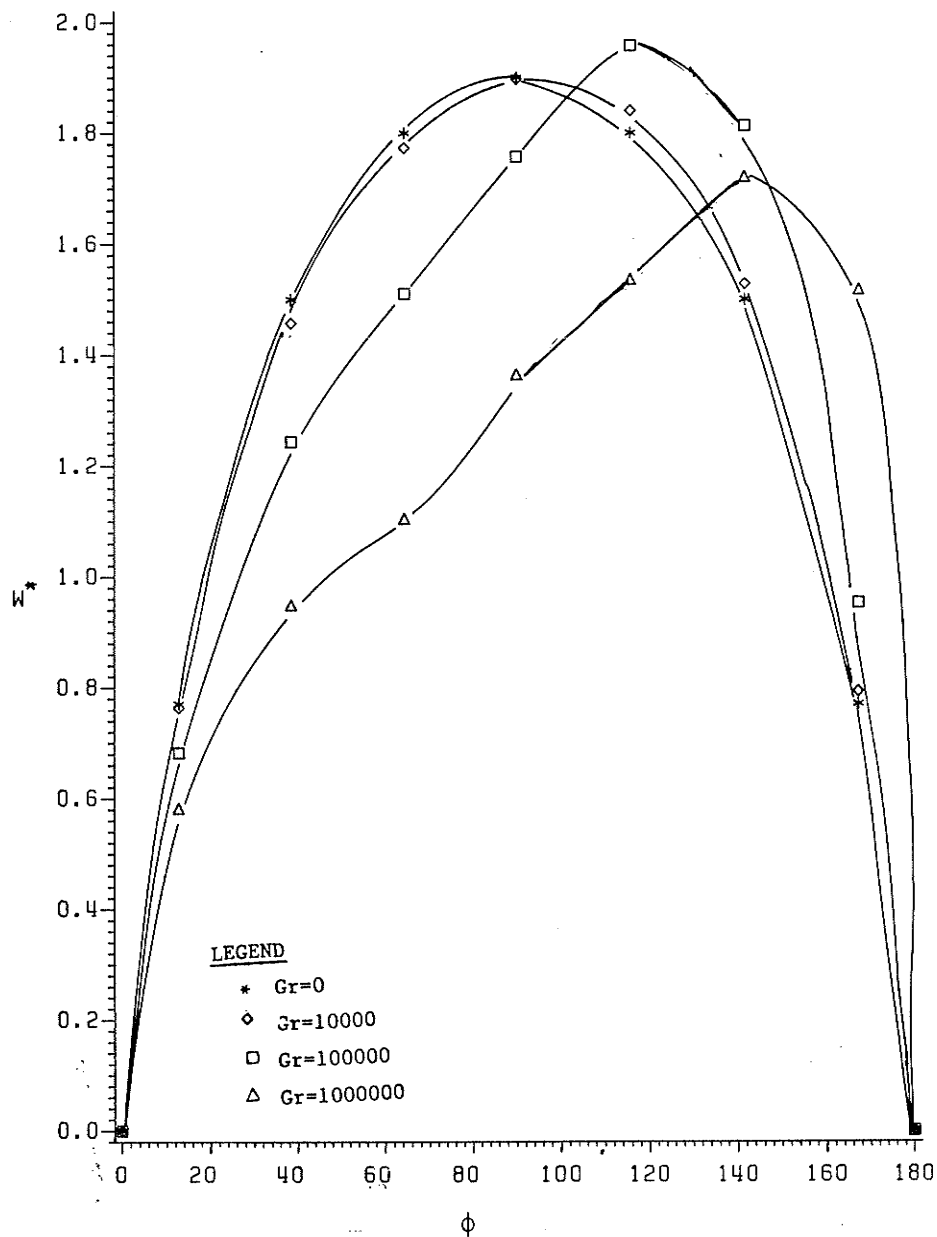Fig. 5.31 Radial Variation of Axial Velocity ($\phi=90°$, H=1.00)

Fig. 5.32 Angular Variation of Axial Velocity (R=0.5625, H=1.00)

ure 5.31 shows the variation of W^* along the horizontal center plane of the tube. Starting from a value of zero at the center (R=0), axial velocity increases upto a maximum value at about R=0.45 and then decreases down to zero at the tube wall (R=1). Axial velocity gradients at the wall are almost identical upto Gr=10^5. It is concluded that free convection effects are observed well above this value of Gr. There is a slight difference in the values of these gradients even at Gr=10^6. Figure 5.32 clearly differentiates the surface friction experienced by the top and bottom fins. Much larger surface friction is observed at the bottom fin. Maximum values of W^* existing at the $\phi=90°$ line suggest that the location of coldest fluid shifts more from the horizontal center plane as Gr increases.

5.2   TEMPERATURE FIELD

Similar to the axial velocity, two figures for each tube geometry were plotted for the temperature distribution. The pure forced convection case (Gr=0) is included for comparative purposes.

Figures 5.33 and 5.34 illustrate the smooth tube case. In figure 5.33 where the radial variation of θ^* is plotted along the horizontal center plane of the tube, minimum values of θ^* for Gr=0 and 10^4 exist at the center. Central temperature is slightly higher for the latter case, implying that although the free convection effects at Gr=10^4 are small, fluid temperature is more uniform. For higher values of Gr, magnitudes of θ^* are higher
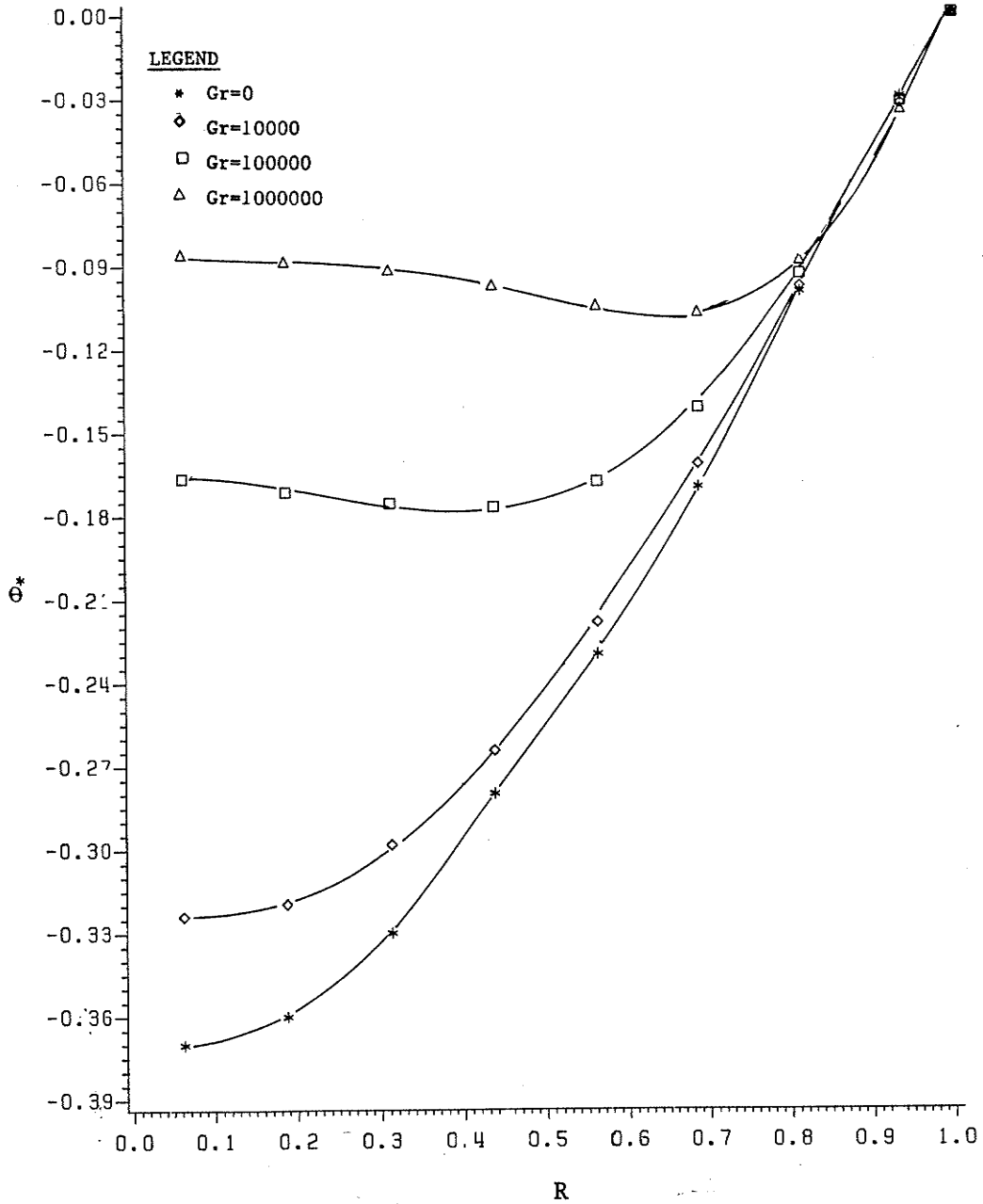
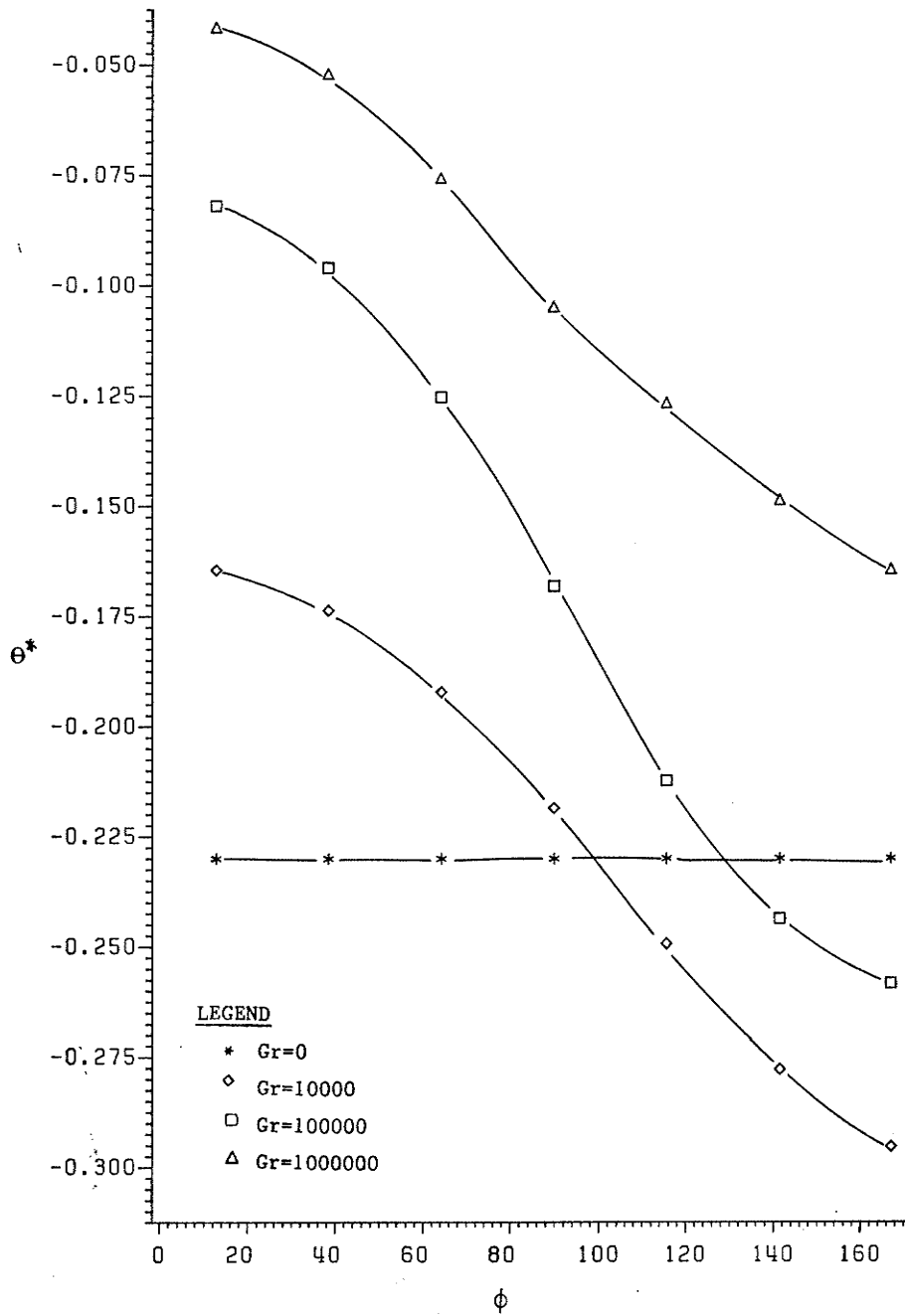Fig. 5.33 Radial Variation of Temperature ($\phi=90^{\circ}$, H=0.0)

Fig. 5.34 Angular Variation of Temperature (R=0.5625, H=0.0)

and therefore the convective heat transfer process is observed to have been enhanced. For Gr=10^5 and 10^6, the global minima with magnitudes greatly increased are seen to have shifted rightwards. Figure 5.34 which shows the angular variation of θ^* around R=0.5625, further illustrates these shifts. Location of coldest fluid which was at the center for Gr=0 case, has moved down along the lower half of the vertical center plane. Hot fluid however, has to be found at the upper half. This phenomenon was predicted when velocity fields were studied, and can be completely explained in terms of secondary flow patterns. An important observation is made when figures 5.23 and 5.33 are compared. Increasing values of Gr have created a magnitude difference in both the axial velocities and temperature. However, these relative differences are much larger for temperature than for axial velocities. This provides an indication that effects of free convection on the heat transfer process are expected to be significant.

The case of H=0.25 is represented by figures 5.35 and 5.36. Figure 5.35 is qualitatively similar to figure 5.33, a slight increase in the magnitudes of temperature is observed as Gr is increased. Temperature profiles for Gr=0 and Gr=10^4 are close to each other, implying that at Gr=10^4 the effects of free convection are small. As the value of Gr is increased, a significant increment in the temperature magnitudes is observed. From wall temperature gardient it is observed that as the value of Gr increases, local heat flux also increases. It indicates enhancement in the overall heat transfer. Figure 5.36 shows that at higher
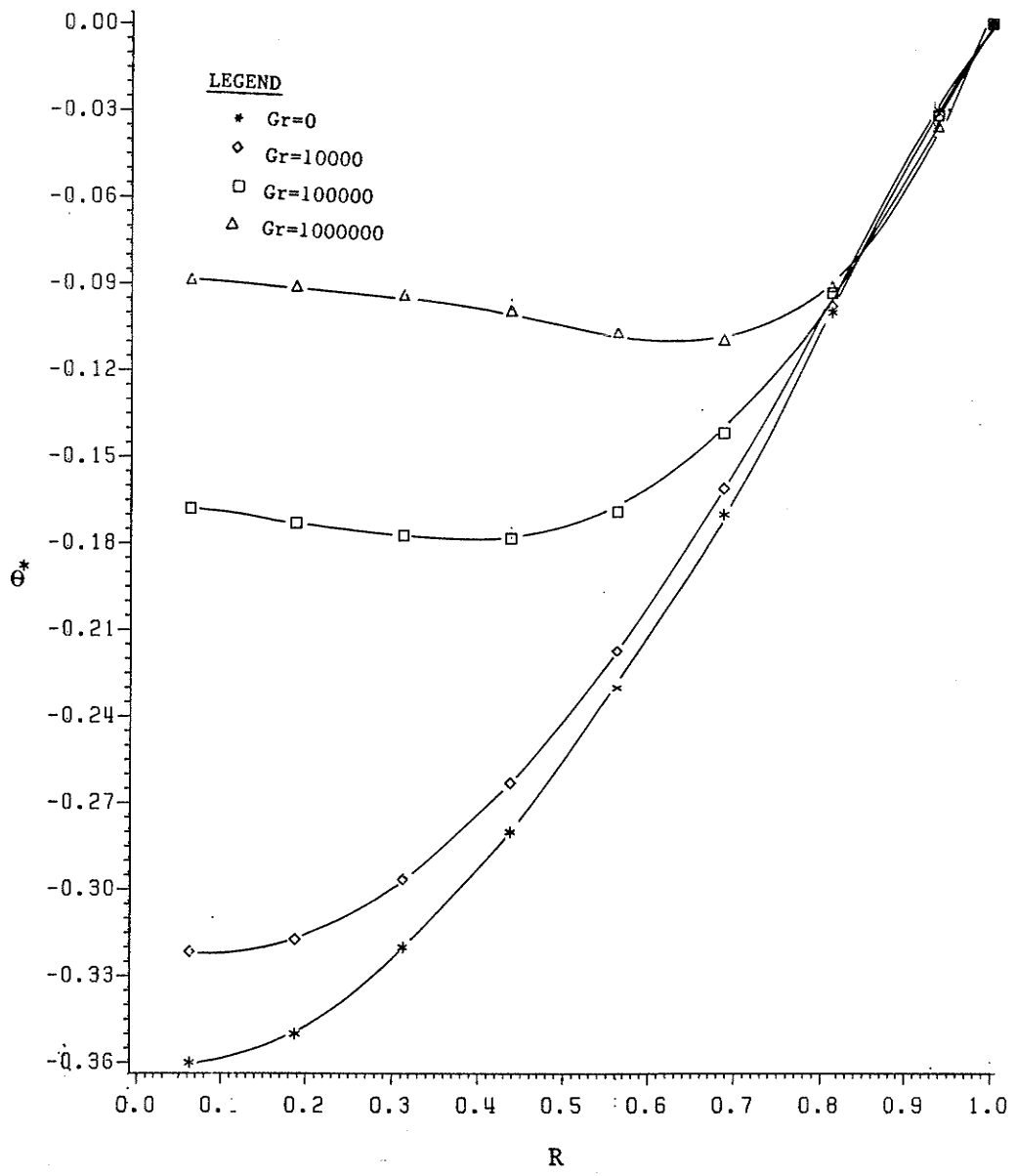
Fig. 5.35 Radial Variation of Temperature ($\phi=90^{\circ}$, H=0.25)
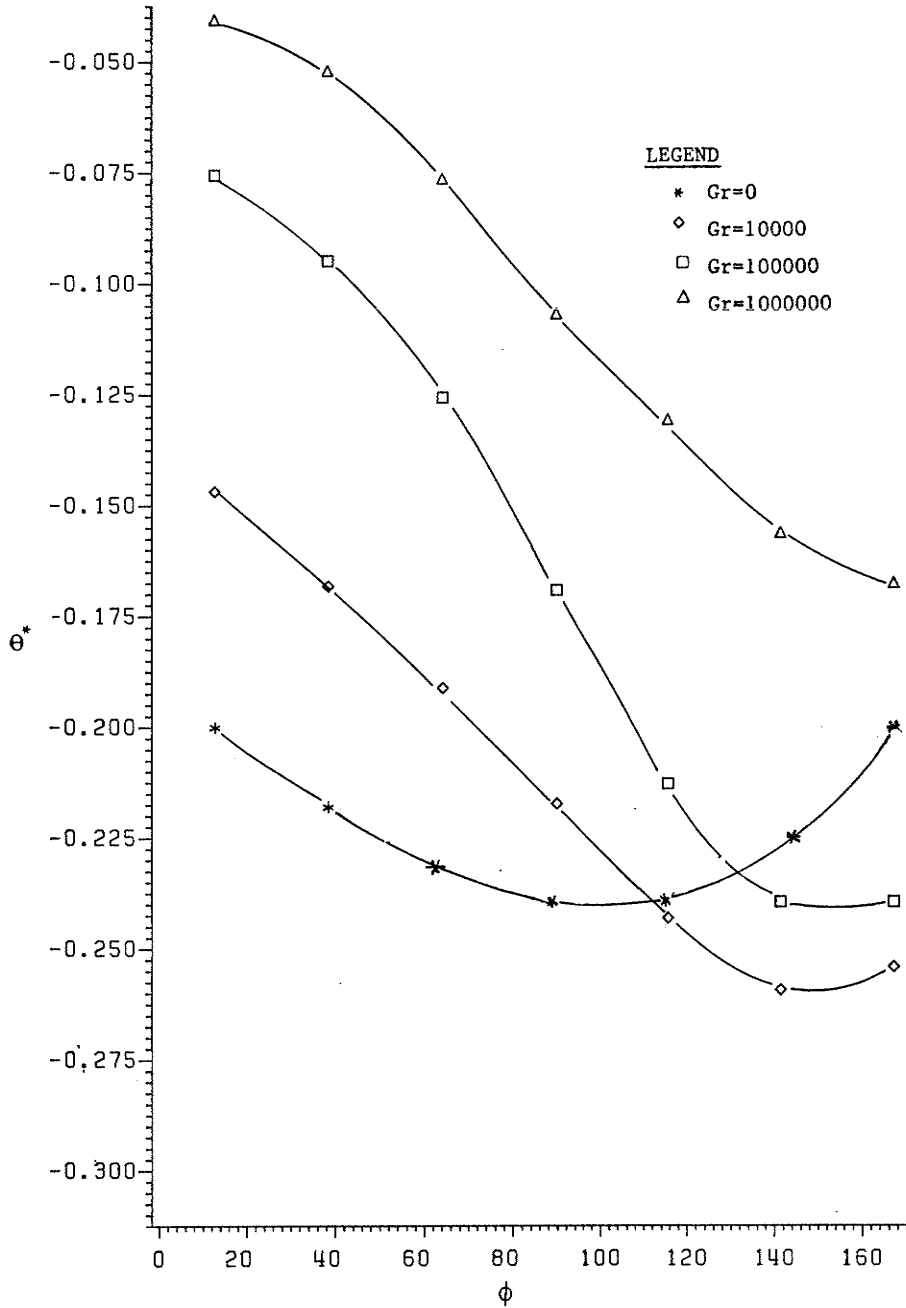
Fig. 5.36 Angular Variation of Temperature (R=0.5625, H=0.25)

values of Gr, colder fluid no longer exists on the lower half of the vertical center plane but is shifted away from it.

The case of H=0.5 is shown in figures 5.37 and 5.38. A first glance at figure 5.37 confirms the notion that as the fin height increases, effects of free convection are felt at very high heating loads. This was observed when velocity fields were examined. Here, the difference between θ^* values at Gr=0 and 10^4 is very small. Figure 5.38 illustrates the variation of θ^* around R=0.5625. This figure provides two important observations. First, location of cold fluid is seen to be bounded by the $\phi=90°$ and $\phi=140°$ lines. This observation verifies the previous deductions. Second and more importantly is the study of temperature gradients at the top ($\phi=0°$) and the bottom ($\phi=180°$) fins. At the top fin, the largest temperature gradient exists for Gr=0. As the value of Gr is increased, magnitude of this gradient is decreased. At the bottom fin however, the situation is reversed. It is therefore concluded that increasing free convection effects make the top fin less and the bottom fin more efficient in terms of heat transfer.

Figures 5.39 and 5.40 describe the temperature distribution for H=0.75 geometry. In figure 5.39, values of θ^* near the center are no longer the minimum values. This is due to the presence of long fins which come close to the center. For this value of H and near the center, the secondary flow was seen to be moving upwards with an appreciable velocity. It implies that fluid is hot in that region. Relative minima for θ^* is seen in the interval of
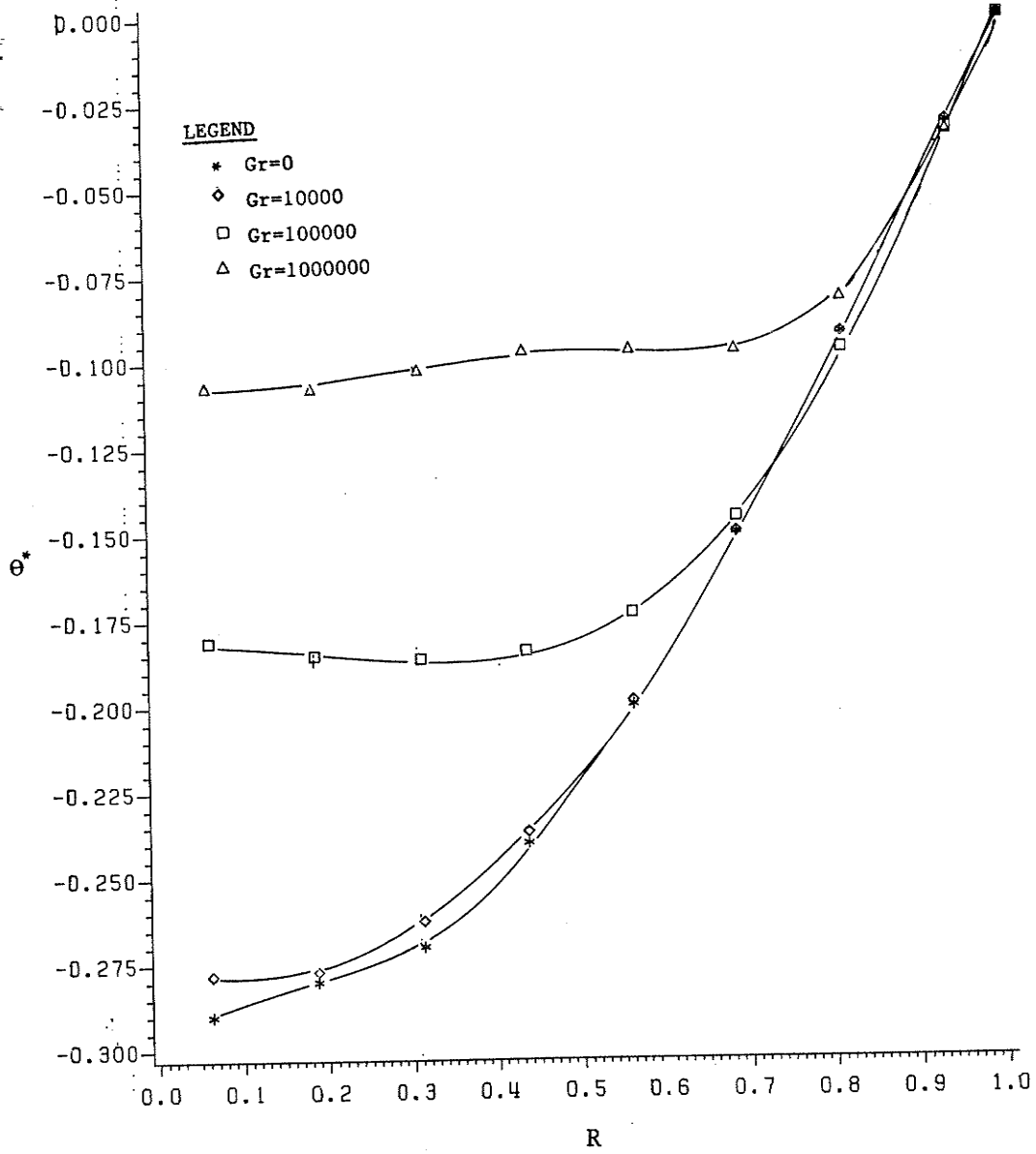
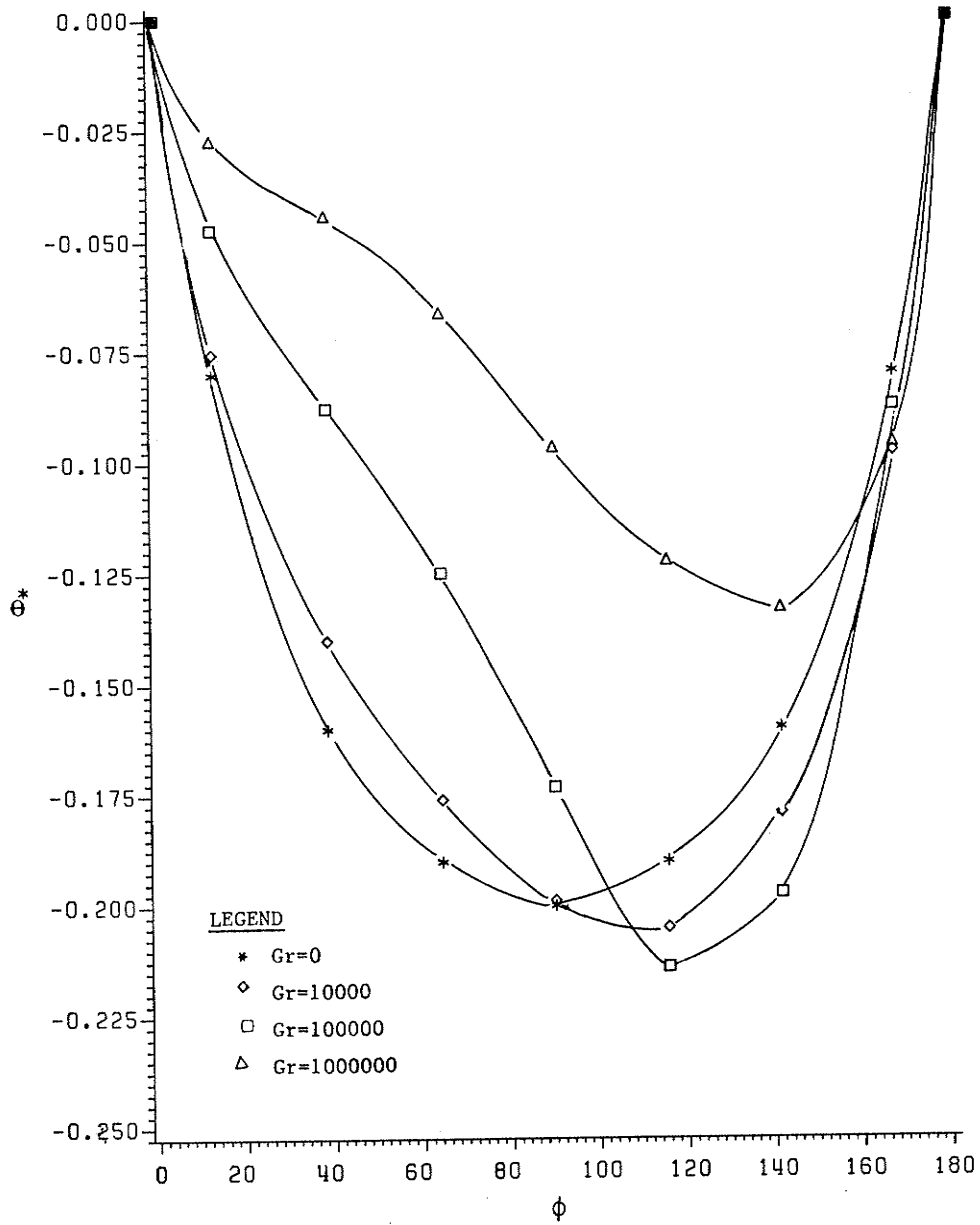Fig. 5.37 Radial Variation of Temperature ($\phi=90^{\circ}$, H=0.50)

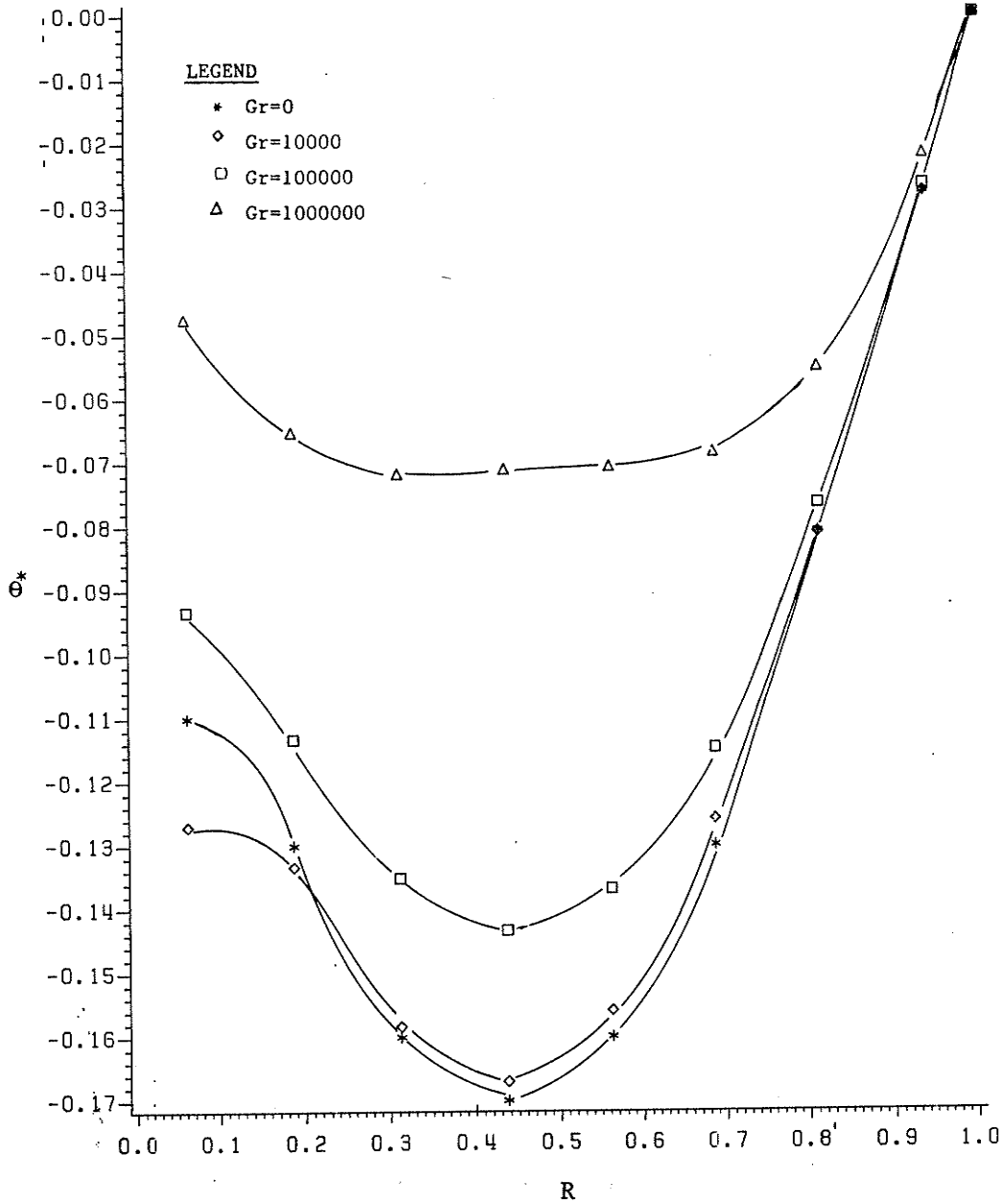Fig. 5.38 Angular Variation of Temperature (R=0.5625, H=0.50)

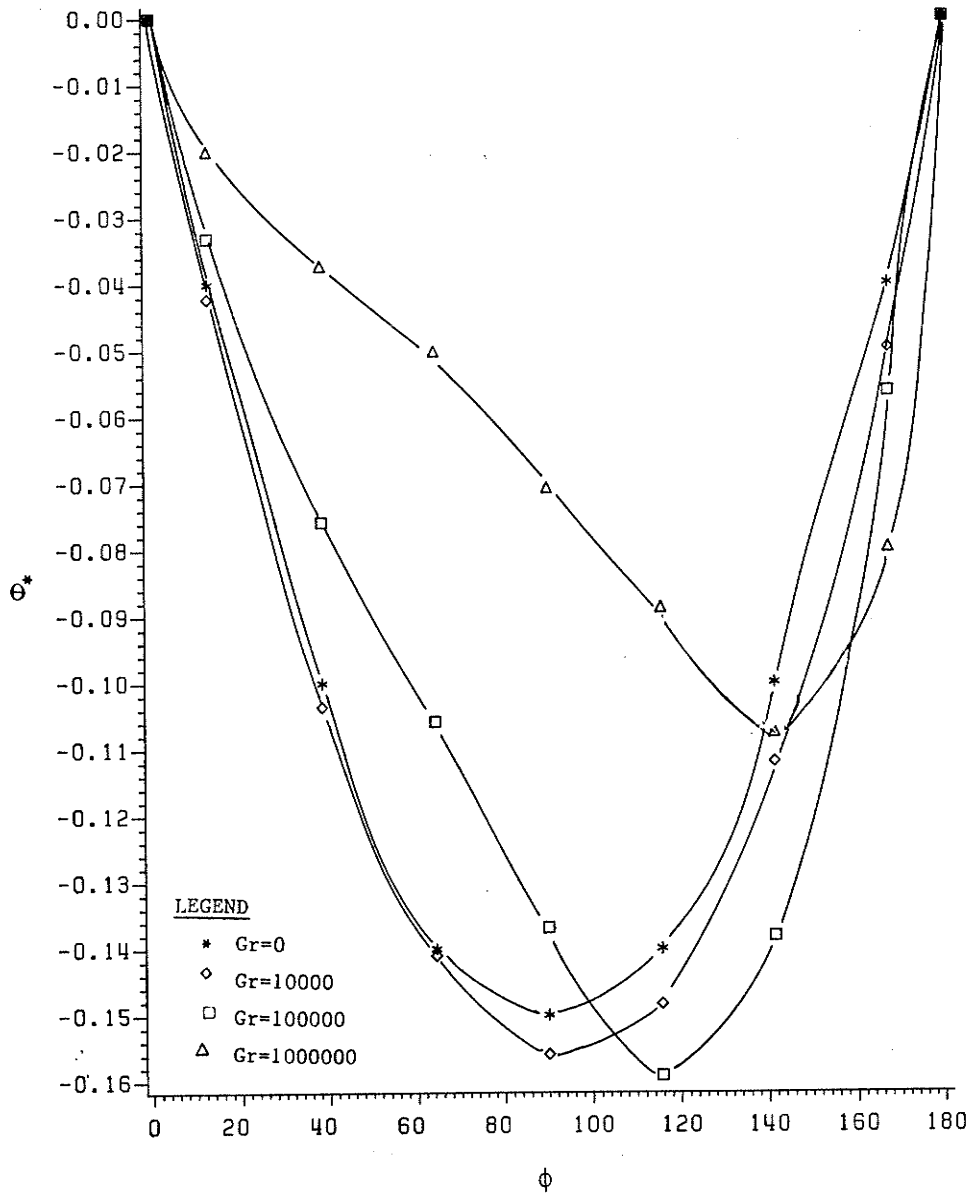Fig. 5.39 Radial Variation of Axial Velocity ($\phi=90^{\circ}$, H=0.75)

Fig. 5.40 Angular Variation of Temperature (R=0.5625, H=0.75)

R=0.4 to R=0.5. The pattern of secondary flow explains this behaviour. As stated earlier, for H=0.75 secondary flow moves in at least two loops, and the temperature profiles in figure 5.39 are a result of this process. The distribution of θ^* for the Gr=10^6 case is seen to be flat over a large area. This is expected in the light of figure 5.18. A general conclusion drawn from figure 5.39 is that for an H of 0.75, significant effects of free convection are felt at Gr values greater than 10^4. In figure 5.40, the angular variations of θ^* are plotted around R=0.5625. Increasing heating loads have the effect of shifting the minimum temperature away from the ϕ=90° line. Temperature gradients at the top and the bottom fins clearly illustrate the relative effectiveness of the two fins.

The case of H=1.00 is shown in figures 5.41 and 5.42. Figure 5.41 shows similar θ^* distribution as figure 5.39. At the center however, due to the presence of solid surface, fluid temperature is equal to the wall temperature. The two loop pattern of the secondary flow explains the occurance of minima at about R=0.5. Difference between the cases of Gr=10^4 and Gr=10^5 is smaller than the corresponding difference at H=0.75. Free convection effects are now appreciable only at Gr values of about 10^6. Since the magnitude of temperature near the center of the tube is almost equal to the one near the circular wall, it is expected that the two regions are equally effective heat transfer surfaces. In figure 5.42, the temperature gradients at the top and the bottom fins exhibit trends similar to the previous cases. Top fin
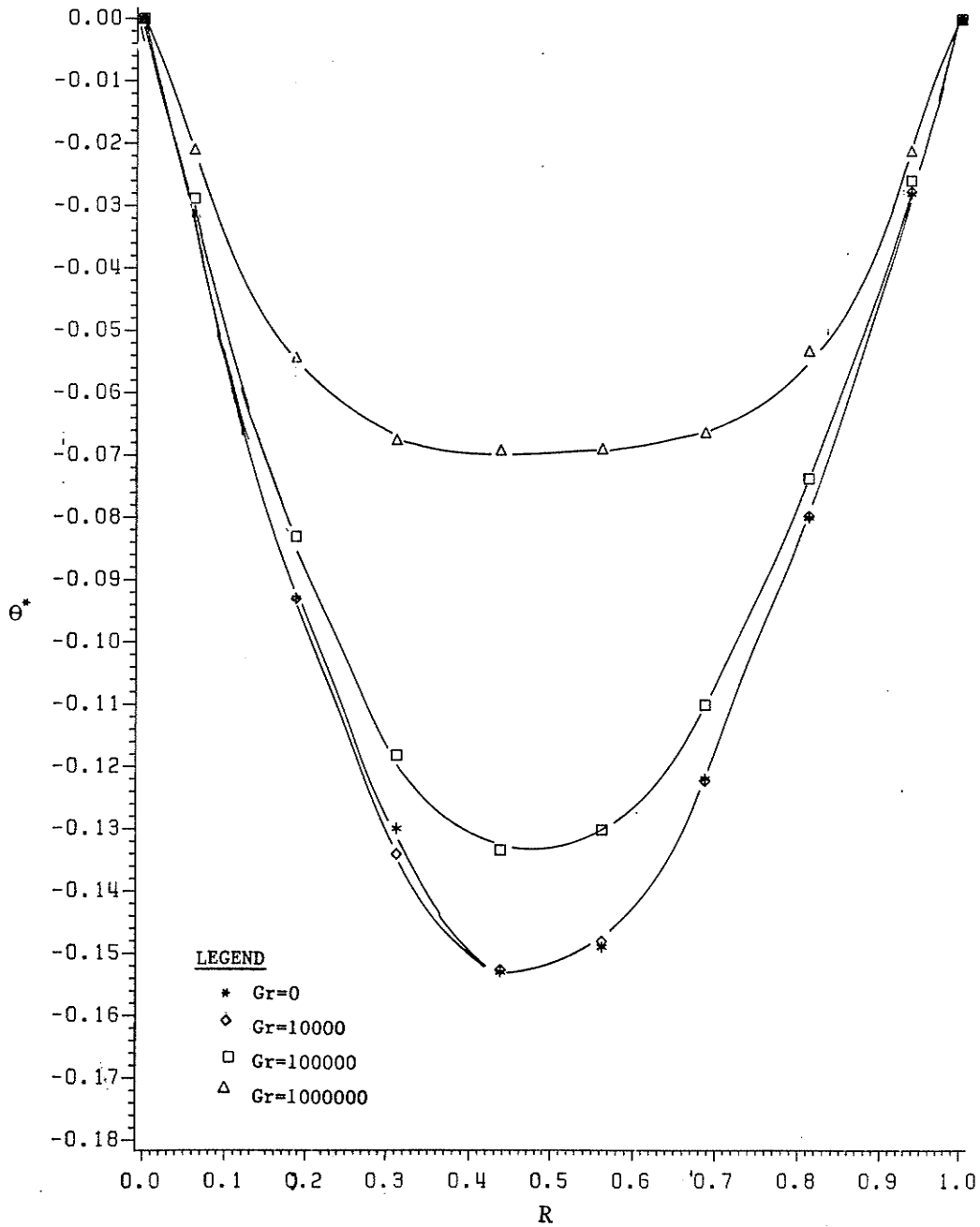
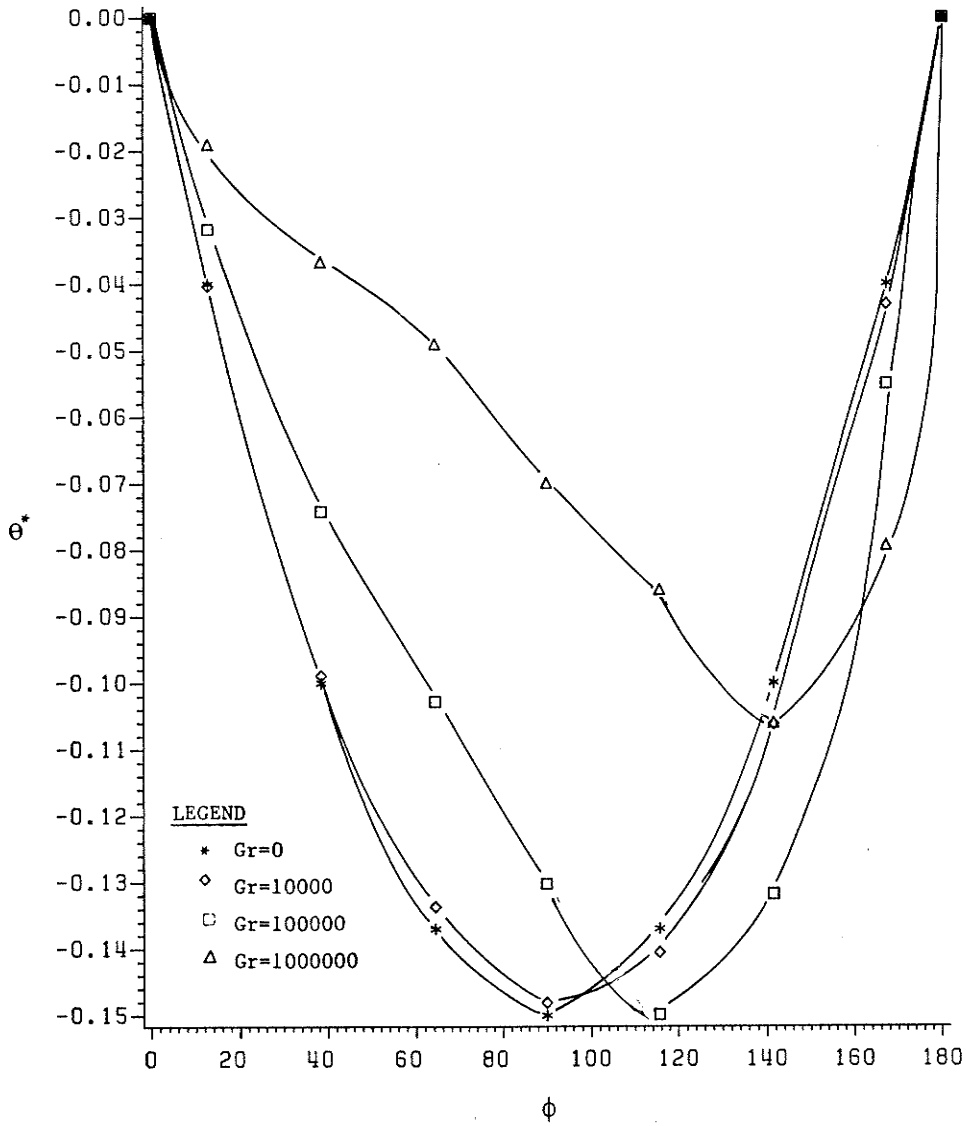Fig. 5.41 Radial Variation of Temperature ($\phi=90^\circ$, H=1.00)

Fig. 5.42 Angular Variation of Temperature (R=0.5625, H=1.00)

transfers a smaller fraction of heat while, the bottom fin has now become a more effecient heat transfer surface. Magnitudes of θ^* are however slightly higher than the H=0.75 case.

5.3   DISTRIBUTION OF LOCAL HEAT FLUX

A study of the temperature distribution of the previous section indicates a variation in the local heat flux distribution around the tube circumference and along the fins. For forced convection, such a variation was investigated by Soliman et al.[27]. In order to explore the effects of free convection, distribution of local to mean heat flux ratios were calculated around the tube circumference, and along the fins. These distributions are shown in figures 5.43 to 5.55.

Figure 5.43 is the only necessary one for the smooth tube case. It illustrates the distribution of local to mean heat flux ratios around the tube circumference. As expected, no variation is observed for pure forced convection (Gr=0). As the heating loads are increased, the bottom half of the tube is. seen to be transfering more heat than the top. Maximum values are observed at $\phi=180°$ This kind of variation was expected. The rate of heat transfer is proportional to the radial temperature gradients at the wall. At the bottom part of the tube, presence of colder fluid greatly increases the gradients, therefore, maximum heat transfer takes place in that region. As was observed, coldest fluid existed along the lower half of the vertical plane and maximum heat is transferred at that point.
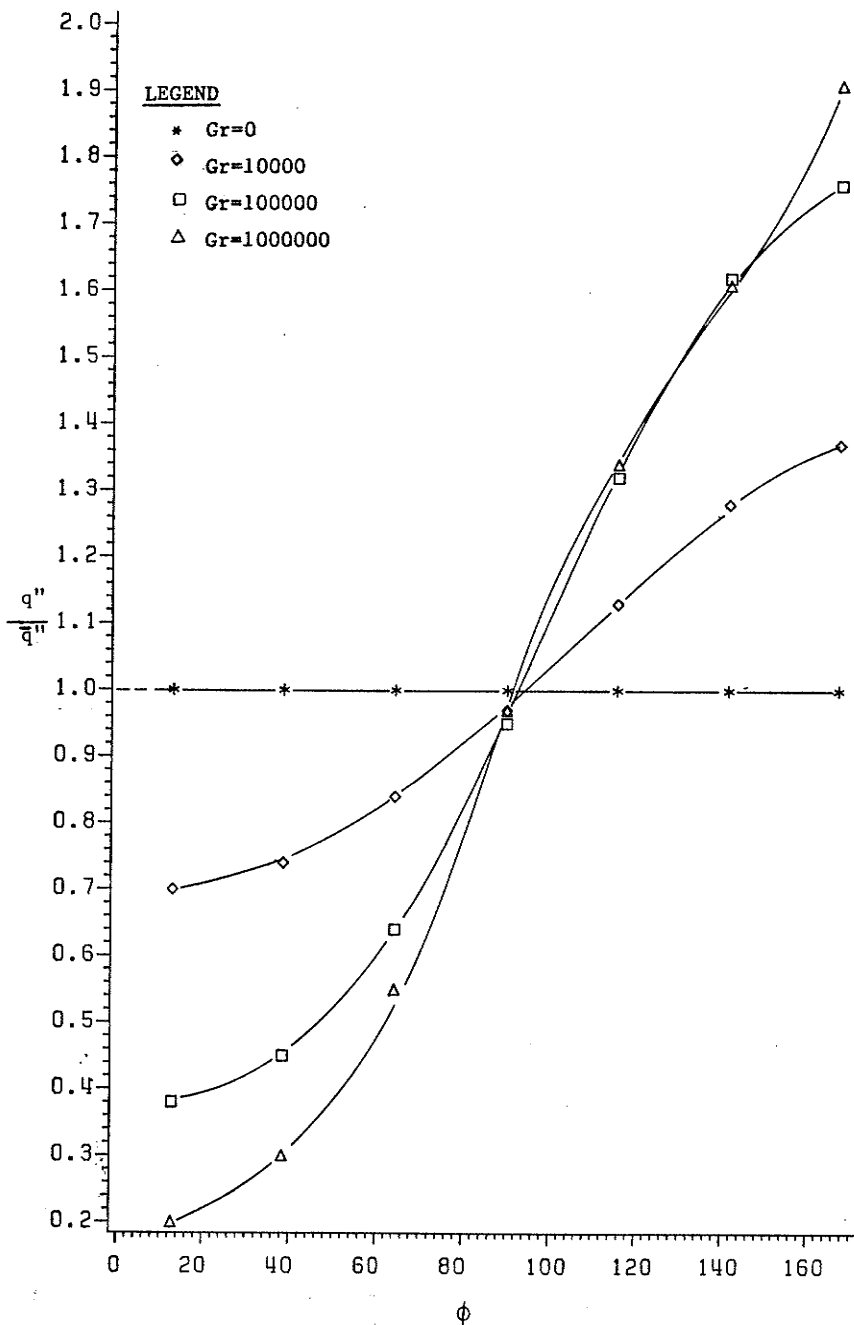
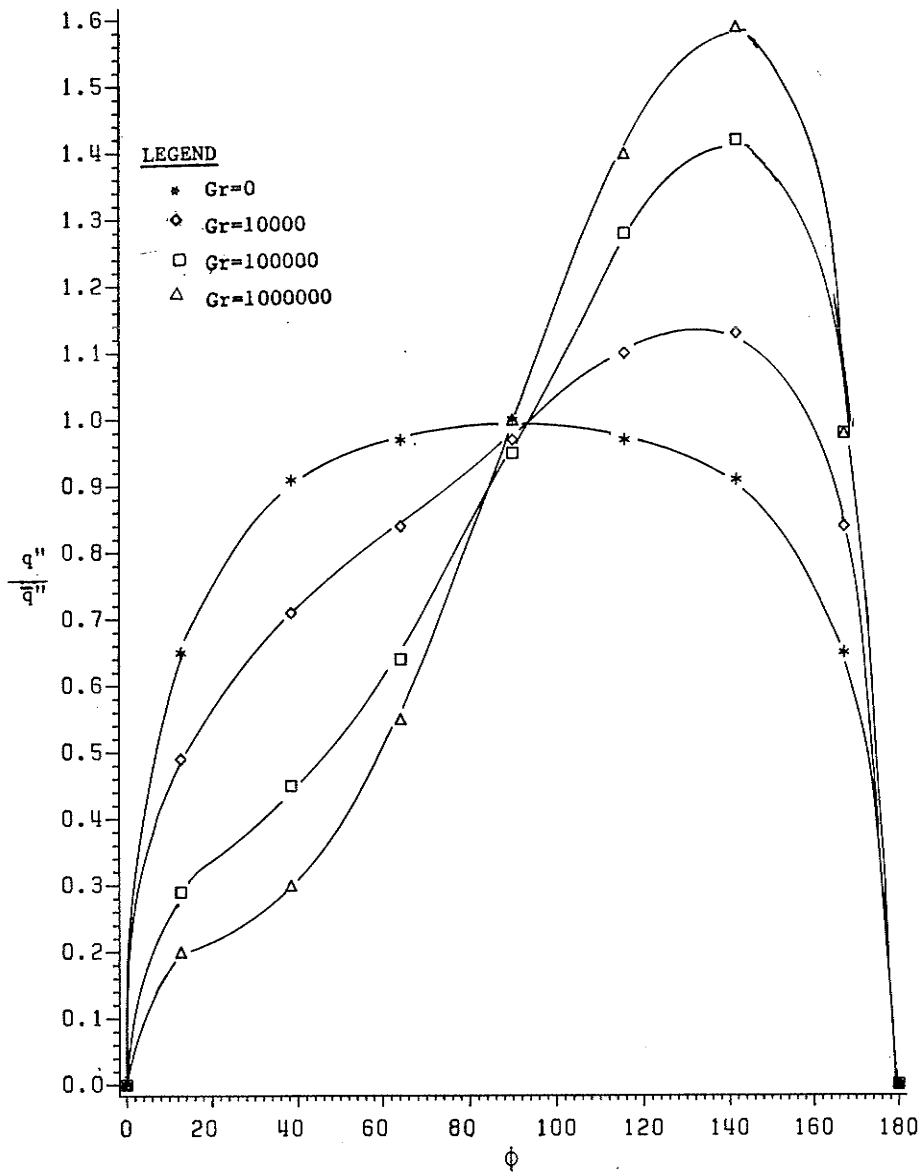Fig. 5.43 Variation of Local Heat Flux around the Tube Wall (H=0.0)

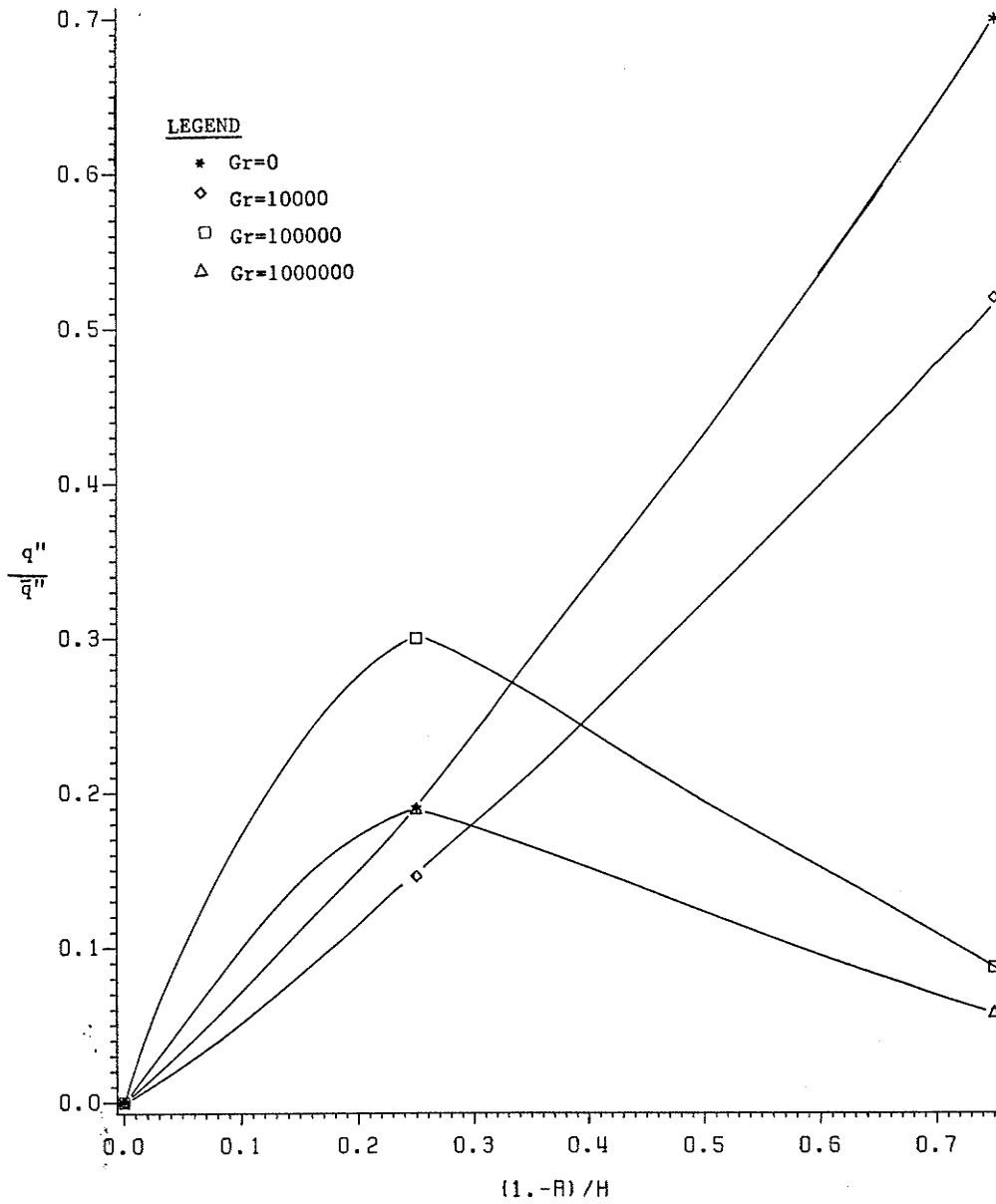Fig. 5.44 Variation of Local Heat Flux around the Tube Wall (H=0.25)

Fig. 5.45 Variation of Local Heat Flux along the Top Fin (H=0.25)

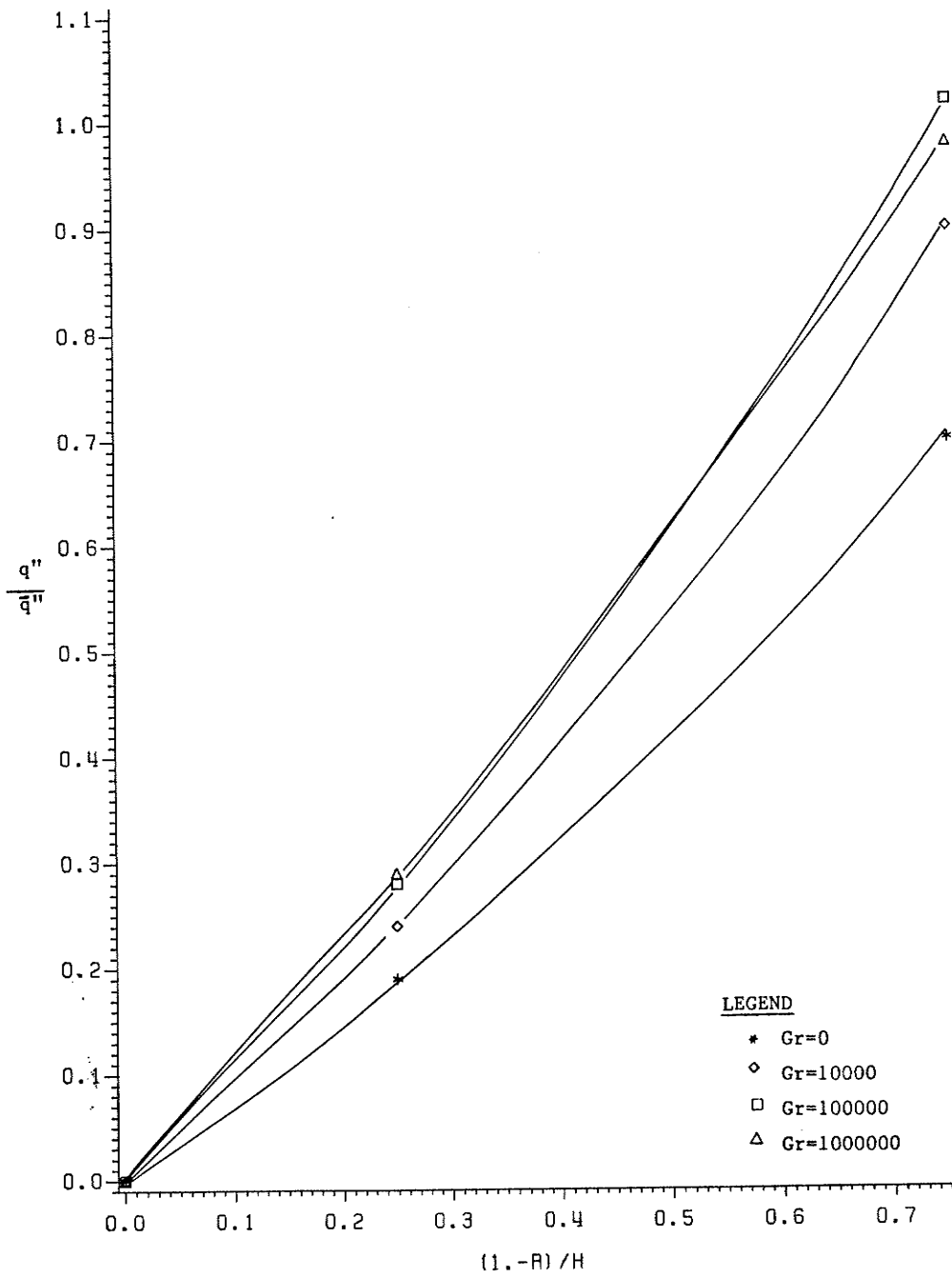Fig. 5.46 Variation of Local Heat Flux along the Bottom Fin (H=0.25)

Figures 5.44 to 5.46 illustrate the H=0.25 case. Figure 5.44 shows the distribution of heat flux around the circular wall. For Gr=0, the distribution is symmetric around the horizontal bisector of the tube. Maximum value is seen at $\phi=90°$. As the heating loads are increased, the lower part of the tube-wall becomes a more efficient heat transfer surface; an opposite trend is observed in the upper half. Maximum values are clustered in the $\phi=120°$ to $\phi=140°$ region. As was seen, location of colder fluid shifted away from the lower half of the vertical center plane when fins were introduced. It explains the location of maxima in this figure. Figures 5.45 and 5.46 show the distribution of heat flux along the top and bottom fins, respectively. The circular wall seems to remain the major heat transfer surface by virtue of its area. At the top fin, the heat flux distribution for Gr=0 and 10^4 starts from zero at the fin base and increases towards the tip. This kind of distribution was reported by Soliman et al.[27]. As the effects of free convection are increased, the top fin shows a change in the form of heat flux distribution. Maximum heat flux exists at the middle region of the fin rather than at the tip. At the bottom fin (shown in figure 5.46), the increase in heat flux is monotonic from the base to the tip for all values of Gr. Higher values of Gr force a higher proportion of heat transfer when compared with the top fin.

The heat flux distributions for the H=0.5 case are illustrated in figures 5.47 to 5.49. Circumferential heat distribution curves of figure 5.47 surround lesser areas than their
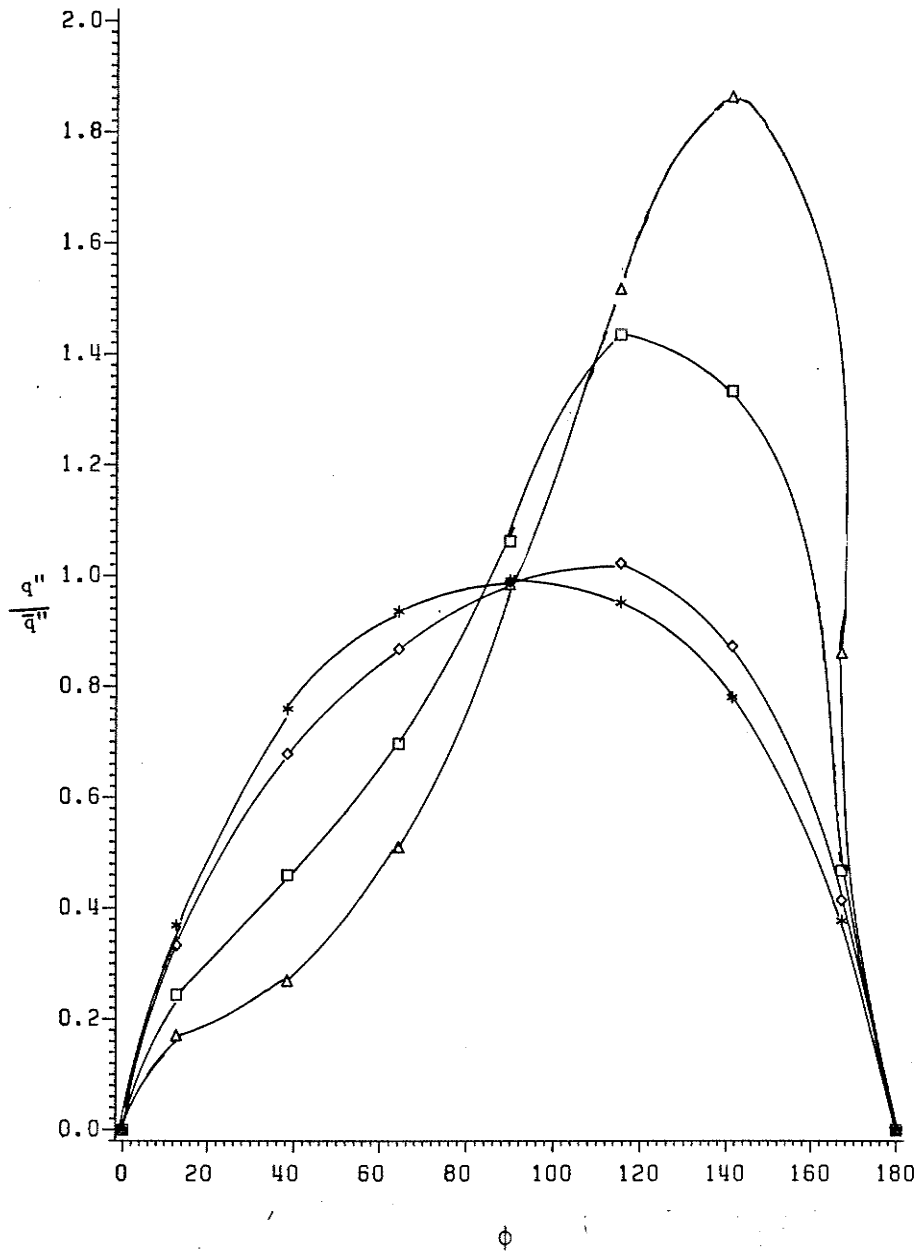
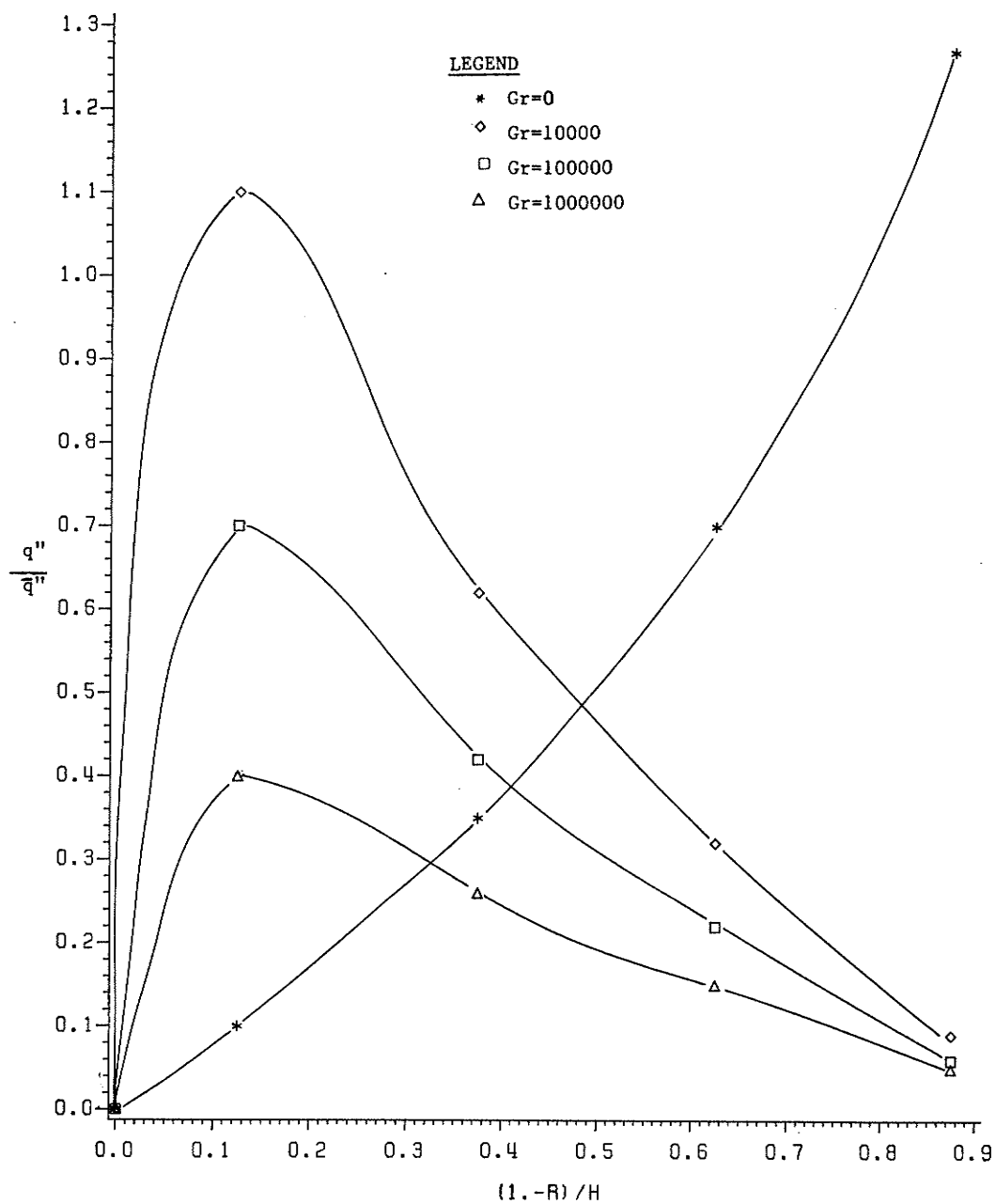Fig.5.47 Variation of Local Heat Flux around the Tube Wall (H=0.50)

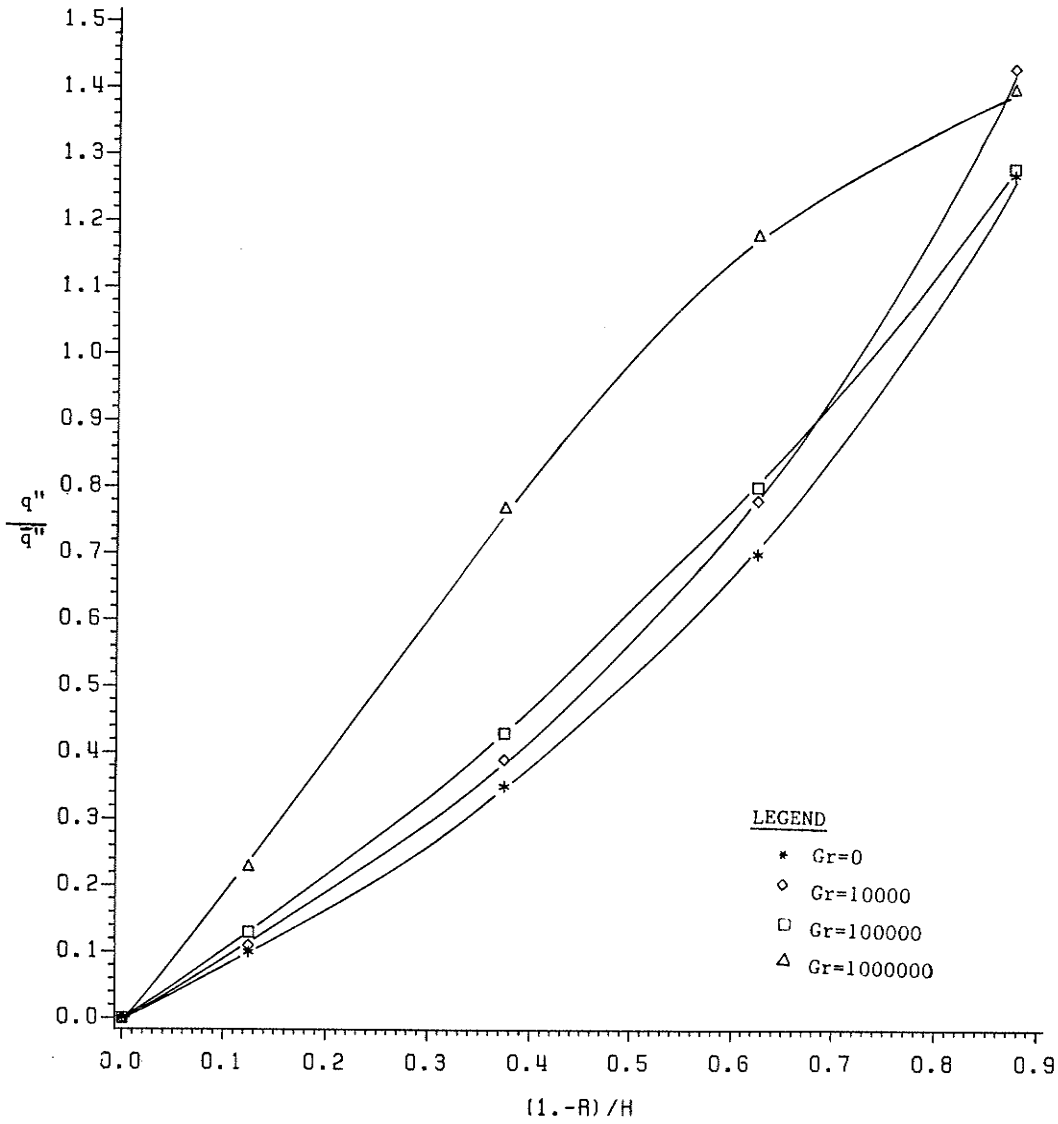Fig.5.48 Variation of Local Heat Flux along the Top Fin (H=0.50)

Fig. 5.49 Variation of Local Heat Flux along the Bottom Fin (H=0.5)

H=0.25 counterparts. This reduction in area is an indication that the fins have become more effective heat transfer surfaces. For the value of Gr upto 10^4, the curves are almost symmetrical around $\phi=90°$. As the heating is increased, the bottom part of the tube is seen to be transfering much more heat than the top. Location of maxima, which is an equivalent to the maximum temperature gradients, indicates the coldest fluid region. Along the top fin, as shown in figure 5.48, increasing values of Gr have not only lowered the magnitude of heat flux distribution, but maximum heat is seen to be transfer ed close to the base of the fin. Near the tip, heat dissipation is almost negligible. As illustrated in figure 5.49, along the bottom fin, the heat flux is monotonically increasing from base to tip for all values of Gr. Clearly, maximum heat is transfered near the fin tip. Unlike other cases, the curve for Gr=10^6 is concave down. This shows that from base to the middle of the fin, heat dissipation increases rapidly. As the tip is approached, rate of dissipation slows down. Although the heat flux ratios are not available at the fin tip, it can be infered that for even higher heating loads (Gr > 10^6), maximum value of heat flux may not exist at the fin tip.

Heat flux distributions for a relative height H of 0.75 are presented in figures 5.50 to 5.52 In figure 5.50, magnitudes of local heat flux are significantly decreased from all the previous cases. It simply implies that a larger portion of heat is now being transfered at the fins. Difference between the case of Gr=0 and 10^4 is insignificant. For higher values of Gr, more heat is
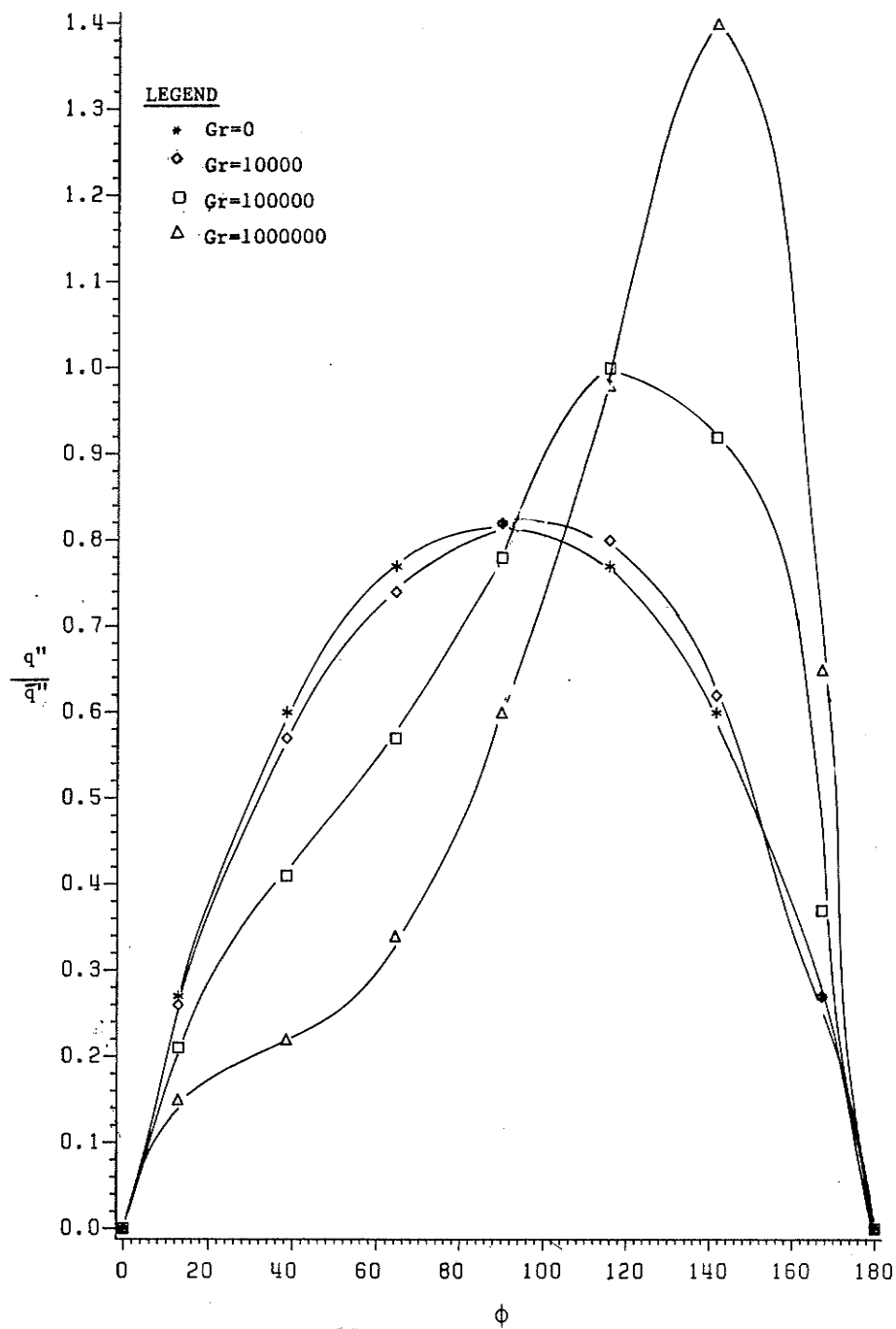
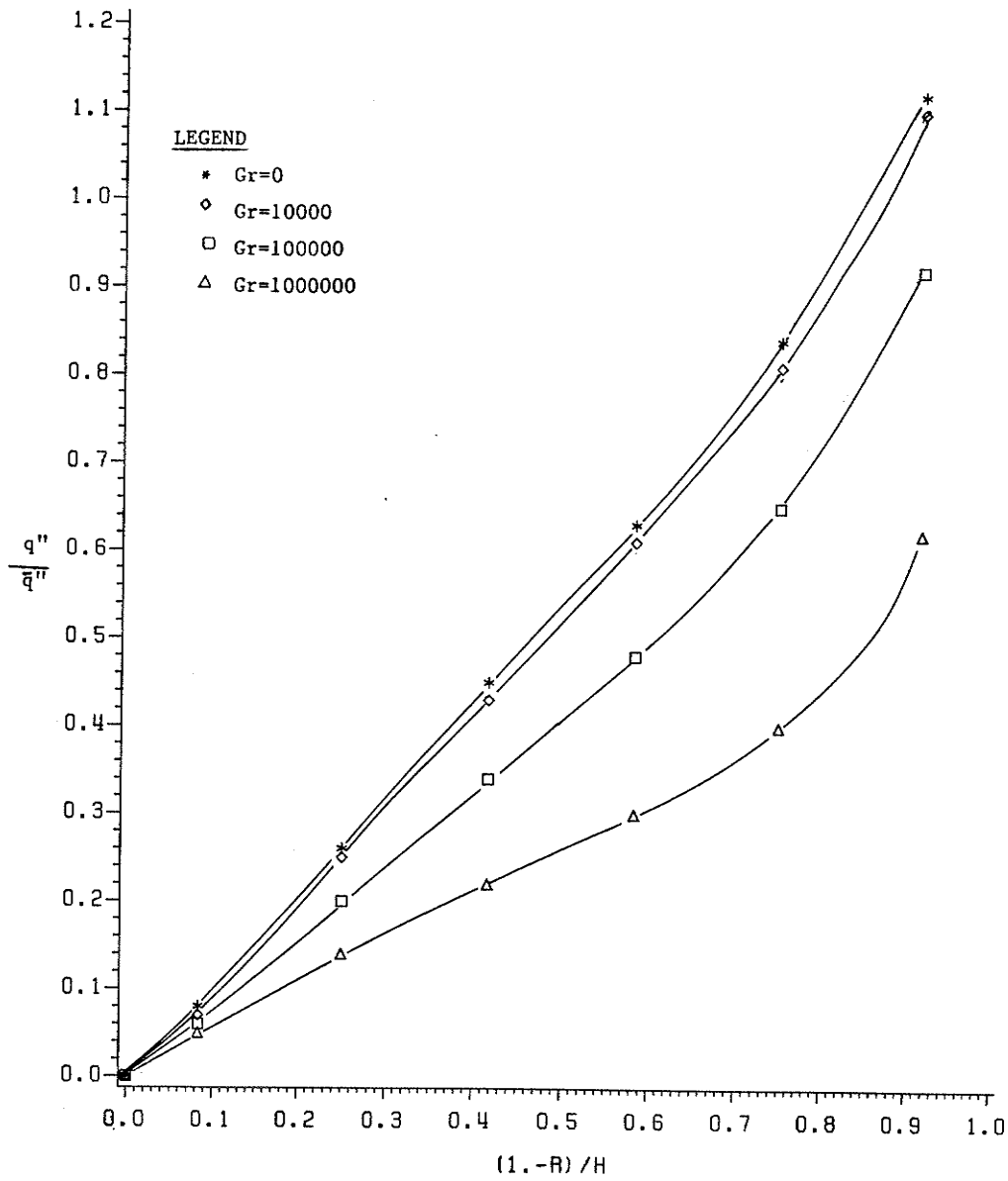Fig. 5.50 Variation of Local Heat Flux around the Tube Wall (H=0.75)

Fig. 5.51 Variation of Local Heat Flux along the Top Fin (H=0.75)

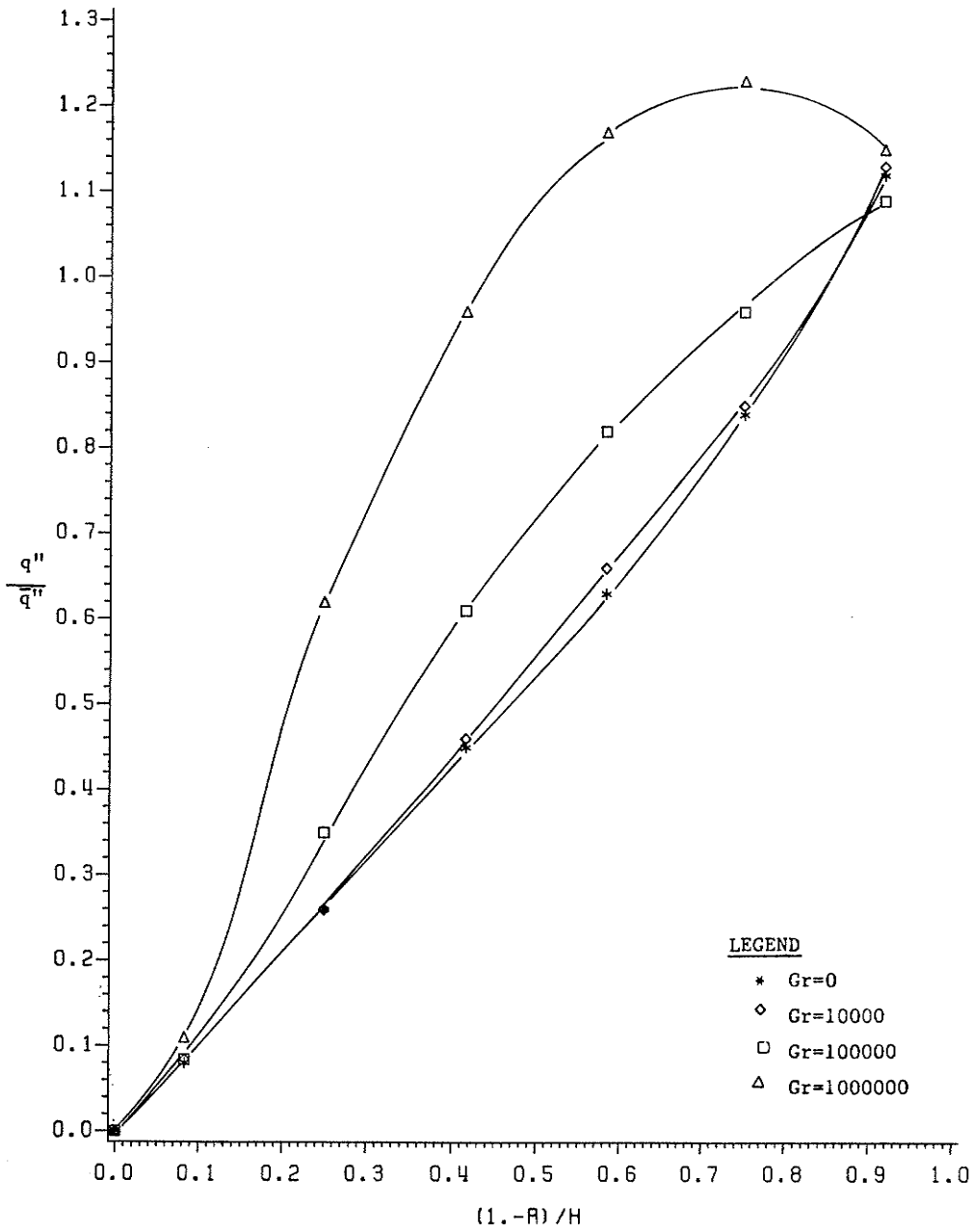Fig. 5.52 Variation of Local Heat Flux along the Bottom Fin (H=0.75)

transfer ed in the bottom part of the tube. Difference between heat transfer effectiveness for Gr=10⁵ and 10⁶ is very large in the bottom part of the tube. Figure 5.51 shows a drastic difference from all previous cases of H. At the top fin, although the maximum heat transfer effectiveness occurs at Gr=0, distribution of heat flux is seen to be monotonically increasing from base to tip for all Gr. At Gr=10⁶, minimum values of $q''/\bar{q}''$ are noticed. Recalling the distribution of secondary velocities near this region, an upward flow was observed near the top fin. Near the tip, motion with reduced upward velocities indicated the presence of colder fluid. However, near the base, those velocities had a larger magnitude. This secondary flow pattern explains the heat flux distribution. An examination of figure 5.52, which shows the heat flux distribution along the bottom fin, indicates the magnitudes of $q''/\bar{q}''$ to be monotonically increasing from base to tip. Clearly, this behaviour is strictly true for Gr=0 and 10⁴. At higher values of Gr, curves are concave downwards implying that maximum heat transfer occurs between the base and the tip. At Gr=10⁶, this maximum is at (1-R)/H value of about 0.75. A general conclusion therefore is that maximum heat transfer effectiveness is transfer ed to the bottom fin and lower part of the tube-wall.

Figures 5.53 to 5.55 correspond to the full fin case (H=1.0). Figure 5.53 being very similar to figure 5.50, shows that the circumferential distributions of heat flux for H=1.0 and H=0.75 are similar. An insignificant decrease of magnitudes is however observed. It can be attributed to increased heat trans-
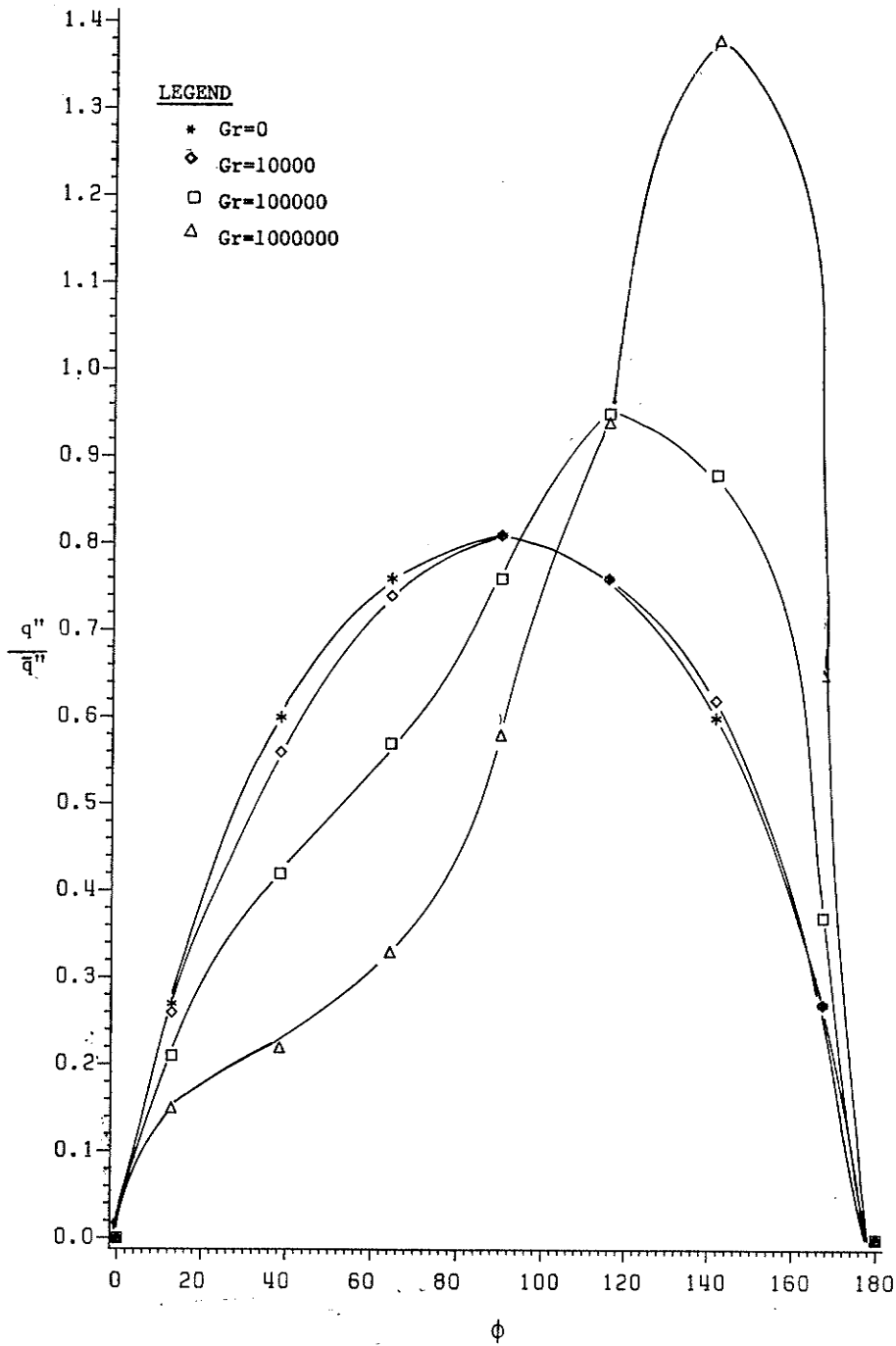
Fig. 5.53 Variation of Local Heat Flux around the Tube Wall (H=1.0)
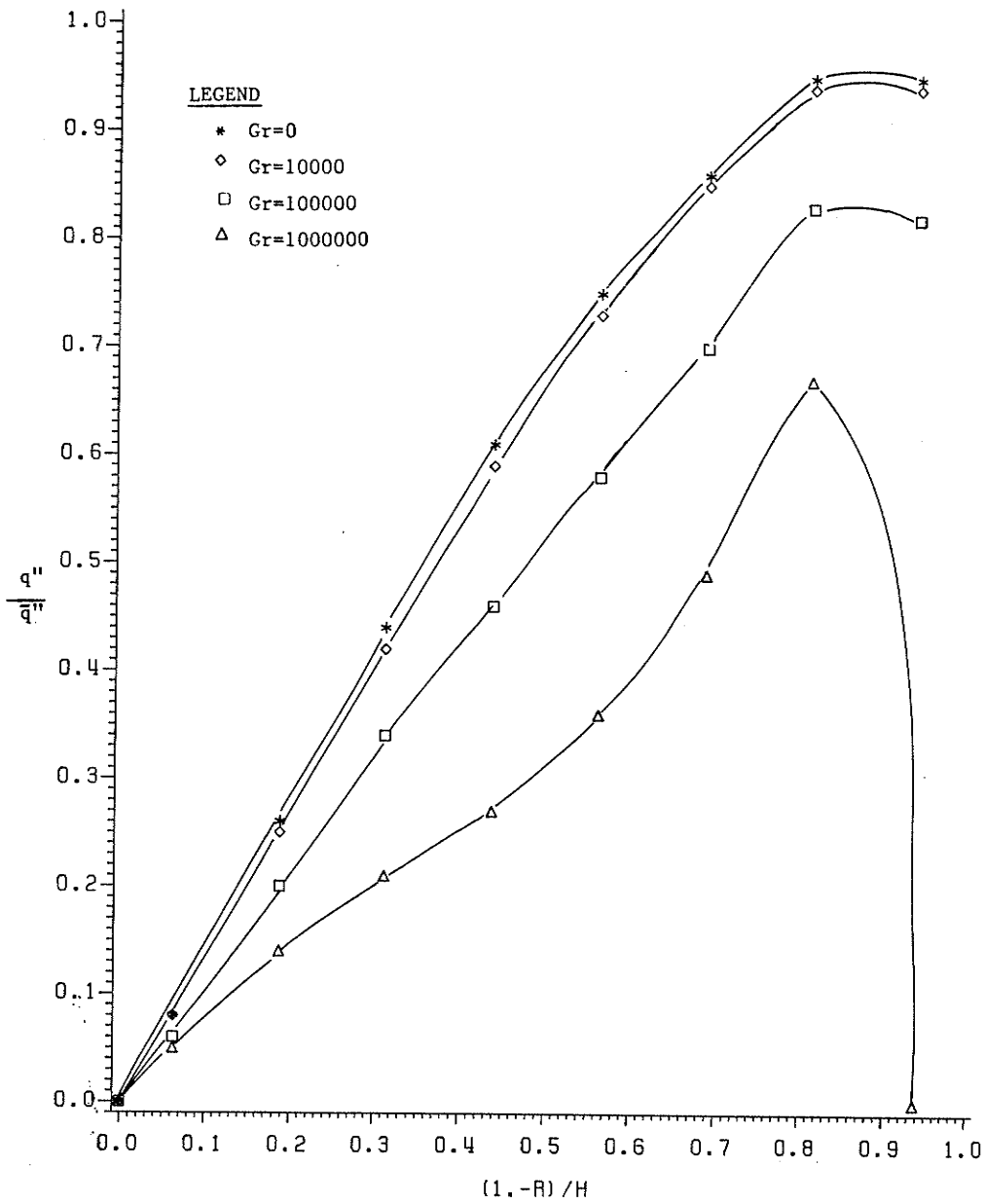
Fig. 5.54 Variation of Local Heat Flux along the Top Fin (H=1.0)
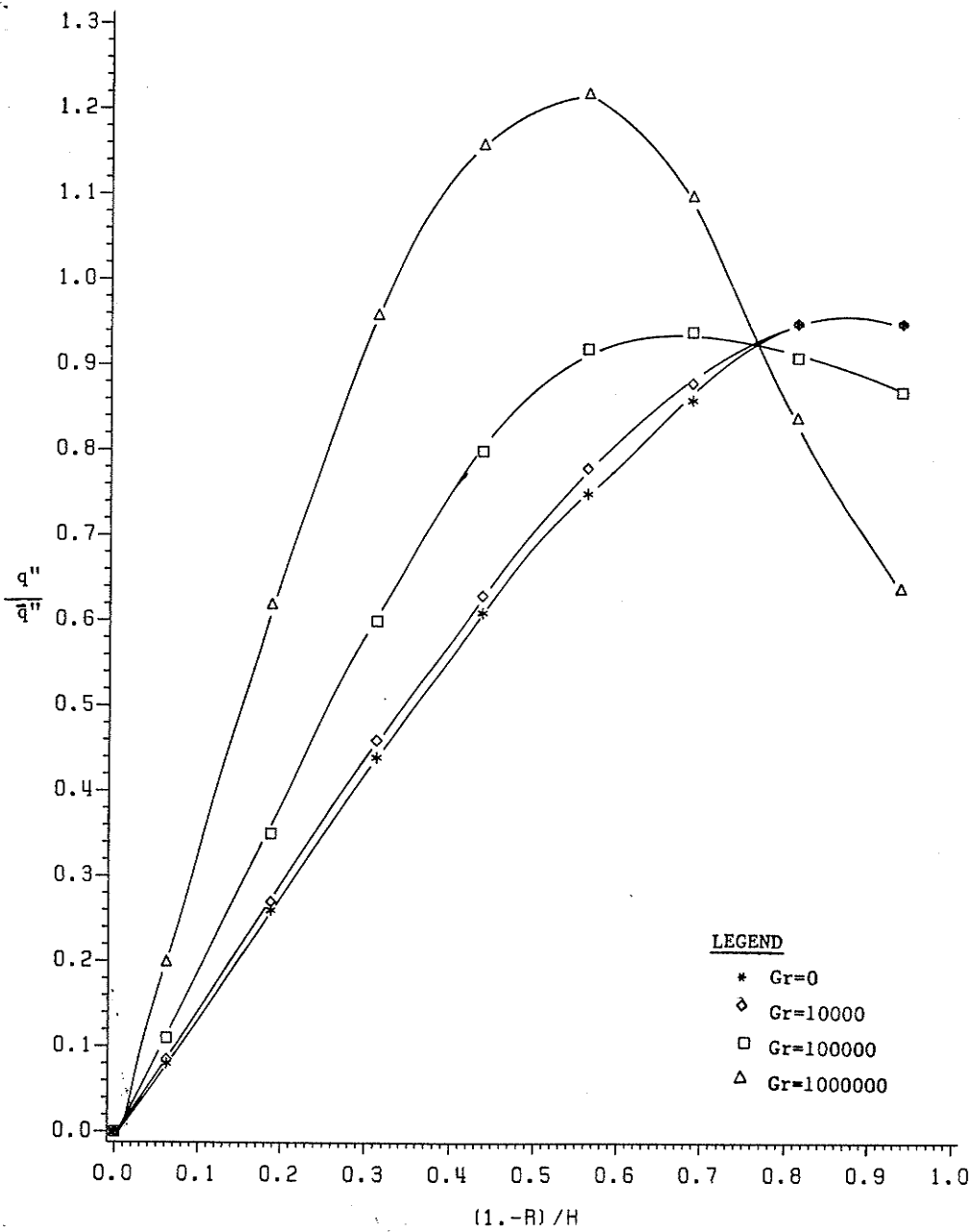
Fig. 5.55 Variation of Local Heat Flux along the Bottom Fin (H=1.0)

fer area at the vertical center plane. In figure 5.54, although

the curves are showing an increase of heat flux from the base to

the tip, they are all concave downwards. Maximum values of heat

flux for all values of Gr exist near the tip. At Gr=10⁶ however,

as the tip is approached, a sharp decrease in the magnitude of

heat flux is observed. Along the bottom fin as shown in figure

5.55, all maxima for heat flux distribution exist at some dis-

tance away from the tip. As the value of Gr increases, these max-

ima shift towards the base and are confined close to the middle

of the fin.

5.4 OVERALL FRICTION FACTORS:

Axial velocity distribution discussed in an early section

indicated a substantial variation of surface friction as a func-

tion of Grashof number and tube geometry. The following procedure

was used to evaluate the fRe values. The integral in the right

hand side of equation (3.20) can be simplified as follows:

$$\frac{dP}{dZ} = \frac{-1}{\frac{2}{\pi} \ \Sigma \ \frac{W}{R} \ \Delta A} \tag{5.1}$$

The summation is carried out inside the flow domain. ΔA which

expresses the area of mesh element is given by:

$$\Delta A = R \Delta R \Delta \phi \tag{5.2}$$

Therefore

$$\frac{dP}{dZ} = \frac{-\pi}{(2\Delta R\Delta\phi \ \Sigma \ W)} \qquad (5.3)$$

Dimensional values of axial pressure gradient and friction factor are related as [34]:

$$-\frac{dp}{dz} = \frac{4 \ f}{2 \ r_0} \ \frac{\rho w_b^2}{2} \qquad (5.4)$$

Therefore

$$f = \frac{r_0}{\rho w_b^2} \ (-\frac{dp}{dz}) \qquad (5.5)$$

But in nondimensional form:

$$\frac{dP}{dZ} = \frac{r_0^2}{\rho \mu w_b} \ (-\frac{dp}{dz}) \qquad (5.6)$$

Therefore

$$f = \frac{\nu}{r_0 \ w_b} \ (-\frac{dP}{dZ}) \qquad (5.7)$$

or

$$fRe = -2 \frac{dP}{dZ}$$

(5.8)

For comparison, values of fRe at Gr=0 are compared with the series solution proposed by Soliman and Feingold [25]. Table 5.1 illustrates this comparison.

Difference between two sets of values ranges from 0.1% to 10% and can be attributed to the truncation errors in the present analysis. At non-zero values of Gr, no results are available for comparison. Table 5.2 lists the fRe values for all geometries and Grashof numbers considered. Figure 5.56 illustrates the relative increase in fRe values in comparison with those obtained at Gr=0 (for same geometry) as a function of Gr. For smooth tubes, the percentage increase is higher than those for finned tubes at all values of Gr. As the fin height H increases, the relative increase in fRe values as a function of Gr becomes smaller. This is in confirmation with the previous observations on secondary flow. For longer fins, the effect of free convection on surface friction becomes significant at higher heating loads only.

H	Ref (25)	Present Analysis	% difference
0	16.00	15.13	5.43
0.25	18.42	16.65	9.60
0.50	24.75	22.57	8.80
0.75	35.06	34.73	0.10
1.00	42.20	38.13	9.60

Table 5.1 : Comparison of pure forced convective fRe values obtained in the present
analysis with the series solution of Soliman and Feingold (25)

Gr \ H	0	0.25	0.50	0.75	1.00
0	15.13	16.65	22.57	34.73	38.13
10^3	15.13	16.65	22.57	34.75	38.13
10^4	15.80	17.26	22.80	34.75	38.13
10^5	19.95	21.70	25.70	35.90	38.97
10^6	27.30	28.80	31.50	44.30	46.83

Table 5.2 : Mean fRe values for all the cases considered in the present analysis
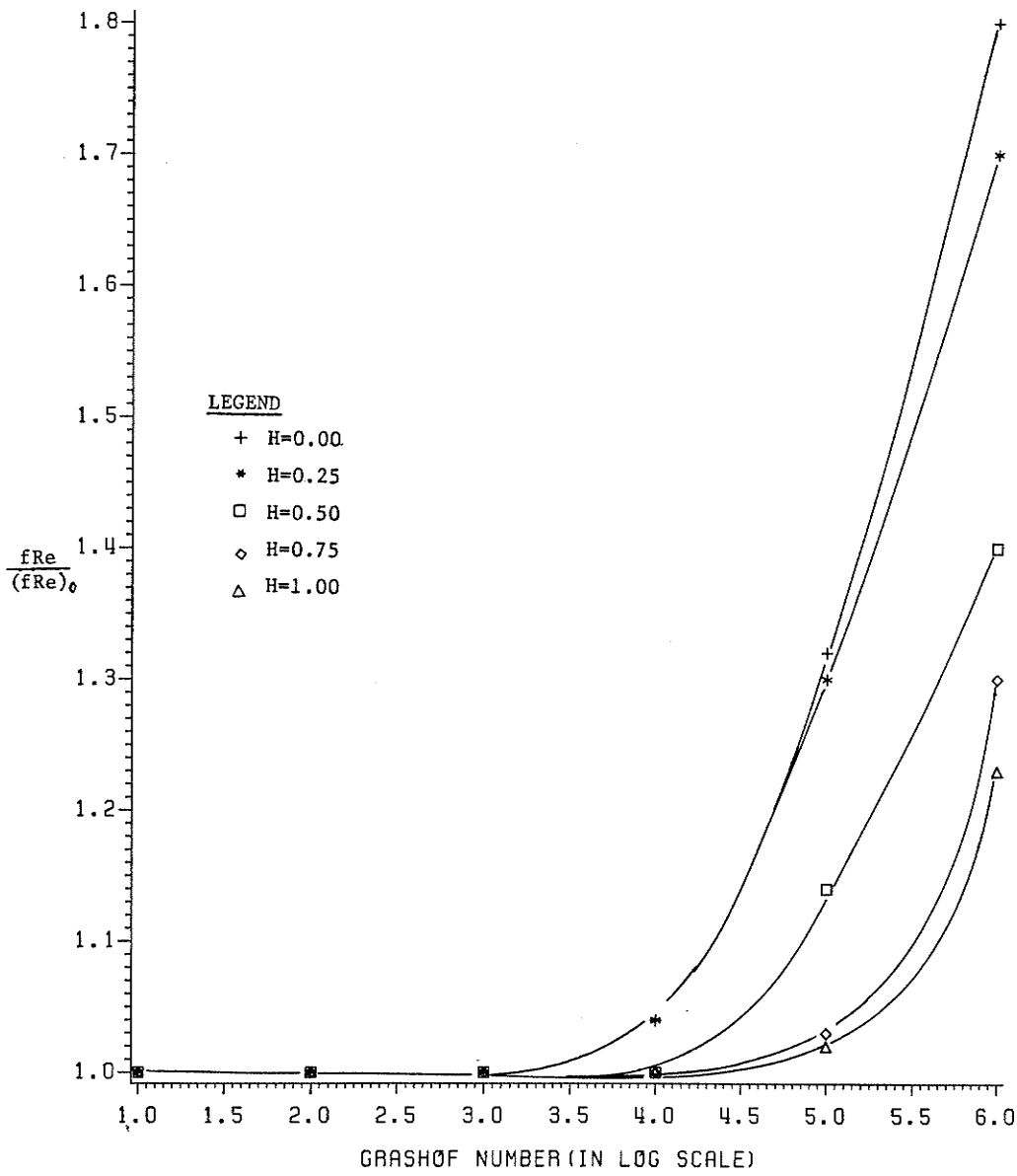
Fig. 5.56 (fRe)/(fRė)$_o$ as A Function of Grashof Number

5.5 NUSSELT NUMBER:

Enhancement of the heat transfer process due to free convection and internal fins has already been discussed. Average values of Nusselt number are reported in this section for all the geometries and heating loads. A quantitative picture of heat transfer enhancement can now be seen.

Average convective heat transfer coefficient "h" is defined as:

$$h = \frac{Q}{2\pi \ r_0 \ (T_w - T_b)} \tag{5.9}$$

and average value of Nusselt number based on h is given as:

$$Nu = \frac{2 \ r_0 \ h}{k} \tag{5.10}$$

After considerable manipulations and using the non-dimensional form of temperature θ_b, Nusselt number can be written as:

$$Nu = \frac{-1}{\theta_b} \tag{5.11}$$

where the bulk value of non dimensional temperature, θ_b, is given as:

$$\theta_b = \frac{2 \ dP/dZ}{\pi} \int_{\phi_{r_0}}^{\pi} \int_{R_{=0}}^{'} \frac{W \ \theta}{R} \ R \ dR \ d\phi \tag{5.12}$$

Assuming the values of W and θ to be constant across each mesh element area, equation (5.12) takes the following form:

$$\theta_b = \frac{2 \ (dP/dZ)}{\pi} \ \Delta\phi\Delta R \ \sum \frac{W \ \theta}{R} \qquad (5.13)$$

Once the values of θ_b are obtained, average value of Nusselt number can be obtained from equation (5.11).

To determine an estimate of the accuracy of the present results, Nu values at Gr=0 are compared with the series solution of Soliman and Feingold [25]. Table 5.3 shows this comparison. Difference between the two sets of values is within 9% . At non-zero values of Gr, no results are available for comparison. Table 5.4 provides the Nusselt number values for all the cases analyzed. To study the relative increase of Nu values as a function of Gr, figure 5.57 which shows all geometries, has been plotted. Interestingly, it is found that the relative increase in heat transfer is much larger then the corresponding increase in fRe values. This is true for all geometries and was predicted when the distribution of axial velocity and temperature were examined.

H	Ref (25)	Present Analysis	% difference
0	4.36	4.33	0.70
0.25	4.97	4.53	8.80
0.50	5.46	5.94	8.70
0.75	10.76	10.27	4.50
1.00	10.89	11.27	3.58

Table 5.3 : Comparison of pure forced convective Nusselt number values obtained in the present analysis with the series solution of Soliman and Feingold (25)

Gr \ H	0	0.25	0.50	0.75	1.00
0	4.33	4.53	5.94	10.27	11.27
10^3	4.33	4.53	5.94	10.27	11.27
10^4	4.57	4.76	6.03	10.28	11.28
10^5	6.38	6.63	7.39	10.90	11.75
10^6	9.70	9.92	11.22	15.33	15.77

Table 5.4 : Mean Nusselt number values for all the cases considered in the present analysis
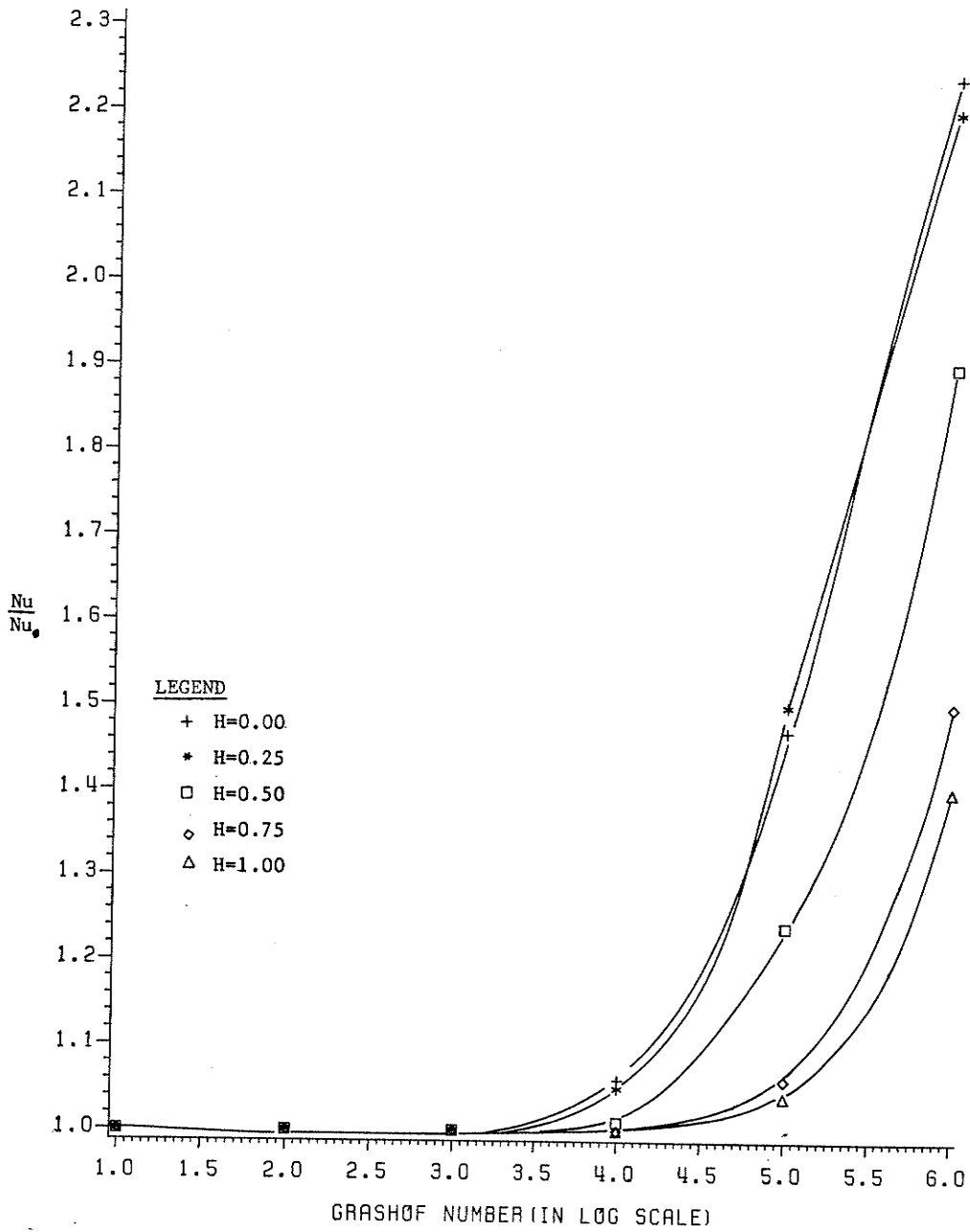
Fig. 5.57 (Nu)/(Nu$_o$) as A Function of Grashof Number

Chapter VI

CONCLUSIONS AND RECOMMENDATIONS

Mixed convection during fully developed laminar flow inside horizontal tubes with two internal fins was investigated numerically. The Method of false transients supplemented by the marker and cell kind of mesh was used to solve the governing partial differential equations. This solution technique proved to be very stable but expensive in terms of computer time. The following conclusions can be drawn from obtained results, which correspond to a Prandtl number of 0.7 and Grashof numbers of up to 10^6:

1. In fully developed laminar flow, free convection effects cannot be ignored when the value of Gr exceeds 10^4.

2. The free convection currents distort the pure forced convective axial velocity and temperature profiles significantly. The bottom part of the tube becomes a more effective heat transfer surface, and offers more resistance to the fluid flow. A reverse trend is observed in the top part.

3. Fins suppress the free convective currents. In general, for long fins ($H \geqslant 0.75$), the free convective effects are significant only at very high Grashof numbers ($Gr \geqslant 10^5$). For shorter fins ($H \leqslant 0.5$) however, although the secondary currents are less intense than the smooth tube, the

- 146 -

effects of free convection are significant even at moderate Grashof numbers (10^4 and up).

4. When free convection is present, the bottom fin becomes a more effective heat transfer surface and offers greater resistance to the flow. On the contrary, the top fin shows an opposite behaviour.

5. Free convection alters the distribution of local heat flux around the tube wall and along the fins. For all tube geometries, the bottom part of the circular wall experiences more heat flux. Along the fins, the heat flux is in general higher at the bottom fin. Along the top fin, maximum heat flux is observed at the middle portion of the fin for shorter fins ($H \leq 0.5$).When fins are long ($H > 0.5$), this maximum occurs at the tip of the top fin. Along the bottom fin, maximum heat flux is seen at the tip for short fins, however, this maximum shifts towards the middle portion of the fin when fins are long.

6. Magnitude of the local heat flux along the fins depends on the heating loads i.e., the values of Gr. At the top fin, increasing the value of Gr decreases the magnitude of heat flux. At the bottom fin, a reverse trend is observed.

7. Relative increases in Nu and f values due to the presence of free convection is found to be maximum for the smooth tubes. As the fins become longer, these relative increases become smaller. In general, the relative increase in Nu values is substantially higher than the corresponding increase in f values.

In future studies, it is proposed that a finer mesh be used to improve the accuracy of the results. As has been demonstrated, the neighbourhood of the tube's center is responsible for the restriction on mesh size. A possible approach could be the use of an uneven mesh which is coarser near the center and relatively finer away from it.

Further, it is recommended that other values of Prandtl number and even higher values of Grashof number be incorporated in the present analysis. Obviously, the case of two fins is a starting point for the mixed convection analysis of the internally finned tubes. It is proposed that in future, the case of more than two fins be studied using similar analysis.

REFERENCES

1. Sabersky, R.H., "Heat Transfer in the Seventies", Int.J. Heat Mass Transfer, Vol 14, 1971, pp. 1927-1949.

2. McComas, S.T., and Eckert, E.R.G., "Combined Free and Forced Convection in a Horizontal Circular Tube", ASME J. of Heat Transfer, Vol 88, 1966, pp. 147-153.

3. Petukhov, B.S., and Polyakov, A.F., "Experimental Investigation of Viscogravitational Fluid Flow in a Horizontal Tube", Scientific Research Institute of High Temperature J., Vol 5, No 1, 1967, pp. 87-95

4. Petukhov, B.S., and Polyakov, A.F., "Effect of Free Convection on Heat Transfer During Forced Flow in a Horizontal Pipe", High Temperature Reasearch Inst. J., Vol 25, No 2, 1967, pp. 384-387.

5. Shannon, R.L. and Depew, C.A., "Combined Free and Forced Laminar Convection in a Horizontal Tube with Uniform Heat Flux", ASME J. of Heat Transfer, Vol 90, 1968, pp. 353-357.

6. Bergles, A.E., and Simonds, R.R., "Combined Forced and Free Convection for Laminar Flow in Horizontal Tubes with Uniform Heat Flux", Int. J. Heat Mass Transfer, Vol 14, 1971, pp.1989-2000.

7. Morcos,S.M., and Bergles,A.E., "Experimental Investigation of Combined Forced and Free Laminar Convection in Horizontal Tubes", ASME J. of Heat Transfer, Vol 99, 1975, pp. 212-219.

8. Browm, A.R., and Thomas, M.A., "Combined Free and Forced Convection Heat Transfer for Laminar Flow in Horizontal Tubes", J. of Mech Engg Science, Vol 7, 1965, pp.440-448.

9. Depew, C.A., and August, C.E., "Heat Transfer due to Combined Free and Forced Convection in a Horizontal and Isothermal Tube", ASME J. of Heat Transfer, Vol 93, 1971, pp.380-384.

10. Yousef, W.W., and Tarasuk, J.D., "An Interferometric Study of Combined Free and Forced Convection in a Horizontal Isothermal Tube", ASME J. of Heat Transfer, Vol 103, 1981, pp. 249-256.

11. Yousef, W.W., and Tarasuk, J.D., "Free Convection Effects on Laminar Forced Convective Heat Transfer in a Horizontal Isothermal Tube", ASME J. of Heat Transfer, Vol 104, 1982, pp.145-152.

12. Hong, S.W., and Bergles, A.E., "Analysis of Combined Forced and Free Convection in Horizontal Tubes", Technical Report HTL-4, ISU-ERT-AMES-74155, Engineering Reasearch Institute, Iowa State University, Ames, Iowa, 1974.

13. Hong, S.W., and Bergles, A.E., "Theoretical Solution for Combined Forced and Free Convection in Horizontal Tubes with Temperature Dependent Viscosity", ASME J. of Heat Transfer, Vol 100, 1976, pp. 459-465.

14. Patankar, S.V., Ramadhyani, S., and Sparrow, E.M., "Effect of Circumferentially Non Uniform Heating on Laminar Combined Convection in a Horizontal Tube", ASME J. of Heat Transfer, Vol 100, 1978, pp. 63-69.

15. Hieber, C.A., and Sreenivasan, S.K., "Mixed Convection in an Isothermally Heated Horizontal Pipe", Int. J. Heat Mass Transfer, Vol 17, 1974, pp.1337-1348.

16. Ou, J.W., and Cheng, K.C., "Natural Convection Effects on Graetz Problem in Horizontal Isothermal Tubes", Int J. Heat Mass Transfer, Vol 20, 1977, pp.953-960.

17. Hishida, M., Nagano, Y., and Montesclaros, M.S., "Combined Forced and Free Convection in the Entrance Region of an Isothermally Heated Horizontal Pipe", ASME J. of Heat Transfer, Vol 104, 1982, pp. 153-159.

18. Bergles, A.E., "Survey and Evaluation of Techniques to Augment Convective Heat and Mass Transfer", Progress in Heat and Mass Transfer, Vol 1, Pergamon Press, 1969, pp. 331-424.

19. Bergles, A.E., and Webb, R.L., "Bibliography of techniques to Augment Heat and Mass Transfer", ASME Publication, New York, 1970, pp. 1-15.

20. Watkinson, A.P., Miletti, D.L., and Kubanek, G.R., "Heat Transfer and Pressure Drop of Internally Finned Tubes in Laminar Oil Flow", ASME Paper No 75-HT-11, 1975.

21. Marner, W.J., and Bergles, A.E., "Augmentation of Tubeside Laminar Flow Heat Transfer by Means of Twisted Tape Inserts, Static Mixer Inserts and Internall Finned Tubes",Proc 6th Int. Heat Tranfer Conference, Toronto, Canada, Vol 2, 1978, pp. 583-588.

22. Hu, M.H. and Chang, Y.P., "Optimization of Finned Tubes for Heat Transfer in Laminar Flow", ASME J. of Heat Transfer, Vol 95, 1973, pp. 332-338.

23. Nandakumar, K., and Masliyah, J.H., "Fully Developed Viscous Flow in Internally Finned Tubes", The Chemical Engineering Journal, Vol 10, 1975, pp. 113-120.

24. Soliman, H.M., and Feingold, A., "Analysis of Fully Developed Laminar Flow in Longitudinal Internally Finned Tubes",The Chemical Engineering Journal, Vol 14, 1977, pp.119-128.

25. Soliman, H.M., and Feingold, A., "Analysis of Heat Transfer in Internally Finned Tubes under Laminar Flow Conditions", Proc 6th Int. Heat Transfer Conference, Toronto, Canada, Vol 2, 1978, pp. 571-576.

26. Soliman, H.M., "The Effect of Fin Material on Laminar Heat Transfer Characterstics of Internally Finned Tubes", Canadian J. of Chemical Engineering, Vol 59, 1981, pp. 251-256.

27. Soliman, H.M., Chau, T.S., and Trupp, A.C., "Analysis of Laminar Heat Transfer in Internally Finned Tubes with Uniform Out-

side Wall Temperature", ASME J. of Heat Transfer, Vol 102, 1980, pp.598-604.

28. Acharya, S., and Patankar, S.V., "Laminar Mixed Convection in a Shrouded Fin Array", ASME J. of Heat Transfer, Vol 103, 1981, pp. 559-565.

29. Prakash, C., and Patankar, S.V., "Combined Free and Forced Convection on Vertical Tubes with Radial Internal Fins", ASME J. of Heat Transfer, Vol 103, 1981, pp.566-572.

30. Roache, Patrick. J., "Computational Fluid Dynamics", Hermosa Publishers, New Mexico, 1982.

31. Miyakoda, K., "Contribution to the Numerical Weather Prediction- Computation with Finite Differences", Japanese J. Geo-Physics, Vol 3, 1962, pp.75-190.

32. Patankar, S.V., and Spalding, D.B., "Heat and Mass Transfer in Boundary Layers", 2nd ed., Intertext Books, London, U.K., 1970.

33. Harlow, F.H., and Welch, J.E., " Numerical Calculations of Time Dependent Viscous Incompressible Flow of Fluid with Free Surface", Physics of Fluids, Vol 8, No 12, 1965, pp. 2182-2189.

34. Kays, W.M., and Crawford, M.E., "Convective Heat and Mass Transfer", 2nd ed., McGraw Hill, New York, 1980.